DEVELOPMENT AND CHARACTERIZATION OF NOVEL BIOINK BY USING DECELLULARIZED EXTRACELLULAR MATRIX FOR BONE TISSUE ENGINEERING APPLICATIONS

A Thesis Submitted to
the Graduate School of Engineering and Science of
Izmir Institute of Technology
in Partial Fulfillment of the Requirements for the Degree of

DOCTOR OF PHILOSOPHY

in Bioengineering

by
Aylin KARA ÖZENLER

May 2023
İZMİR

ACKNOWLEDGMENTS

ABSTRACT

DEVELOPMENT AND CHARACTERIZATION OF NOVEL BIOINK BY USING DECELLULARIZED EXTRACELLULAR MATRIX FOR BONE TISSUE ENGINEERING APPLICATIONS

Bone tissue engineering has focused on the development of functional scaffolds that can organize bone regeneration with appropriate structures and properties. Three-dimensional (3D) printing technology enables the development of personalized scaffolds. In addition, biological scaffolds obtained by decellularization have various advantages for developing natural-based scaffolds. The development of printable, patient-specific bioinks derived from decellularized extracellular matrix could provide 3D fabrication of tissues and organs with high potential to mimic native tissues.

The presented thesis study demonstrates the development of various bioink compositions for bone tissue engineering applications. In this regard, bone tissues were decellularized with a novel method and then characterized in order to verify the removal of whole cellular components for eliminating immunological reactions. After the pulverization of tissues, decellularized bone (DB) particles were used as an additive within various ink combinations (alginate-, gelatin- and alginate-gelatin-based). Thus, various bioink formulations were developed containing DB particles, biopolymers and mesenchymal stem cells (MSC). All prepared bioinks were bioprinted, then the viability, proliferation and differentiation capacity of the cells inside the structures as well as the physical, rheological, and printability properties of the inks were assessed.

The results revealed that all bioink combinations were suitable for bioprinting and the addition of DB particles improved cell proliferation and osteogenic differentiation in all bioink formulations. Alginate-based bioinks exhibited the greatest printability and shape fidelity, gelatin-based bioinks showed the highest cell proliferation and attachment, also, gelatin incorporation into alginate-based bioinks improved the biological activity of cells. In conclusion, cytocompatible, functional composite bioinks developed in this thesis study are of value for bone tissue engineering research in future to explore their functions in the living system and show complete bone regeneration while maintaining their stability for a long time.

ÖZET

KEMİK DOKU MÜHENDİSLİĞİ UYGULAMALARI İÇİN HÜCRESİZLEŞTİRİLMİŞ HÜCRE DIŞI MATRİS KULLANILARAK YENİ BİYOMÜREKKEP GELİŞTİRİLMESİ VE KARAKTERİZASYONU

Kemik dokusu mühendisliği, uygun özelliklerle kemik onarımını sağlayan işlevsel doku iskelelerinin geliştirilmesine odaklanmıştır. Üç boyutlu (3D) baskı teknolojisi, kişiselleştirilmiş malzemelerin tasarlanmasını sağlar. Bununla birlikte, hücresizleştirme tekniği ile elde edilen biyolojik doku iskeleleri, doğal malzemeler üretilmesi için pek çok avantaj sunmaktadır. Hücresizleştirilmiş dokulardan üretilen yazdırılabilir, hastaya özel biyomürekkeplerin geliştirilmesi, doğal dokuları taklit etmek için yüksek potansiyele sahip doku ve organların üretimini sağlayabilir.

Sunulan tez çalışması, kemik dokusu mühendisliği uygulamaları için çeşitli biyomürekkep geliştirilmesini temel almaktadır. Bu doğrultuda, kemik dokuları yeni bir yöntemle hücresizleştirilmiş ve immünolojik reaksiyonları ortadan kaldırmak için tüm hücresel bileşenlerin uzaklaştırıldığını doğrulamak için karakterize edilmiştir. Toz haline getirilen dokular, hücresizleştirilmiş kemik (DB) parçacıkları olarak çeşitli mürekkep kombinasyonlarının (aljinat ve jelatin temelli) hazırlanması için kullanıldı. Böylece, çeşitli biyomürekkep formülasyonları, DB parçacıkları, biyopolimerler ve mezenkimal kök hücreler (MSC) kullanılarak geliştirilmiştir. Hazırlanan tüm biyomürekkepler bir 3D biyoyazıcı kullanılarak baskılanmış ve yapıların içindeki hücrelerin canlılığı, çoğalmaları ve farklılaşma kapasiteleri ile mürekkeplerin fizyolojik, reolojik ve basılabilirlik özellikleri değerlendirilmiştir.

Sonuçlar, tüm biyomürekkeplerin 3D biyobaskılama için uygun olduğunu ve DB parçacıkları eklenmesinin hücre çoğalmasını ve osteojenik farklılaşmayı arttırdığını ortaya koymuştur. Aljinat temelli biyomürekkeplerin mükemmel basılabilirlik özellikler gösterdiği, jelatin temelli biyomürekkeplerin en yüksek hücre canlılığına sahip olduğu ve aljinat temelli biyomürekkeplere jelatin eklenmesinin hücre canlılığı ve çoğalmasını arttırdığı saptanmıştır. Özetle, tez çalışmasında geliştirilen kompozit biyomürekkepler, canlı sistemdeki işlevlerini keşfetmek ve tam kemik iyileşmesi göstermek için kemik dokusu mühendisliğinde gelecekteki araştırmalar için değer taşımaktadır.

Dedicated to my family…

TABLE OF CONTENTS

LIST OF FIGURES

CHAPTER 1

INTRODUCTION

1.1. State of the Art

Tissue engineering is an emerging multidisciplinary field that aims to regenerate tissues using biomaterials, cells and bio-signal molecules. In biomaterials science, research strives aims for the discovery of biocompatible and biomimetic materials in accordance with the composition and structure of tissues for therapeutic or diagnostic purposes[1]. Thus, it aims to induce, monitor or support tissue healing and repair or replace defective tissue. A growing number of tissue engineering research studies conducted over the past several years have proposed the combination of materials, cells and biosignal molecules while using new methods for tissue regeneration[2–4]. Bone tissue engineering is concerned with bone regeneration and healing and focuses on designing novel ways to encourage bone creation in clinical emergencies that cannot be healed with the help of conventional techniques. Thus, with the developing technology, advanced and innovative methods could be used to repair damaged tissues[5].

New methods and biologic materials similar to extracellular matrix (ECM) have been widely investigated for regeneration of numerous tissues. Decellularized extracellular matrix (dECM) scaffolds for the bioengineering of tissues or human-scale organs have been extensively investigated for therapeutic applications. Decellularization methods and recellularisation of the tissues with autologous cells have great potential for regeneration of the tissues[6].

In the last decade, kidney[7], lung[8], heart[9], and liver[10] tissues have been used to develop dECM scaffolds showing high potential applications in regenerative medicine. Furthermore, injectable decellularized tissue-based hydrogels were developed from heart[11], dermis[12], urinary bladder[13], liver[14], blood vessel[15] and adipose tissue[16], and showed promising results for developing biological tissue-derived scaffolds. Although there have only been a few studies on bone decellularization, injectable hydrogels made from decellularized bone (DB) have been developed after the demineralisation process,

which causes insufficient biomineralisation and cellular activity needed for regeneration[17,18]. Along with the increasing use of injectable hydrogels in three-dimensional (3D) bioprinting, the concept of organ printing has lately taken the lead in the production of biomimetic scaffolds.

3D bioprinting applications have improved significantly, with various advantages in producing tissue- or patient-specific functional biomaterials with different cell types by layer-by-layer process. Numerous studies have been reported using natural or synthetic polymer-based 3D-printed hydrogels for bone tissue engineering. Still, to the best of our knowledge, no study has been presented that DB-derived 3D-bioprinted hydrogels that contain both organic (collagen and non-collagenous proteins) and inorganic (mineralised crystals) components of bone tissue. The advantages of decellularized ECM and its usage in 3D bioprinting applications could overcome the problems faced by bone-tissue engineering. The development of printable patient-specific ECM bioink could enable 3D biofabrication of tissues and organs that functionally match the defective tissues. Therefore, the approach of using DB within biocompatible polymers as a bioink could facilitate bone regeneration with the desired structural similarity and biological functionality. In consideration of this approach, this thesis study presents different novel bioink formulations composed of biopolymers and DB, as well as the development of functional cell-laden constructs by 3D bioprinting for bone-tissue engineering applications.

1.2. Tissue Engineering

Tissue engineering is a multidisciplinary field that focuses on reconstructing organs and functions to produce physiologically similar 3D structures[19]. In the classic tissue engineering approach introduced by Langer and Vacanti, the appropriate cell types are seeded in biodegradable 3D structures fabricated to mimic the target organ or tissue and are supplied with the appropriate biological signals (growth factors and signalling molecules) according to the target tissue properties[20].

3D structures/scaffolds made from synthetic or natural materials are used for cell attachments, growth differentiation and support tissue formation with appropriate ECM production. The ECM in the native tissues is a 3D network composed of proteins and polysaccharides that supports cell–cell and cell–ECM interaction and the diffusion of

nutrients and metabolites[21]. A scaffold acts as a synthetic ECM, modifying biomaterials to mimic the native tissue ECM is a major challenge. The ideal characteristics of a scaffold should include an anatomically appropriate shape, biological compatibility with the surrounding tissues and biological fluids to reduce the immune response, preparation using a biodegradable polymer with an appropriate degradation rate, non-toxicity of the scaffold itself and its degradation products and mechanical support[22].

In the last 30 years, a range of biomaterials have been produced that imitate the ECM by using natural polymers, including collagen and fibrin to promote cell attachment and growth[23,24]; bioabsorbable polyesters, such as polylactic and polyglycolic acid, which provide stronger structures than natural biomaterials and tunable degradation behaviour[25]; ceramic materials, including calcium phosphate or bioglass, which mimic the biomineralisation property as mineral content of bone and stimulate cell regeneration[26]; and composite materials, which are obtained by a combination of two or more of the above-mentioned groups[27]. In order to include cells into these materials, numerous techniques have been presented for cell isolation and expansion, then to repopulate them within scaffolds and obtain cell-laden constructs that can be implanted into the defective tissue. Along with the improvement of technology for material production and cell-culture techniques, modulating extracellular signalling by bioactive scaffolds and intracellular reprogramming approaches have marked advances for regenerative medicine applications[28,29]. Thus, the production of scaffolds that could be able to respond to cell signals have made large advances and brought a new perspective to tissue engineering. Furthermore, there has been eminent progress in tissue engineering applications to induce or control direct tissue regeneration (for example, functional scaffold fabrication composed of bioactive agents without losing bioactivity)[30,31].

Numerous techniques have been developed to mimic the native ECM microstructure and guide cellular activity in tissue engineering fields (Figure 1.1). Porous structures similar to the ECM in many tissues can be obtained by a freeze-drying technique[32–35], a fibrillar network similar to the nervous system can be fabricated by electrospinning technique[36], and more complex structures can be produced layer-by-layer with a computer-assisted design using 3D printing[37,38]. Additionally, tissues can be treated with various decellularization techniques according to tissue type to remove cells and obtain a native tissue microenvironment. Decellularization methods have been

developed for several tissues, such as liver[10], kidney[39], heart[9], lung[40] and meniscus[41], proving their potential in tissue-engineering applications. Decellularized tissues provide native microenvironmental cues that regulate and support cell behaviour since native ECM contains tissue-specific macromolecules, cytokines and growth factors[42]. Thus, cell functions could be enhanced by preserved ECM components after decellularization, compared to the synthetic biomaterials. With those approaches, tissue engineering research is being improved and new alternatives are being developed to fabricate biomaterials that can better mimic organs and tissues. Besides the advanced research, alternative approaches strive to develop relevant biomimetic structures for tissue regeneration and immediate clinical applications.
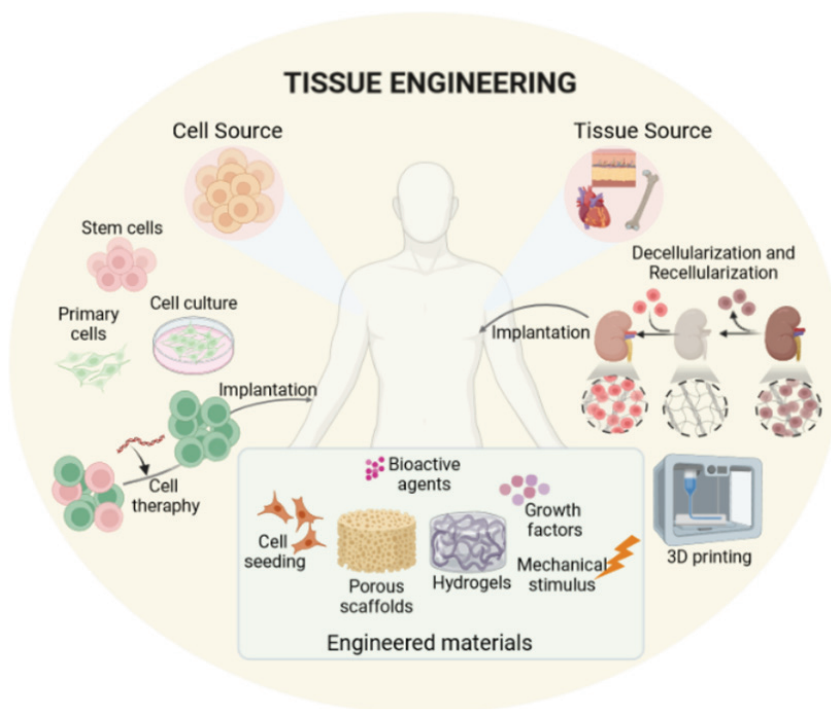
Figure 1.1. Tissue engineering (TE) paradigm consists of isolated cells from the patient and cell seeding into engineered scaffolds specifically fabricated for the target tissue. The engineered biomaterials, such as microporous scaffolds and hydrogels produced with various engineering techniques, serve as an environment for cell growth, proliferation and migration within the specific condition composed of growth factors, biological signals and bioactive agents. Tissue engineered-structures can be implanted in a patient and undergo a remodelling process that allows tissue or organ regeneration. (Created with BioRender.com.).

1.3. Bone Tissue Engineering

Bone tissue engineering research proceeds with the increasing acceleration for the treatment of bone tissue loss and provides effective solutions with innovative approaches. Bone, mainly composed of collagen and calcium phosphate crystals, is one of the few tissues that can heal itself with complete reconstruction and consists of a complex array of biological, structural and metabolic functions[5,43]. Bone tissue offers natural self-repairing, remodelling and regeneration, which is a major benefit. Although this unique ability allows for the regeneration of minor fractures, beyond critical size defects regeneration does not complete and healing does not occur, which is still a fundamental challenge to be addressed in clinical surgery[44,45]. With the continuous progress of biomaterial science and technology, new approaches and alternatives are being developed to fabricate biomaterials for regeneration and mimic bone tissue.

Bone is a vascularised tissue that enables structural support, withstands load-bearing and responds rapidly to metabolic demands[46]. It also has a well-organised structure from macro- to nano-scale structures (Figure 1.2). Bone tissues are composed of organic components (22 wt%, collagen and non-collagenous proteins), inorganic components (69 wt%, crystalline minerals) and water (9 wt%). The main organic components are collagen type I, type II, type III and type IV and fibrins[47]. The noncollagenous matrix proteins, such as proteoglycans and glycoproteins, number over 200, and there are also inorganic crystalline mineral components known as hydroxyapatite that contain calcium phosphate. Most of the mammal bone tissues has the highest calcium content and can be consider as an organic-inorganic nanocomposite structure[48]. Organic components provide elasticity, while inorganic components provide strength. Bone has a heterogeneous, anisotropic structure as a consequence of the association between its mechanical, biological and chemical properties and functions[47].
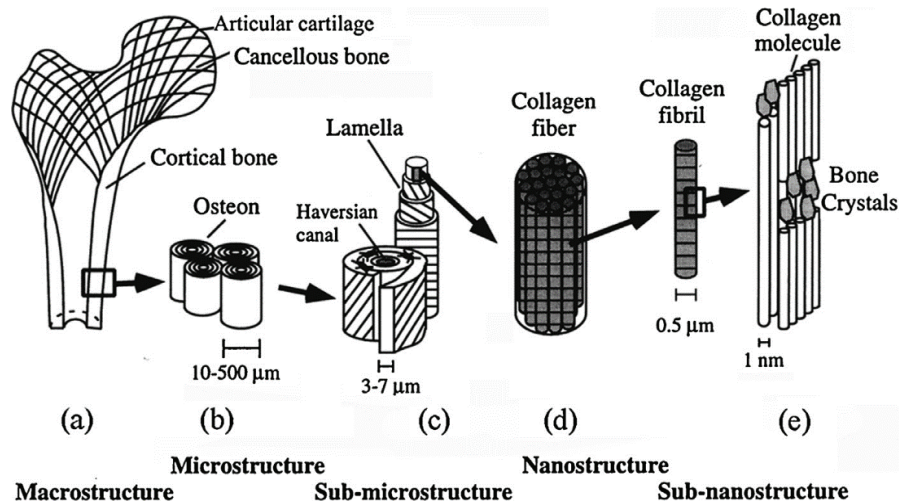
Figure 1.2. Hierarchical structure of bone tissue: (a) compact and trabecular bone; (b) osteons with Haversian systems; (c) lamellae; (d) collagen fiber assemblies of collagen fibrils; (e) bone mineral crystals, collagen molecules, and non-collagenous proteins[49].

Bone injuries are a key cause of aged patients' disabilities and consequent reduction in life quality. In bone defects, osteoporosis-related fractures, trauma, congenital bone abnormalities and tumor resections, there is an increment demand for orthopaedic surgery[50]. The human body can efficiently repair fractures in bone, and small bone defects can self-repair by the growth of natural bone, whereas large bone defects resulting from trauma or bone diseases require more complex therapies[50]. Approximately 2.2 million bone graft surgeries are carried out annually worldwide. The focus of current treatments is to replace the damaged bone tissue using donor graft tissues (xenografts, allografts and autografts) or metallic implants. These techniques have certain drawbacks, though, such as pain at the donor site, bone fractures, morbidity and a limited supply of bone grafts[51,52]. Tissue-engineering (TE) applications and regenerative-medicine approaches focus on regenerating defected tissues and organs by producing biological alternatives that restore, preserve or enhance tissue function rather than replacing defected tissues with metallic implants.

In bone-tissue engineering and regenerative medicine, biomaterials are an essential substitute for bone tissue that provide an environment for cell attachment, proliferation, differentiation and migration and serve as a guide when implanted into the defective bone[53]. Key attributes of engineered biomaterials for bone-defect repair

include biocompatibility, biodegradability, microstructure, osteoconductivity and mechanical properties. The primary requirement for biomaterials is cytocompatibility or biocompatibility, which is the capacity for cell adhesion, migration and proliferation without inducing a favourable immune response or a severe inflammatory response[53]. In addition, a significant property that offers enough mechanical support during the formation of new bone and prevents inducing an inflammatory reaction against the material's foreign components is the capability of appropriate biodegradability. Moreover, porous structures facilitate the diffusion of nutrients and metabolic waste products, which has been demonstrated to enhance the biological activity of osteoblasts. In bone-tissue engineering, scaffolds should have sufficient mechanical strength, which enables mechanical support during tissue regeneration[54]. Finally, an engineered biomaterial should have the appropriate material properties to enable 3D printing into patient-specific anatomical shapes that fit the defective area as well as being reproducible in large quantities.

1.4. Scaffolds for Bone Tissue Engineering

Numerous methods have been developed for fabricating 3D structures in bone tissue engineering, giving rise to scaffolds with unique properties and morphologies. There are mainly two scaffold fabrication methods depending on the choice of materials which determine the scaffold properties. Conventional or traditional methods enable easy production through high amount of products with the same features. Porous foam-like scaffolds are produced by solidification of the polymer in organic solvent and dissolution of the porogens, mainly salts, with specific size include into solution and dissolve the porogens. Following the dissolution of the porogens and evaporation of the solvent, 3D porous scaffolds are obtained. In spite of the simplicity of this method, porosity control, homogenous disperse of the porogens, porogen and polymer dissimilarity are the main disadvantages[55]. Besides, remaining residual solvents and porogens inside the polymer affect the biocompatibility of the scaffolds[56]. Melt molding and gas foaming methods are also used create pores into the molded polymer by heating of the polymer and gas development, respectively. Although allowing the solvent-free 3D scaffold fabrication, those methods have similar disadvantages with solvent casting method and not suitable for cell growing[57,58].

Besides the disadvantages of all the methods mentioned above, freeze-drying method has many advantages among the traditional fabrication methods. In freeze-drying method, 3D porous scaffolds produced by lyophilisation which is described the removal of ice crystals of the solvents led by sublimation and form porous structure under vacuum[59]. The porosity and pore sizes can be controlled the freezing temperature and molecular weight of the polymer. 3D lyophilized porous scaffolds obtained from both natural and synthetic polymers also addition of different bioactive particles showed promising potential in bone tissue engineering applications[34,35,60–62]

The limitations of traditional fabrication methods including various difficulties in tuning microstructure, pore size and porosity encountered in tissue engineering applications, has led to the development of advanced scaffold fabrication methods. Therefore, new advance methods such as electrospinning or rapid prototyping have revealed to control the structural properties of the scaffolds more precisely.

Electrospinning method is one of the delicate strategy where the 3D scaffolds is fabricated with the fiber formation in a range of micrometre to nanometre provide larger surface area[63]. Numerous natural (e.g. silk fibroin, chitosan, collagen, etc.) and synthetic (poly lactic acid, poly caprolactone, polyvinyl alcohol) polymers have been used in this techniques[64]. The electrospinning method provides a large surface area with great surface/volume values by the production of the nano-sized fibers, and it is possible to form a micro-/nanoporous structure with adjustable porosity. In addition, it enables a flexibility to adapt to a broad variety of sizes and shapes, and an ability to manage the nanofiber structure with the addition of bioactive agent, loading drugs for drug delivery systems[63]. Although electrospinning has many advantages, synthetic polymers are more suitable for electrospinning due to their controllable and tuneable properties, and the use of natural polymers with high biocompatibility and hydrophilicity is limited[65].

Moreover, different scaffolds include hydrogels, which have the ability to swell over four-fold than their weight and facilitate the diffusion of nutrients[66]; biological scaffolds, which provide natural substitutes by removing of cells to avoid immunological reactions and required mechanical properties[67]; 3D printed scaffolds, which provide to fabricate well-defined internal structure with desirable shapes[68]. In this thesis study, biological scaffolds obtained by decellularization methods and 3D printed scaffolds and biofabrication are focused on. Therefore, these two topics have been emphasized more in the following sections.

1.5. Biological Scaffolds

Numerous methods and materials have been widely investigated to obtain structures similar to ECM and provide for optimum regeneration of the tissues. The decellularization process is one of these methods that could be the most proper process to provide a better mimic of the ECM structure.

The primary purpose is to remove the cellular components from tissue while preserving ECM proteins and minimise cell-mediated immunological reactions; thus, it can be possible to obtain a cell-free biological structure. Different decellularization methods, such as gamma irradiation, lyophilisation/cryopreservation, high-pressure treatment, enzymatic treatment and chemical decellularization, have been used to prepare biological scaffold material. The decellularization process depends on the physical and biochemical structure of the tissue and the chemicals and methods selected for decellularization. Each step can affect the microstructure and biochemical properties of the tissue. The efficacy of the treatment is directly influenced by the antigenicity of the implanted decellularized tissues, which research has shown vary depending on the decellularization technique used. Thereby, the antigenicity of the tissues can be reduced with the appropriate decellularization methods. The fundamental prerequisites for ideal decellularization are the separation of cells and nuclear components, which are caused by cell-mediated immunogenic reactions as well as the preservation of ECM, which provide mechanical and structural stability, as well as the protection of cell adhesion sites for cell growth. The use of ECM scaffolds as a decellularized allograft or xenograft tissue has become the preferred application in tissue engineering[69,70].

The success of the decellularization process is highly correlated with the method used, the chemicals and their concentrations. Decellularization methods are classified as physical, chemical and biological. The method to be applied and the steps to be followed should be selected depending on the cellular density, thickness and molecules in the biochemical structure of the tissue.

Physical decellularization methods include freeze-thawing, direct pressure, high pressure and sound waves[13,71]. Gamma radiation is a broadly-used method to sterilise materials. It is quite effective at destroying cells and pathogenic microorganisms. Using a high amount of energy (3.5 Mrad), however, leads to a decrease in mechanical stability; therefore, it is improper for structural stability. On the other hand, high-

pressure treatments (600 MPa) can destroy the cells but retain the ECM and might still be immunogenic. Freeze-thawing is an effective method among these methods, as it leads to the destruction of the cells by the formation of ice crystals in the tissue and helps loosen the tissue to remove the cells. Freeze-thawing is also a simple and cheap method and is therefore preferable. Although physical methods were used alone in many studies, they are insufficient when used alone to remove the cellular components from tissue[72]. Physical applications can be performed to assist the decellularization process.

     Enzymatic decellularization methods or enzymes are commonly used in decellularization of the various tissues and are highly effective in removing cellular components. Trypsin is a proteolytic enzyme used to remove cellular components. Trypsin, however, causes ECM damage and could change both the mechanical and biological properties of the tissue[73]. Nuclei are used to help remove nuclear substances from tissues by breaking down DNA and RNA. To remove cells from tissues, the cell membranes must be lysed, and nuclear materials must be removed[74]. Enzymes are the best way to reach the nuclear components; therefore, the nuclease step can be performed within the protocol rather than using the enzymatic decellularization method alone. In addition, the time to treat tissue with enzymes is another important point to consider. Long incubation damages the ECM, while short incubation prevents the cellular content from being completely removed from the tissue[75].

     Chemical decellularization methods are important steps to remove cells from tissues while protecting the ECM structure. Acids and bases dissolve cellular components by providing hydrolytic degradation of biological molecules. The use of acids and bases, however, should be chosen carefully, as they can cause significant damage to the tissue. For example, acetic acid does not damage sulphated GAG, while collagen fibrils affects it[76]. Peracetic acid (PAA) is widely used for disinfection and sterilisation at the end of the process. It can be used as a decellularization agent due to its ability to remove nuclear residues without causing damage to ECM. Bases were used in the early stages of skin decellularization to remove hair, but the mechanical properties were negatively affected due to the removal of growth factors from tissue and damage to collagen fibrils[77]. Hypertonic and hypotonic solutions have an osmotic-shock effect on tissues, causing the cells to break down[78]. For maximum osmotic effect, hypotonic and hypertonic solutions can be passed through the tissue in cycles. These

solutions could help to remove damaged cells from tissues. Hypotonic and hypertonic solutions alone do not affect the separation of cells and, when used with detergents, they give more effective results[79].

Ionic and non-ionic detergents have been widely used in the decellularization process and are important steps for decellularization since detergents dissolve the cell membrane and denature its proteins.

Detergent exposure time is an important factor in preventing damage to ECM during the separation of cells from tissues. In addition, detergent concentration and the use of different combinations of detergents results in damage to the ECM. The most commonly used detergents in decellularization method are sodium dodecyl sulphate (SDS, ionic detergent), Triton-X (non-ionic detergent) and tri-nitro-butyl phosphate (TnBP). SDS denatures ECM proteins by breaking down the cell and nucleus membrane. Many studies have shown that it has very suitable for the decellularization method[77,80,81]. SDS effectively removes cells and nuclear contents, but it can also damage GAG, growth factors and collagen fibrils[80–82]. High SDS concentrations can not only eliminate cell content but also damage ECM proteins and collagen fibrils. Low concentrations should be preferred to minimise the harmful effects. Besides SDS, Triton X-100 is a non-ionic detergent commonly used to break down cells[77,79]. It can remove the cellular content of tissue without damaging protein–protein interactions in the tissue. This effect, however, can be suggested for the decellularization of thin tissues; it is insufficient for the decellularization of denser tissues, such as kidney and liver.

The most effective decellularization protocol includes a combination of different protocols consisting physical, chemical and enzymatic methods. In this combination, initially, physical methods damaged the cell membrane, then enzymatic method facilitated the removal of cellular components, followed by the dissolution of nuclear and cytoplasmic components with chemical treatments using ionic or non-ionic detergents, and finally removal of all cellular debris from tissue. The last step of decellularization is the removal of residual chemicals to prevent a negative host-tissue response. Physical, chemical and enzymatic decellularization mechanisms can be used for various tissues in various combinations. Thus, decellularized tissues or organ transplantation could be possible with minimum adverse immunological effect, and decellularized tissues can be repopulated with patient-specific cells for recellularisation (Figure 1.3).

11
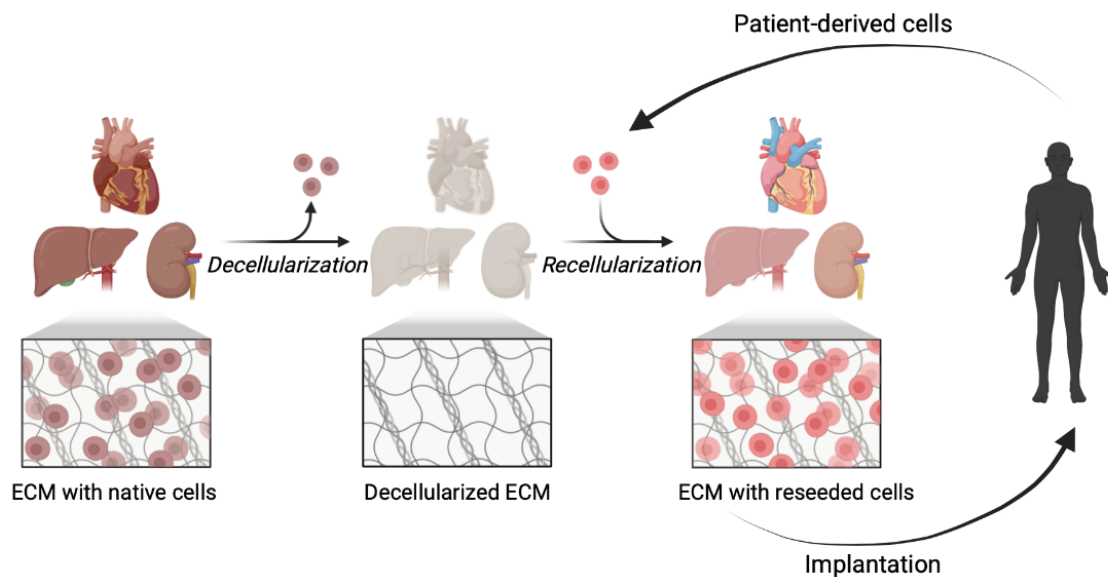
Figure 1.3. Concept of decellularization. Cell-free organs/tissues can be obtained by decellularization of native tissues, following the recellularization with patient-derived cells, recellularized structures can be implanted to the patients. (Created with BioRender.com.).

The successful decellularization of intestine[83], urinary bladder[84], liver [85], skin[86], and meniscus [41,87] were reported in the literature. An efficient decellularization method to remove vital immunologic cells could allow biological scaffolds to be obtained that can better mimic tissues for tissue engineering applications. Although decellularized scaffolds are already used in clinical applications (e.g., skin tissue), there remain key challenges to be addressed, especially hard tissue engineering. To increase the long-term outcome of biological ECM scaffolds, new alternative strategies are needed.

Recently, a few studies related to bone tissue decellularization were reported. On bone decellularization studies, it is observed that demineralisation and decellularization were used together. The inorganic components that provide mineralisation of the tissue are damaged while separating the cellular components. On the other hand, a high amount of detergent (0.5%, 1%, 2.5%) and a mixing of the different detergents were used for the decellularization of the bone tissue[18,76,88,89], which could caused damage to the ECM structure of the bone tissue. In addition, performing the demineralization process while the hydrolysis induced by HCl causes removal of the inorganic mineral content of bone, which is most important for biomineralisation during regeneration of the bone and destruction of the collagen structures[90]. This thesis focuses on the bone

12

tissue decellularization method preserving inorganic components as well as the organic components of the bone, which is the most important factor in biomineralisation.

Using decellularized tissues as tissue-specific ECM scaffolds has shown great promise for repairing and regenerating tissues and organs. If dECM can be incorporated into injectable materials, such as hydrogels, cells can be easily encapsulated within the dECM-incorporated hydrogel matrix. In addition, the injectable hydrogels are quite suitable for minimally invasive arthroscopic surgery widely performed in clinics[91,92]. Hydrogels can fill an irregularly-shaped tissue defect, transfer cells or drugs, and create a stable milieu for cell growth to support the formation of new tissue[12]. Injectable hydrogels incorporated into decellularized tissues and derived from heart[11], dermis [12], urinary bladder[13], liver[14], blood vessel[15] and adipose tissue[93], have been demonstrated. It is noteworthy that decellularized porcine heart-derived hydrogels were delivered into another infarcted porcine heart by a catheter, which demonstrated great promise in clinics[94]. There is, however, no reported study on the decellularized bone-incorporated 3D-bioprinted hydrogel, which is one of the main focuses of the thesis study. Decellularized bone ECM structures could provide a natural tissue-equivalent milieu that allows various benefits among other materials that still lack bio-functionality[11,75,95]. Decellularized bone tissues that preserve bone histoarchitecture and include the organic and inorganic components of bone can be used to create functional materials. With the advantages of decellularized ECM scaffolds, 3D-printed patient-specific scaffolds have great potential for tissue-engineering applications.

1.6. 3D Bioprinting

3D bioprinting is an innovative technique that enables the fabrication of engineered tissue-like constructs by depositing biomaterials and cells together within micrometres to millimetres of the desired shape (Figure 1.4). 3D bioprinting research has grown quickly over the past ten years as an emerging area of regenerative medicine. By simultaneously depositing living cells and biomaterials, 3D-bioprinting technology enables the production of a 3D artificial implant or complex tissue 'from the bottom up' in user-defined patterns[96]. The printable material used while printing cells as bioink[97] to prevent cell damage during bioprinting and biomaterial ink should be biocompatible and have decent rheological and mechanical strength[98,99].
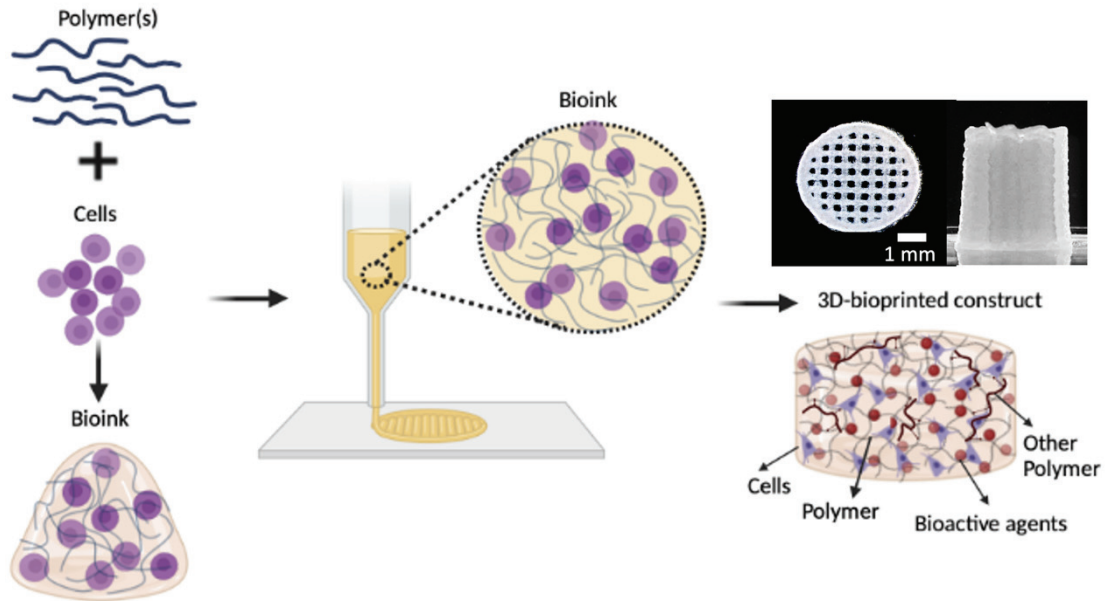
Figure 1.4. Schematic illustration of the bioink composition and 3D bioprinting.

3D printing is a critical fabrication technique for bone-tissue engineering due to its ability to control final bulk geometry and the internal structure of printed scaffolds. Hydrogels are mainly used as bioinks in 3D cell printing since they can allow cell encapsulation in a biocompatible and mechanically supportive microenvironment[100]. Numerous hydrogel-based scaffolds such as collagen, chitosan, gelatin methacryloyl (GelMA), alginate and hyaluronic acid (HA) have been reported previously that have controllable material characteristics and biocompatibility[101–104]. Among these polymers, collagen has advantages since it can be obtained from animals as a natural ECM protein, but it typically has poor mechanical properties and inferior shape fidelity after printing, which are major disadvantages in maintaining the 3D structure for both *in vitro* and *in vivo* conditions[105]. Despite the low mechanical properties of collagen hydrogels, they can be used with various natural or synthetic polymers to produce composite hydrogels[106]. Nevertheless, the production of the complex trabecular bone structure remains a major challenge[106]. A challenge faced in 3D printing is the development of novel bioinks with decent mechanical properties as well as biocompatibility for bone-tissue engineering.

3D printing technique offers promising results and allows for the production of tissue-specific structures with a controllable complex microstructure[107]. It can be easily adapted by printing various polymers and living cells at the same time and growing

them in a cell culture environment for the regeneration of the tissue[108]. 3D-printing technology enables the simultaneous printability of hydrogels prepared as bioink with the target tissue cells and the production of scaffolds that have a stronger regeneration feature and that are biologically and physically compatible with the defective tissue[38]. An ideal bioink should have chemical and mechanical properties similar to those of natural ECM, contain angiogenesis-promoting biochemical factors and exhibit appropriate rheological properties to be highly printable (e.g., with low shear stress and high resolution). Looking forward, 3D-printing technology provides advantages and disadvantages, but there are still many technical challenges to overcome and find an optimal 3D printing process as well as a proper material for bone engineering[106]. In addition to a decent design of novel bioinks for bone-tissue engineering that mimic the biochemistry of bone ECM (e.g., collagens, proteoglycans, enzymes), it is also required that the bioink should exhibit favourable rheological properties for 3D bioprinting: for instance, sufficient mechanical strength to maintain shape fidelity, shear-thinning behaviour and compatibility with the non-damaging crosslinking process[109]. In addition, hydrogels containing dECM have advantages regarding their high tunability: (i) injectability with a compatible form; (ii) tunable mechanical properties by adjusting concentration or strengthened by cross-linking; (iii) good processability that allows for the production of customised structures by 3D printing [110,111].

The biomimetic strategy involves mimicking tissues using ECM components, such as natural biopolymers (e.g., collagen, proteoglycan), proteins or biological signalling molecules derived from tissues to solve problems with tissue and organ regeneration. The better an artificial material matches its native biological model, the faster and more easily it might be integrated into the host tissue after implantation and involved in the remodelling cycle and finally result in a complete biological degradation and remodelling of the defective area[67,112]. Decellularization of the tissue without any significant changes in the structural features plays a critical role in tissue engineering, especially the regeneration of bone tissues due to the distinctive structure of the bone. Natural ECM scaffolds obtained by the decellularization method are widely studied because they have no immunological side effects, their mechanical strength is similar to natural tissue and the microstructure of the tissues is intact. The main purpose of the decellularization method is to remove the cellular components from the tissue without damaging the extracellular matrix (ECM), not to change the biomechanical tension and

to reduce the antigenicity of the tissues[67,75]. The decellularized ECM scaffolds are biomimetic candidates for a more ideal carrier than the synthetic scaffolds that exist in the literature in terms of containing collagen, glycosaminoglycan (GAG), matrix proteins and growth factors[113].

Recently, the development of printable tissue-specific ECM bioinks has enabled the 3D fabrication of tissues or organs that are more functionally matched with the defective tissue. Bioinks containing native ECM components presence in bone are attractive for development of functional bone-like structures using a 3D-printing technique. Pati et al. demonstrated dECM hydrogels obtained from the heart, cartilage and adipose tissues; cell-laden 3D-bioprinted dECM constructs improved the tissue formation more than a construct produced using only collagen[95]. In a different study, the feasibility of using 3D-printed scaffolds obtained from dECM bioink obtained from adipose tissue was evaluated for soft tissue regeneration[114], however, dECM bioinks showed inadequate mechanical stability since solubilisation of the ECM resulted in the loss of its natural structure and mechanical strength. Only a few recent studies exist for bone-tissue engineering applications. In those studies, decellularized bone tissue was used as hydrogel itself or printed with a 3D printer after demineralisation. Sawkins et al. reported on the use of decellularized and demineralised bone matrix hydrogel for bone-tissue engineering. They prepared hydrogels from decellularized and demineralised bovine bone and compared them to collagen hydrogels. After demineralisation, however, removing the inorganic content which is important for osteoinductivity caused insufficient cellular functions[18]. In another study, 3D-printed polycaprolactone were mixed with decellularized bone hydrogel to produce 3D scaffolds for bone-tissue engineering. It was reported that decellularized bone matrix-derived hydrogels enhance the osteoinductivity of polycaprolactone and have more healing capacity for bone regeneration *in vivo* [17]. Osteogenic activity and osteoinductivity are important for bone regeneration that provides effective treatment. Here, we presented a novel decellularized bone ECM-derived bioink composed of native bone ECM molecules and inorganic components for bone-tissue engineering applications. To the best of our knowledge, there is no bioink study available in the literature that can mimic bone tissue with both organic and inorganic structures in 3D printing applications.

CHAPTER 2

EXPERIMENTAL

2.1. Decellularization Process

Rabbit, rat and bovine femur tissues were used for the decellularization process. 1cm^3 pieces of bone samples were decellularized by a new decellulaization method consists of physical (freeze/thawing), chemical (detergent treatment) and enzymatic (nuclease solution) methods. Bone tissues were decellularized using our new technique involving physical, chemical and enzymatic treatments. As a physical treatment repetitive freeze-thawing cycles were applied. In chemical treatment, different sodium dodecyl sulfate (SDS) concentrations (0.05%, 0.1%$_2$ and 1% (w/v)) in hypotonic buffer solutions were used for the optimization of the decellularization process. Next, enzymatic solution consist of DNase and RNase were used to remove the residual nuclear component of the cells. Decellularized bone samples were sterilized using peracetic acid (PAA) then were washed with phosphate buffered saline (PBS).

2.2. Verification of the Decellularization Process

Decellularization of bone tissues were assessed by histologically, biochemically and mechanically. In histological assessments, Hematoxylin eosin (HE), Masson trichrome (MT) and Alizarin red (AR) staining were used. The cell nucleus were observed by fluorescence microscopy and surface morphology of the bone tissues were analysed by scanning electron microscopy (SEM). Besides, total DNA, collagen and glycosaminoglycans (GAG) amount of bone tissues were determined by biochemical analyses. Compression tests were performed to determine the changes in the mechanical properties of the tissues after decellularization.

Histological assessments: Bone tissues were investigated histologically for the verification of the decellularization process. After the decellularization, tissues were fixed in 4% paraformaldehyde (PFA, v/v) solution for 72h and then samples were

dehydrated using 100% ethanol, 100% acetone and 100% xylene. Following paraffin embedding process, samples were prepared as 5 μm thick sections using a microtome (Leica Biosystems RM2245). Prepared sections were stained using HE to evaluate general tissue histoarchitecture. Besides, MT and AR stainings were performed to observe collagen distribution and mineralization sites, respectively.

Fluorescence analysis: Decellularized bones were examined with fluorescence microscopy for verifying the cellular removal. Samples were fixed using 4% PFA (v/v) solution for 30 min. at room temperature. Following the washing samples with PBS, samples permeabilized by 0.1% Triton X-100. For observation of the cell nuclei, DAPI staining was performed and the samples were observed by fluorescence microscopy (Zeiss Observer Z1).

SEM Analysis: To observe the surface morphology of the bone tissues, samples were fixed using 4% PFA solution for 30 min. after the decellularization process then washed with grading ethanol series (25%, 50%, 75%, 90% 100%). After drying the samples in a vacuum oven at room temperature, coated with a gold layer then SEM analysis was performed with a Scanning Electron Microscope (Quanta FEG, Thermo Fisher Scientific).

Biochemical analysis: The total DNA content of bone samples was determined using DNeasy Blood and Tissue Kit. After decellularization, tissues were homogenized using Proteinase K and DNA was extracted from tissues using a Nucleospin Tissue kit following the manufacturer's protocol. The total DNA content of tissues was measured at 260/280 nm in a Nanodrop spectrophotometer (Nano 2000, Thermo Scientific).

Hydroxyproline assay was used to quantify the total collagen content of the bone tissues. The samples were hydrolysed with 6 M hydrochloric acid for 20 h at 95 °C. The test standards and sample solutions were prepared according to the kit manual (Quickzym Biosciences) and were incubated at 60 °C for 60 min prior to the absorbance measurements at 570 nm (Varioskan Flash, Thermo Fisher Scientific). The concentration of hydroxyproline was determined by the interpolation from the standard curve.

GAG content of bone tissues was quantified based on 1,9-DMMB assay. Firstly, enzymatic digestion were performed, samples were incubated in papain solution for 48h at 60 °C, tests standard or sample solutions were prepared following the manufacturer's protocol. The absorbance at 530 nm was recorded using a microplate

reader (Varioskan Flash, ThermoFisher Scientific). The concentrations of sulfated sugars representative of GAG were determined by interpolation from the standard curve.

Mechanical analysis: Mechanical properties of decellularized bone tissues were determined with compression tests using a universal testing machine (Shimadzu AG-X, Japan). Compression tests were performed using six replicates (n=6) with 1 mm/min crosshead speed up to failure. Compressive modulus was determined as a slope in the linear elastic deformation region from compressive stress-strain data and maximum stress was calculated based on the stress and stress data.

2.3. Preparation of Decellularized Bone Incorporated Bioinks

In this thesis study, different biopolymers were utilized in the development of several bioink formulations. The used biopolymers are gelatin (GEL, (from porcine skin, Type A, Sigma), sodium alginate (ALG, sodium alginate Sigma), and methylcellulose (MC, Sigma Aldrich, MW088 kDa). Gelatin (GEL) solution was prepared by dissolving GEL in ultrapure water at 80°C for 3h. ALG-based biomaterial ink was prepared by dissolving ALG in PBS and MC was used as a viscosity enhancing materials in powder form. For the sterilization, GEL solution was filtered using a 0.02 um filter after dissolving, ALG and MC were autoclaved before use. All further experiments were performed in sterile conditions.

Decellularized bone (DB) particles were prepared by using a laboratory mixer and filtered with a 100 μm mesh diameter after decellularization. For the sterilization of DB particles, gamma radiation was used. Prepared hydrogel precursors were mixed with different concentrations of DB particles and dispersed homogeneously using a magnetic stirrer. Then DB particles incorporated biomaterial inks were obtained.

For bioink composition, human pre-osteoblasts (MC3T3-E1) and human telomerase reverse transcriptase (hTERT) expressing mesenchymal stem cells (MSCs) were used. MC3T3-E1 cells were subcultured in alpha-modified minimum essential medium (α-MEM, MC3T3-E1 cells) and hTERT-MSCs were subcultured in Dulbecco's Modified Eagle Medium (DMEM). Culture mediums contained 1% (v/v) L-glutamine, 10% (v/v) Fetal Bovine Serum (FBS) and 1% (v/v) penicillin-streptomycin. After reaching sufficient cell number, cells were detached from the culture flask using

Trypsin/EDTA. Cell pellets (5×10^6 cells/ml) were obtained by centrifugation at 1250 rpm and gently mixed with inks.

2.4. 3D Bioprinting

Prepared bioinks were bioprinted using a 3D extrusion printer (Gesim Bioscaffolder 3.1, GmbH, Germany). All prepared hydrogel precursors were transferred into the cartridge, then extruded through the 410 μm nozzles at room temperature. All samples were fabricated as a cylinder shape including seven strands. 3D bioprinted GEL-based constructs were crosslinked using microbial transglutaminase (mTG) from *Streptoverticillium mobaraense* (Ajinomoto Co., Inc., ACTIVA WM, 85–135 U/g). ALG-based constructs were crosslinked using 100 mM $CaCl_2$ after 3D printing.

2.5. Printability Assessments of 3D-Printed Scaffolds

The accuracy of printing determined using images of 3D-printed structures, after the printing images were recorded by a light microscopy (Stemi 508, Carl Zeiss, Germany) and processed using Image J software. Printability factor were calculated using following equation according to the circularity (C), pore perimeter (P) and pore area (A) was calculated using the following equation[115]:

$$Pr = \frac{\pi}{4} x \frac{1}{C} = \frac{P^2}{16A}$$

Eq.1

The uniformity of the 3D-printed strands was quantified using the uniformity factor (U) [59], according to the horizontal length of a 3D-printed strut (L) and the theoretical horizontal length of a parallel strand (Lt) as shown in equation[116];

$$U = \frac{L}{L_t}$$

Eq.2

2.6. Rheological Characterization

The rheological properties of the DB incorporated biomaterial inks were determined by a rotational rheometer equipped with a plate-plate geometry in a diameter of 25 mm (Anton Paar, MCR 702e, Austria). By conducting amplitude sweep tests in the deformation range of 0.0001–10 at a frequency of 10 rad/s, the linear viscoelastic range and the yield point were identified. To describe the structural recovery, a thixotropy tests were performed. The thixotropy test is divided into a 30 s transient phase, a 30 s loading phase, and a 120 s recovery phase. The hydrogel precursors were applied to deformation of 0.001 at 10 rad/s during the transient phase and recovery phases. To destroy the structure, deformation was increased to 6 at a frequency of 10 rad/s for the loading phase. The entire thixotropy tests were performed at 25 °C. All rheology tests were carried out with a Peltier plate at 0.5 mm gap size to prevent sample drying, and to allow homogeneous heat distribution.

2.7. Fourier Transform Infrared Spectroscopy (FTIR)

The chemical composition of the 3D-printed scaffolds was determined by Attenuated Total Reflectance FTIR (ATR-FTIR) analysis. 3D-printed hydrogels were freeze-dried for 48 hours and measurements were performed at a wavenumber range of 4000 to 400 cm^{-1} (IR Affinity-1S, Shimadzu, Japan).

2.8. Scanning Electron Microscopy (SEM) Analysis

SEM analysis was carried out to evaluate the surface morphology, pore structure and particle-polymer interaction of the 3D-printed scaffolds. Following the printing, samples were freeze-dried then coated with a thin gold layer before the analysis. The images were recorded with a scanning electron microscope (Quanta FEG, Thermo Fisher Scientific).

2.9. X-ray Microtomography (µCT)

3D-printed scaffolds were investigated with µCT analysis to reveal the DB distribution within the structures. Scaffolds tomograms were recorded on a Skyscan 1076 scanner (Bruker, Kontich, Belgium), subjected 37 kVsource voltage and 228 mA source current. A titanium filter (0.025 mm) was used to reduce beam hardening artifacts. The scan resolution was set to 9 µm per voxel. An average of four frames was recorded every 0.3 degrees for noise reduction. The scans were reconstructed by subjecting the cone-beam algorithm in the NRecon software (Bruker, Kontich, Belgium). The datasets were segmented globally lower and upper gray threshold was set to 155 255 respectively to account for the denser DB particles.3D analysis of the segmented datasets was carried out to quantify the amount of DB particles and determine the DB particle size distribution. For 3D analysis and segmentation, CT analyzer software (Bruker, Kontich, Belgium) was used for 3D analysis and segmentation. 3D renderings in high resolution were generated using CTVox software (Bruker, Kontich, Belgium).

2.10. Swelling/Degradation behaviour

The swelling/degradation behaviour of the 3D-printed scaffolds was investigated according to the weight changes. The scaffolds were incubated in the cell culture medium (described in the cell culture section) at 37 °C with 5% CO_2 in a humidified atmosphere. The scaffolds (n=6) were immersed into the culture medium and the medium was refreshed two times in a week. The scaffolds were weighed at each time point, filter papers were used to remove the excess medium. The samples' initial mass before submerging in the medium (m^i) and the current weight at each time point (m_c) were noted. The following equation was used to determine swelling and degradation in weight %:

$$swelling\ (wt\%)\ and\ degradation\ (wt\%) = \left(\frac{m_c - m_i}{m_i}\right) x\ 100$$

Eq.3

2.11. Mechanical Characterization

Compression tests were carried out to determine the mechanical properties of 3D-printed scaffolds using a universal testing system equipped with a 100 N load cell (Instron 3300 Floor Model, Instron® GmbH, Germany). Six replicates of samples were used and tests were carried out using a 100 N load cells with a crosshead speed of 1 mm/min up to 15% strain. Using the compressive stress-strain data between 5% and 10% deformation, the slope in the linear elastic deformation region was calculated thus the Young's modulus was determined.

2.12. *In vitro* Cell Culture Assessments

3D-bioprinted cell-laden hydrogels were cultured in the α-MEM (for MC3T3-E1 cells) and DMEM (hTERT-MSCs) supplemented with 1% (v/v) L-glutamine, 10% (v/v) FBS and 1% (v/v) penicillin-streptomycin for 28 days. Cytocompatibility, cell viability and osteogenicity of cells within the 3D bioprinted structures were evaluated to assess the influence of the DB particles on the cell behaviour and functionality of the bioinks including potential application in bone tissue engineering. Therefore, cell-laden scaffolds were evaluated with cell culture assays, fluorescence microscopy, confocal microscopy and scanning electron microscopy (SEM) as well as material characterizations.

2.12.1. Live/Dead Staining

Live/Dead staining assay was used to determine the live and dead cells in the 3D-printed scaffolds. Cell-laden scaffolds were washed with Hank's Balanced Salt Solutions (HBSS) and incubated in culture media (described above) containing 2 µl/ml Calcein AM and 3 µl/ml ethidium homodimer-1 (EthD-1) (Invitrogen, Molecular probes by Life Technologies, USA) for 45 min at 37°C, 5% CO_2 in an incubator. After incubation, samples were washed with HBSS and examined by fluorescence microscopy (AxioScope A.1, Carl Zeiss, Germany).

2.12.2. Cell Viability

Water-soluble tetrazolium salt (WST) assay was carried out to determine the cell viability by conversion of WST through cellular metabolism into insoluble formazan. Cell-laden structures (n=4) were cultured for 28 days. The medium was removed at each time point, and samples were incubated in WST-8 solution (Cell Counting Kit-8, Sigma Aldrich, Germany) for 4 hours. After incubation, 100 µl aliquots were transferred into 96-well-plates, and the absorbance at 450 nm was recorded using a microplate reader (PHOmo, Anthos Mikrosysteme GmbH, Friesoythe, Germany).

2.12.3. Lactate Dehydrogenase Release Assay (LDH)

The potential cytotoxicity of the bioinks was evaluated using the LDH kit (Tox7 Toxicity kit, Sigma Aldrich). At each time point, cell culture medium was collected and mixed with LDH substrate solution, cofactor solution and dye solution into the cuvettes. After the 30 min. incubation of the samples protected from light, the absorbance at 490/ 690 nm was measured using a UV spectrophotometer.

2.12.4. Cell Proliferation

Cell proliferation was determined based on quantifying the double-strand DNA (dsDNA) by Quant-iT PicoGreen ds-DNA Assay-Kit (Invitrogen, Life Technologies, Thermo Fisher Scientific, USA). Cell-laden constructs (n=6) were cultured during 28 days and at each time point, samples were washed and lysed with the lysis buffer for 30 min at 37 °C then centrifuged at 5000 rpm for 5 min. The supernatant was collected and mixed with a Quant-iT PicoGreen assay buffer solution and incubated for 5 min at room temperature in the dark. Measurements were performed at standard fluorescein wavelengths (excitation 480 nm, emission 520 nm) using a fluorescence microplate reader (Infinite®M200, Tecan, Switzerland).

2.12.5. Cell Attachment and Morphology

In order to observe the cell adhesion and cell morphology on the 3D-printed scaffolds and inside the 3D-bioprinted cell-laden structures were examined by SEM, confocal and multiphoton microscope. Cell-seeded 3D-printed scaffolds were fixed with 4% PFA for 30 min. Then dehydrated in 25%, 50%, 75%, 90%, and 100% ethanol. A critical point dryer (Leica EM CPD300) was used for the complete drying of the samples. After coating the samples with a gold layer, samples were analyzed using a SEM (Auriga CrossBeam, Carl Zeiss microscopy GmbH, Germany).

After 3D bioprinting, samples (n=3) were fixed using 4% paraformaldehyde for 30 min. and washed with HBSS for three times. 1 µl/ml DAPI (Thermo Fisher Scientific USA) and 5 µl/ml Actin (phalloidine, Thermo Fisher Scientific USA) were used for staining nuclei and cytoskeleton, respectively. For confocal microscopy imaging, samples were observed with confocal laser scanning microscope (cLSM; Leica, TCS SP5 Germany),
z-stack images were acquired then process using Image J Software.

For multiphoton microscopy imaging, multiphoton microscope (TriMScope II, LaVision BioTec, Bielefeld, Germany), equipped with a HC FLUOTAR L 25x/0.95 W VISIR objective was used. DAPI and Actin were acquired at 450/70 nm (ET 470/70 m) and 620/60 nm (ET 620/60 m), respectively, at 810 nm excitation. All data were processed using Image J Software with 3D script plugin.

2.13. Statistical Analysis

The experimental data are presented as mean ± standard deviation (mean ± SD). The variations between groups in the biochemical assays and the biomechanical tests were assessed using one-way Analysis of Variance (ANOVA) with Tukey's multiple comparison test. P-values of 0.05 or less were considered significant ($p < 0.05$). Non-significant differences (ns) were indicated for $p \geq 0.05$.

CHAPTER 3

DECELLULARIZATION OF BONE TISSUE

The decellularization technique aims to remove the cellular components from the tissues or organs while preserving the ultrastructure composition of the tissues. Decellularized biomaterials as tissue-specific biological scaffolds show great promise for the regeneration of specific tissues and organs[42]. With the promising successful outcomes of decellularized tissues, these structures might find a place in clinical applications.

Numerous techniques have been used for the decellularization of the organs and tissues, such as physical (repetitive freeze-thaw, high pressure), chemical (ionic, non-ionic solutions, hypotonic, hypertonic buffers) and enzymatic (trypsin, collagenase, protease) methods[69,113,117]. Decellularization of the bone has recently gained attention as a biological scaffold due to its histoarchitecture and biochemical composition, including both organic and inorganic compounds. Several studies have been reported regarding the decellularization of bone tissue with different techniques. Sawkins et al. reported the enzymatic decellularization of bone using 0.5% trypsin following the demineralisation step[18]. Lee et al. used 0.5% SDS and 0.1% ammonium hydroxide for decellularization of rat calvaria[76]. In another study, bone tissues were decellularized using the enzymatic decellularization method with 0.05% trypsin and demineralisation with 0.5% HCl[88] Rindone et al. performed decellularization using several treatment steps with 0.5% SDS, 0.1% EDTA and 10mM Tris to remove cellular components from bone tissue[17]. Studies such as high detergent concentrations (0.5%, 1%) and demineralisation step after decellularization, however, both damage the natural ECM structure and decrease the biomineralisation characteristic specific to bone tissue[89]. Therefore, a more effective and suitable decellularization method for bone tissue is still needed.

In this chapter, a new decellularization method is presented that allows for the removal of the cellular components from bone tissue using a minimum detergent concentration without any damage to the ECM or any biomechanical changes in the structure. The primary goal is to protect the organic (collagen and non-collagenous proteins) and inorganic (mineralised crystals) components within bone; this is a

different approach from the currently reported decellularization or demineralisation techniques in bone-tissue engineering applications[41,75,87]. Figure 3.1 illustrates the schematic representation of the presented study. Bone tissues obtained from bovine, rabbit and rat femurs were decellularized with a combination of physical, chemical and enzymatic treatments, and 0.1% SDS was used as an optimum concentration for cell removal from the tissue without any additional detergent. The decellularization process was characterized by histological, biochemical and biomechanical analyses. Our results indicate that cellular components were removed from bone tissues and that ECM proteins for instance, collagen and GAG were preserved during the decellularization process. In addition, it was observed the mineralisation sites of the tissues were maintained after decellularization. This chapter demonstrates that our decellularization method was effective at developing biological bone ECM containing both organic and inorganic compounds by using a minimum concentration of SDS. It is foreseen that the obtained decellularized bone could be used as a biological substitute and would provide a favourable microenvironment for bone regeneration.
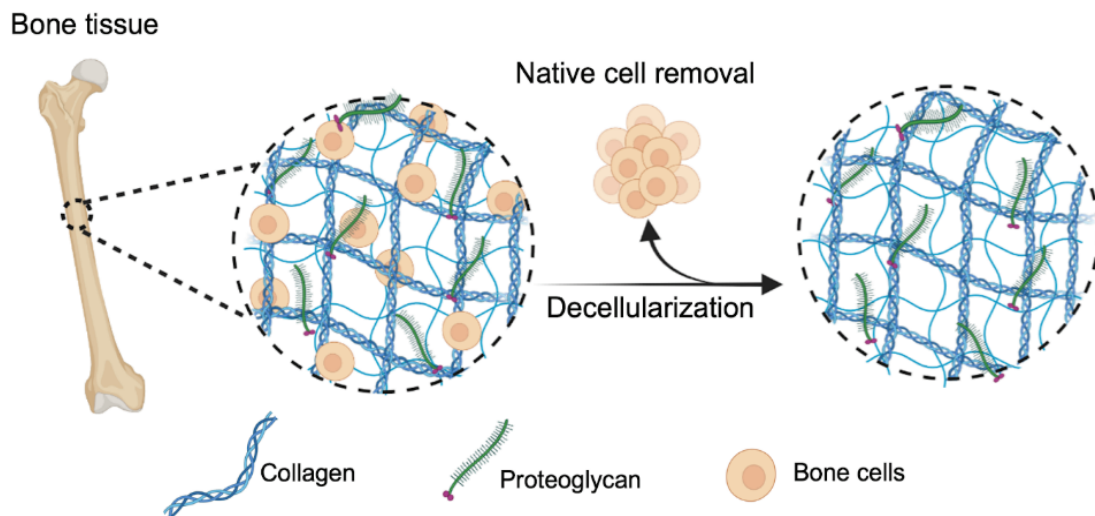
Figure 3.1. Schematic representation of decellularization of the bone ECM. (Created with BioRender.com.).

3.1. Materials and Methods

Bovine, rabbit and rat femur bones were used for decellularization. Bovine bones were obtained from a slaughterhouse in Izmir, Turkey. New Zealand White Rabbit bones (weight, 2.5–3.0 kg, female, n=5), and rat bones (weight, 150–200 g, female, n=5) were obtained from the Department of Laboratory Animal Science, Dokuz Eylul University, İzmir, Turkey. All experiments were carried out based on the protocol approved by Dokuz Eylul University Experimental Animals Ethical Council (Protocol No: 50/2017). The fresh bone samples were transferred to the laboratory and cut into 1 cm^3 pieces using an autopsy saw. All samples were then washed with PBS, including penicillin, streptomycin and gentamicin. Bone samples were stored at -20 ^{o}C until further use. Bovine bone tissues were decellularized using different SDS concentrations (0.05%, 0.1%$_2$ and 1% (w/v)). Subsequently, rabbit and rat bone samples were decellularized using an optimum SDS concentration. Decellularization was performed with our new technique involving physical, chemical and enzymatic treatments. Physical treatment was applied first, samples were frozen and thawed for five cycles: freezing at -80 ^{o}C for 3 h and thawing at room temperature for 4 h. For the chemical treatment, samples were immersed in a hypotonic buffer consisting of 10 mM Tris-HCl and incubated at 37 ^{o}C for 24 h. Then, solution was changed with0.1% SDS solution containing 0.1% (w/v) ethylene diamine tetraacetic acid (EDTA, Sigma Aldrich) and samples were incubated at 45 ^{o}C for 48 h agitation at 200 rpm. The chemical treatment step was repeated as three cycles. Next, enzymatic treatment was applied by incubating in a nuclease solution including 50 U/ml DNase I and 1 U/ml RNase (Applichem GmbH) in 50 mM tris-HCl (Sigma Aldrich) for 3 h at 37 ^{o}C; this treatment was repeated twice. As a final step, hypertonic buffer (1 M NaCl in 0.05 M tris-HCl) was used, then samples were washed with PBS (Sigma Aldrich) for 24 h at room temperature to exceed the residual chemicals. For the sterilisation step, samples were incubated with 0.1% (v/v) peracetic acid (Sigma Aldrich) in PBS for 3 h. Finally, decellularized bone tissues were washed in PBS at 37 ^{o}C and 25 ^{o}C for 24 h, repectively.

The decellularization process was verified by histological, biochemical and biomechanical methods. Fresh bone samples served as a control group for all evaluations. General morphology, collagen structures, GAG and mineralisation sites in the bone tissues were assessed with the staining of Hematoxylin-eosin (Biooptica),

Masson trichrome (GBL) and Alizarin Red S (Abcam), respectively. The surface morphology and nucleus of the bone tissues were observed after decellularization by SEM (Quanta FEG, Thermo Fisher Scientific) and confocal microscopy (Zeiss, LSM880). Bone tissues were stained and then observed with a light microscope (Olympus-CX31). A Nucleospin Tissue Kit (Macherey-Nagel, GmbH & Co. KG), Total Collagen Quantification kit (Quickzym, Biosciences) and Sulfate Glycosaminoglycan Quantification Kit (Amsbio Europe BV) were used for the determination of total DNA, collagen and GAG content, respectively. Moreover, the mechanical properties of decellularized bone were determined with a compression test using a universal testing system equipped with a 100 N load cell (Shimadzu AG-X, Japan). Compression tests were carried out with 1 mm/min crosshead speed up to failure. Compressive modulus was determined as a slope in the linear elastic deformation region from compressive stress–strain data, and maximum stress was calculated based on the stress and stress data.

The decellularization process was verified by histological, biochemical and biomechanical methods. Fresh bone samples served as a control group for all evaluations. General morphology, collagen structures, GAG and mineralisation sites in the bone tissues were assessed with the staining of Hematoxylin-eosin (Biooptica), Masson trichrome (GBL) and Alizarin Red S (Abcam), respectively. The surface morphology and nucleus of the bone tissues were observed after decellularization by SEM (Quanta FEG, Thermo Fisher Scientific) and confocal microscopy (Zeiss, LSM880). Bone tissues were stained and then observed with a light microscope (Olympus-CX31). A Nucleospin Tissue Kit (Macherey-Nagel, GmbH & Co. KG), Total Collagen Quantification kit (Quickzym, Biosciences) and Sulfate Glycosaminoglycan Quantification Kit (Amsbio, LLC) were used for the determination of total DNA, collagen and GAG content, respectively. Moreover, the mechanical properties of decellularized bone were determined with a compression test using a universal testing system equipped with a 100 N load cell (Shimadzu AG-X, Japan). Compression tests were carried out with 1 mm/min crosshead speed up to failure. Compressive modulus was determined as a slope in the linear elastic deformation region from compressive stress–strain data.

3.2. Results and Discussions

3.2.1. Decellularization of Bovine Bone Tissue

Bone tissue has a unique structure that contains osteon structures, Haversian and Volkmann's canals and distinctive cell types. Osteon is the distinctive structural unit of the cortical bone. Each osteon contains several concentric layers called lamellae, which are composed of osteoblasts and osteocytes, and the lamellae surround a Haversian canal, which contains small blood vessels[118]. Because of the circular concentric layer arrangement and compact structure of the bone, removing the cellular components from the bone is more difficult than from other tissues. The combination of different treatments could promote decellularization and obtain natural cell-free ECM. To investigate the effect of the decellularization process, decellularized bone tissues were assessed by histological stainings. Histological imaging of both native and decellularized bone tissues was stained with Hematoxylin-eosin (HE), Masson trichrome (MT) and Alizarin red (AR) for the assessment of general morphology, collagen structures and mineralisation sites, respectively (Figure 3.2). In native bone, cells were observed in the lacunae around the osteon structures, as seen in HE staining. MT staining indicates the collagen structures as blue in colour; they are distributed partly inside the structure. Mineralisation sites of the bone are seen as red/brown in AR staining. After 0.05% SDS treatment, it was observed that bone samples still have cell nuclei and cells that were not completely removed from the tissue. In addition, MT and AR stainings show a similar histoarchitecture with the native bone.

In the 0.1% SDS treated samples, it was observed that the cells were removed from the bone tissue without damaging the collagen structures. In addition, the mineralisation sites of the bone were still preserved and showed structural similarity with natural bones. Despite the removal of cells, the bone histoarchitecture was damaged after 1% SDS treatment. Empty lacunae, however, were observed, collagen structures were damaged and mineralisation sites decreased after 1% SDS treatment, which indicates destructive decellularization. Histological staining results demonstrate that the optimum detergent concentration is 0.1% SDS, which ensures the removal of cells from bone tissue without any damage to tissue histoarchitecture.
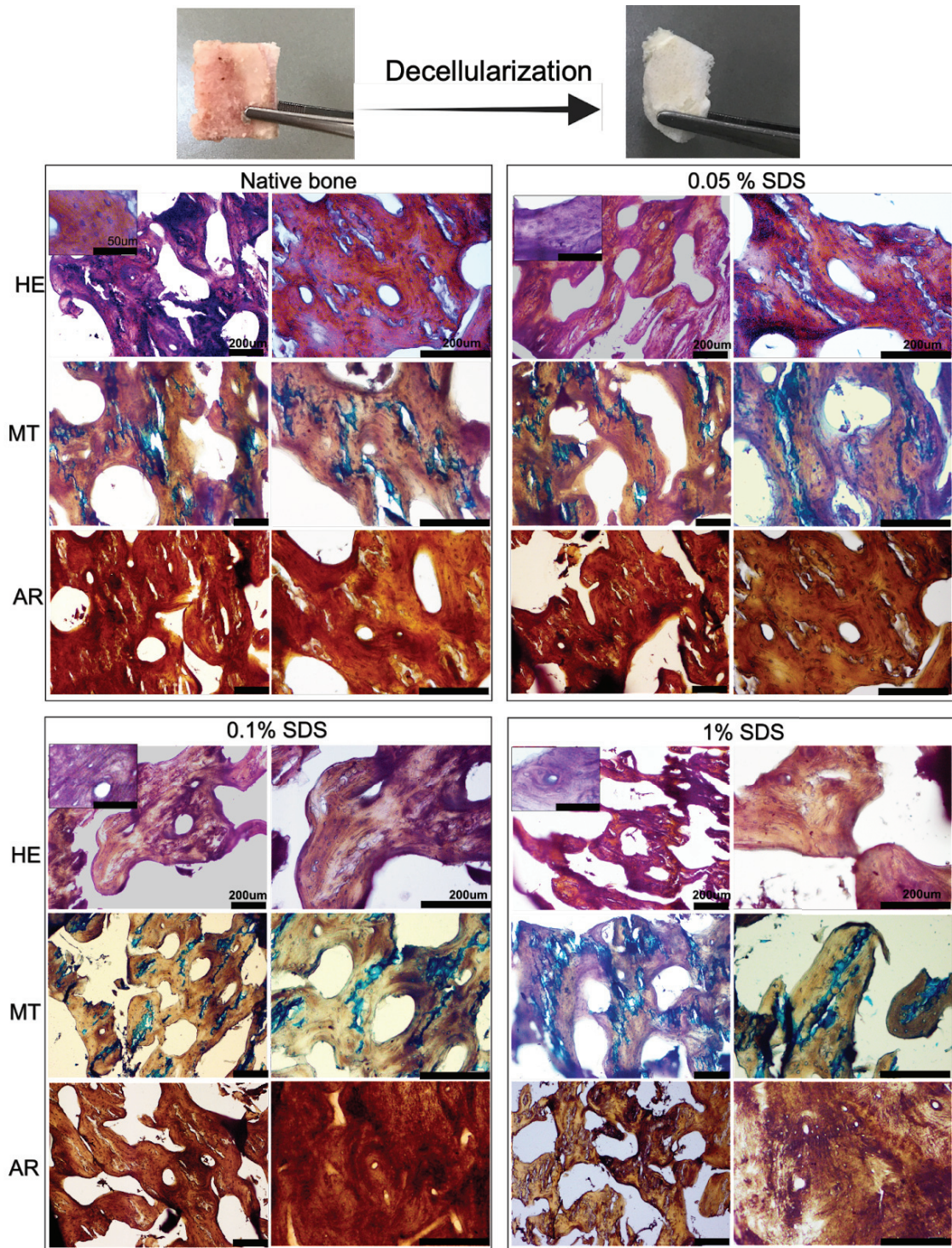
Figure 3.2. Histological staining results of native and decellularized bovine bone tissues. Images show the HE, MT and AR staining after the decellularizstion process in three different SDS concentrations. Scale bars: 200 μm and 50 μm (for inlets).

In addition to histological stainings, native and decellularized bone tissues were evaluated by biochemical analysis. The amount of total DNA, collagen and GAG in the tissues before and after decellularization were determined (Figure 3.3). Consistent with the histological results, the higher DNA amount was detected in 0.05% SDS treatment group and less DNA was measured in the 0.1% and 1% SDS treatment groups. Statistically significant differences were found when compared to the native bone samples. It was reported that the upper limit of the DNA content for complete decellularization is 50 ng DNA[75]. In native bone samples, 95.51 ng/mL DNA was measured. After decellularization, the DNA content of the bone samples was measured as 54.18 ng/mL, 7.90 ng/mL and 5.68 ng/mL for the 0.05%, 0.1% and 1% SDS treatment groups, respectively (Figure 3.3). 96% DNA reduction in DNA content was achieved with 0.1% SDS treatment indicating effective decellularization.

Preservation of the ECM proteins is another essential criterion for an effective decellularization process. Therefore, collagen and GAG contents of bone tissues were detected biochemically. The total collagen content of the bone tissues did not change in either the 0.05% or the 0.1% SDS treatment, but 1% SDS treatment caused a decrease in collagen content, and statistically significant differences were found (Figure 3.3). The total GAG content of bone tissue treated with 0.05% and 0.1% SDS groups did not change and had no statistical differences (Figure 3.3). 1% SDS treatment, however, decreased the amount of GAG in bone tissues, and a statistical difference was found compared to the native bone, which indicates that the ECM structure of the bone tissue was damaged. Biochemical test results demonstrate that removal of the cellular components from the tissue without damaging the ECM proteins could be possible with 0.1% SDS treatment.
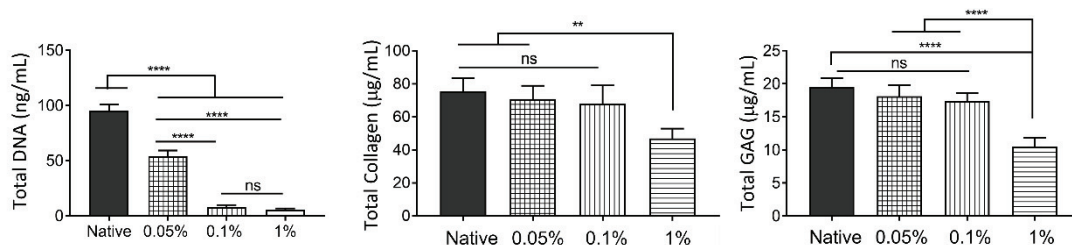
Figure 3.3. Biochemical analysis results of native and decellularized bovine bone tissues. The measurements were performed using six replicates of samples (n=6). **p<0.01, ***p<0.001 and ****p<0.0001 indicate statistical differences of means in comparison to bone.

Bovine bone tissue was decellularized successfully with our decellularization method with a concentration of 0.1% SDS which is the lowest concentration for bone decellularization in comparison to the studies existing in the literature[17,18,76,89]. Histological stainings and biochemical test results demonstrate that bone tissue histoarchitecture was not affect during removal of the cells. Therefore, rabbit and rat bone samples were decellularized using 0.1% SDS and evaluated for the verification of the decellularization process.

3.2.2. Decellularization of Rabbit and Rat Bone Tissues

HE images of the rabbit and rat bone tissues show that round-shaped osteoblasts were distributed homogeneously on the untreated fresh rat and rabbit bone tissue before decellularization (Figures 3.4 A and 3.4 B). In Figure 3.4, black arrows indicated cell nuclei in native bone tissues, both rat and rabbit. After decellularization, cells localised in the osteon structure were removed from the rat and rabbit bones, and the lacuna of the cell was observed as empty. In addition, circular osteon structures, which are important for cell localisation and provide mechanical support to the bone tissue, did not affect after decellularization (Figure 3.4 C).

In addition to the Hematoxylin & eosin staining, collagen structures of the bone tissues were stained with Masson trichrome and then observed with light microscopy. Radial and circumferentially oriented collagen fibrils were observed as dark blue in colour in both decellularized and native bone tissues. Histological images revealed that the collagen structures were preserved after decellularization in rabbit and rat bone tissues and were observed around empty lacuna (Figure 3.5A, 3.5B).
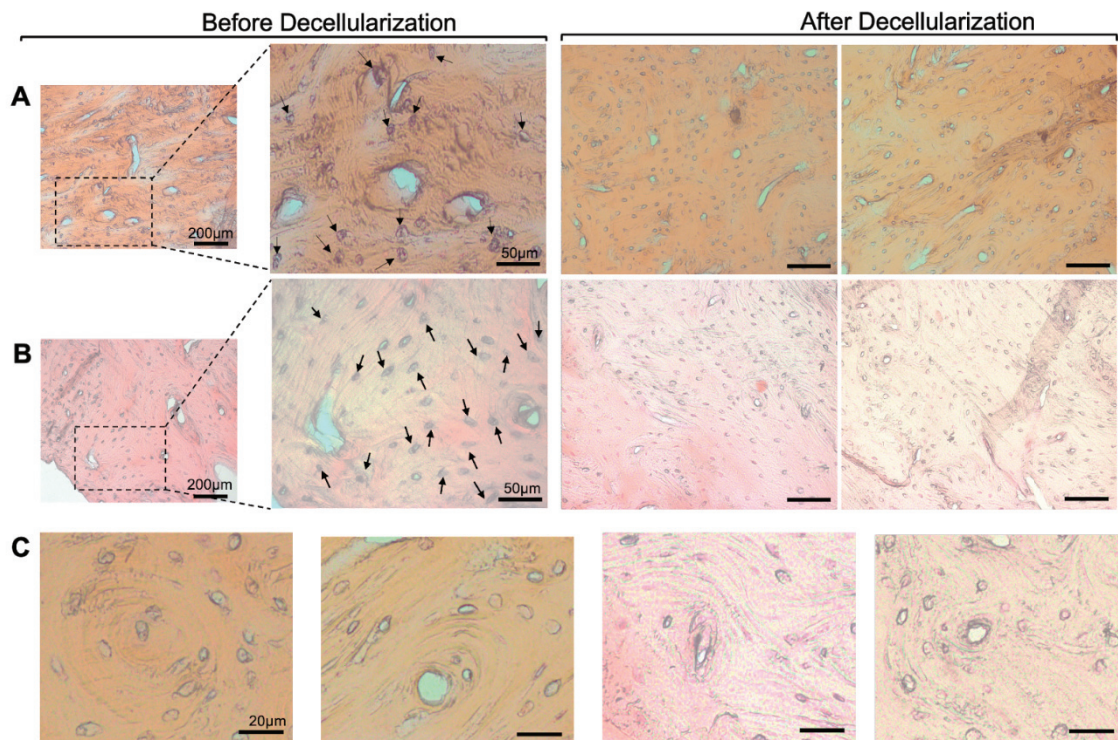
Figure 3.4. Hematoxylineosin staining of rabbit (A) and rat (B) bones before and after decellularization showing cell nucleus (black arrows) inside the tissue before decellularization, and empty lacunae after decellularization. (C) Additionally, osteon structures are shown in higher magnification. Scale bars: 200 μm, 50 μm (left to right for A and B), 20 μm (left to right for C).

Mineralisation is the distinctive feature of bone tissue, but many decellularization studies have not considered this feature. The inorganic content of the bone is essential for osteoinductivity; therefore, removal of inorganic content causes insufficient cellular functions during bone regeneration. To provide osteogenic activity and osteoinductivity after decellularization, we examined the mineralisation sites of both native and decellularized bone tissues. Mineralisation sites were observed in Alizarin Red S staining as a red/brown colour (Figure 3.6). Mineralisation sites around the osteon structures were observed clearly in rabbit bone tissue before and after decellularization, and results showed no change in the tissue structures after decellularization. In rat bone tissue, a partially irregular structure was observed, but mineralisation sites showed a brown colour and did not change after decellularization.
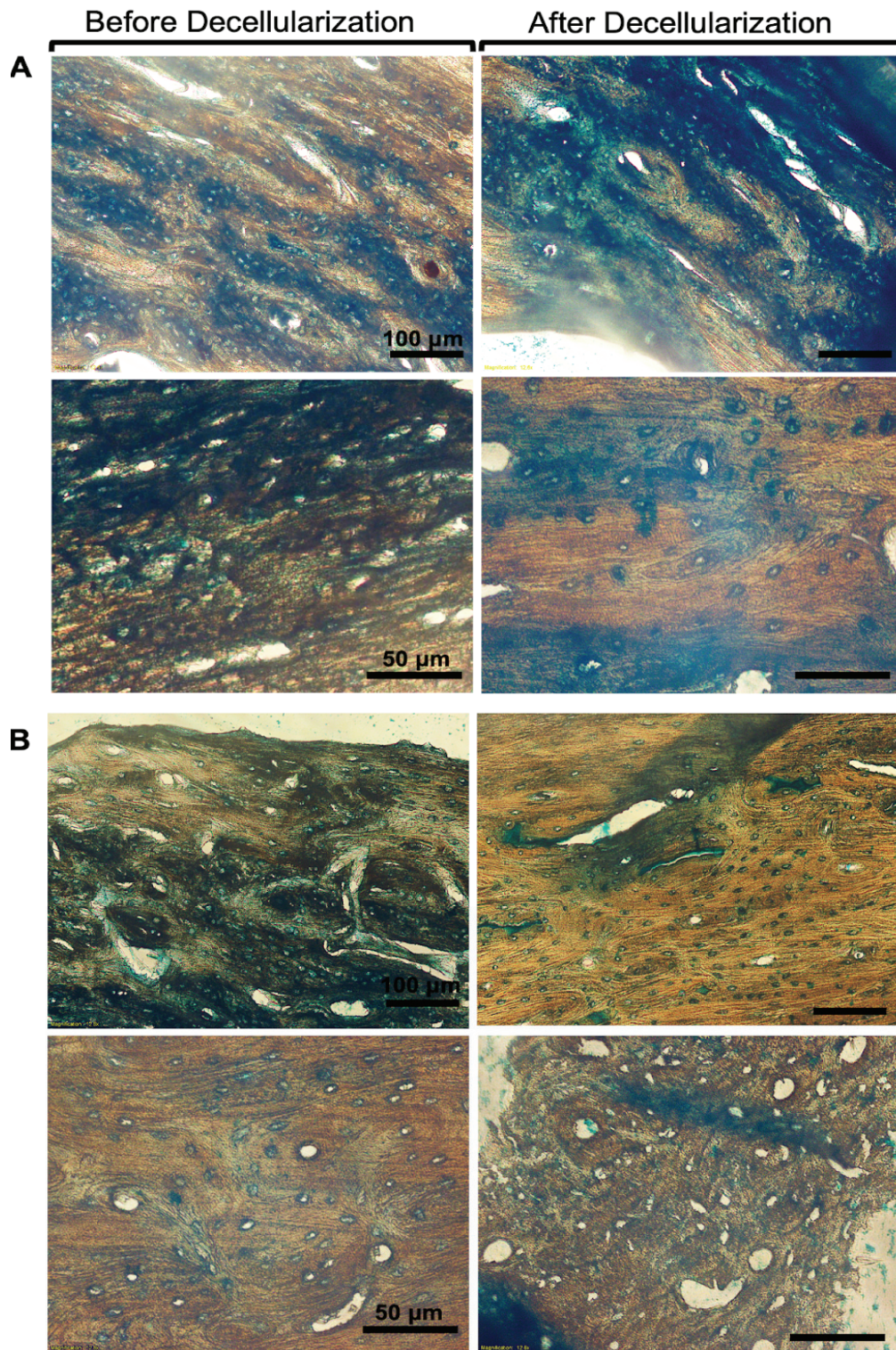
Figure 3.5. Masson trichrome staining of rabbit (A) and rat (B) bone tissues before and after decellularization. Images show the presence of collagen structures inside the bone tissues even after decellularization which confirmed the preservation of the ECM during decellularization. Scale bars: 100 μm (first row) and 50 μm (second row).
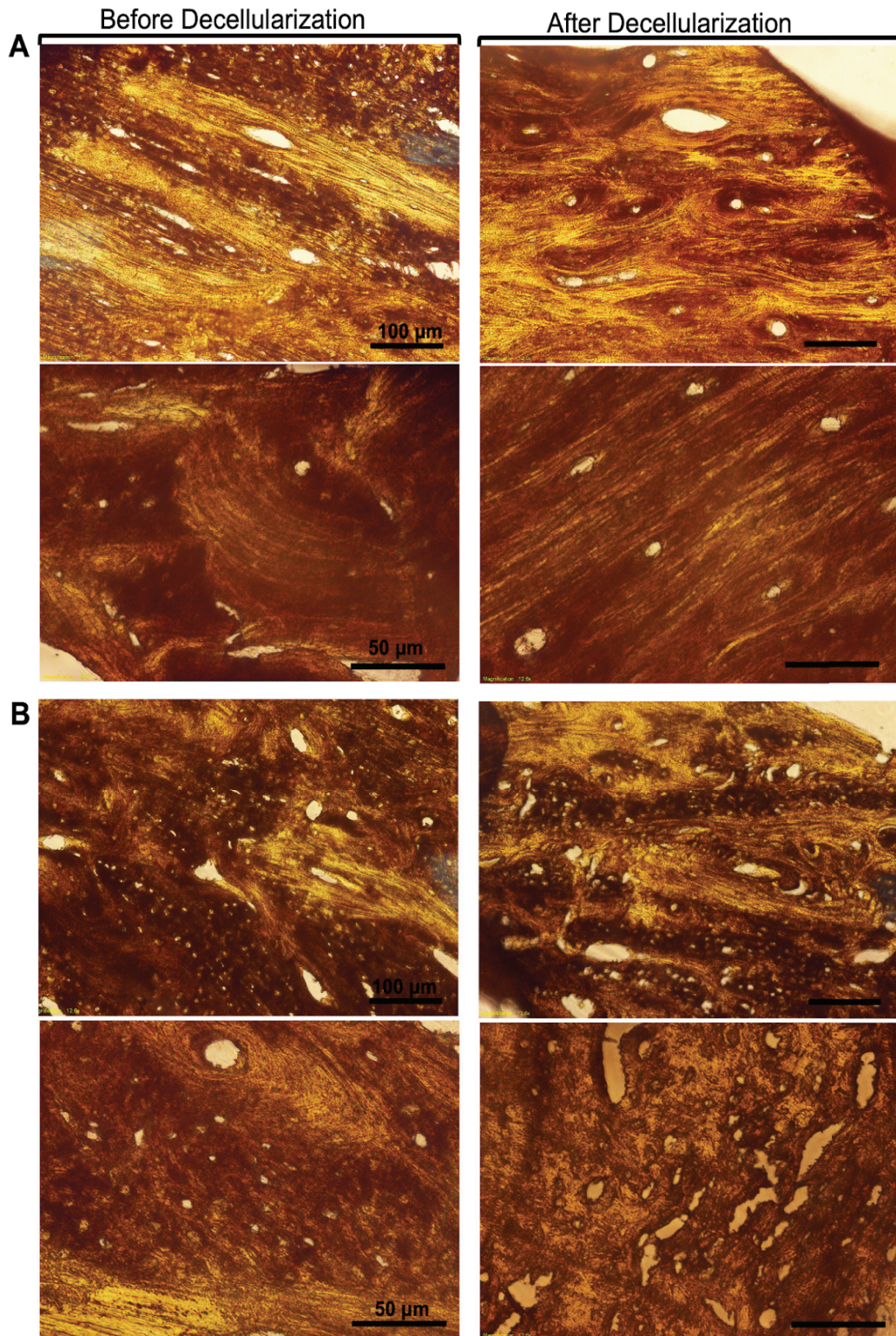
Figure 3.6. Alizarin Red S staining of rabbit (A) and rat (B) bone tissues before and after decellularization showing the mineralization sites of the bone as a brown colour. Scale bars: 100 μm (first row) and 50 μm (second row).

Histological staining results revealed that cellular components were successfully removed from bovine, rat and rabbit bone tissues with a combination of physical, chemical and enzymatic methods using 0.1% SDS, and the decellularization process did not affect the histoarchitecture of the bone tissues.

Total DNA, collagen and GAG content of bone tissues were determined before and after decellularization. The DNA content of both rabbit and rat bone tissues was determined. The total DNA content of rabbits was measured as 81.13 ± 12 ng/ml and 8.02 ± 04 ng/ml before and after decellularization, respectively (Figure 3.7A). In rat bones, the total amount of DNA was measured as 29.92 ± 8 ng/ml and 4.93 ± 2 ng/ml before and after decellularization, respectively (Figure 3.7B). After decellularization, the DNA content of the bone tissues decreased, and statistically significant differences were detected. For confirmation of the decellularization process, DNA content is an essential criterion. After decellularization, the total DNA content of rabbit and rat bone was detected as 3.57 ± 0.99 ng/ml and 2.38 ± 1.18 ng/ml, respectively, and the DNA content obtained in this study was much lower than the recommended upper limit[75]. Laker et al. reported that combining the detergents is more effective than using SDS alone. In Laker's method, SDS is not an optimal detergent for decellularization since SDS had seriously affected the ECM[119]. In our method, however, 0.1% SDS was the optimum concentration for the successful decellularization of the bone, and a 96% and 93% reduction in DNA content for rabbit bone and rat bone, respectively, was achieved.

The total collagen content of the bone tissues was determined by the spectrophotometric method, depending on the amount of hydroxyproline. As shown in Figure 3.7A, the total collagen amount of rabbit bones was measured as 56.71 ± 3 mg/ml before decellularization and 48.72 ± 10 mg/ml after decellularization. In rat bones, it was measured as 39.84 ± 7 mg/ml before decellularization and 35.63 ± 10 mg/ml after decellularization (Figure 3.7 B). No statistically significant difference was found between samples before and after decellularization, confirming that the collagen structures were not affected by our decellularization method. Previous studies showed that treatment with SDS or Triton X-100 has a lower effect on ECM compared to trypsin[120,121]. Decellularization with trypsin resulted in the loss of ECM components. In addition, both chemical and enzymatic treatments have much lower effects on the loss of collagen [121]. With the combination of the histological Masson trichrome staining and

collagen measurement, it could be said that 0.1% SDS did not significantly affect collagen structure.

GAG amounts of tissues were evaluated spectrophotometrically with a 1.9 dimethyl methylene blue (1.9 DMMB) test. The total GAG amount of rabbit bones was measured as 18.99 ± 17 mg/ml before decellularization and 16.92 ± 11 mg/ml after decellularization (Figure 3.7A). In rat bones, it was determined as 11.88 ± 21 mg/ml before decellularization and 8.63 ± 14 mg/ml after decellularization (Figure 3.7B). In addition, no statistically significant differences were detected. Supporting the Alcian blue staining results, GAG proteins were preserved after decellularization. Different decellularization methods in the literature showed various effects on the ECM molecules; several detergent treatments, such as SDS and Triton X-100, resulted in the reduction in GAG contents[74,122,123]. Xu et al. used three different detergents such as 0.5% trypsin, 0.5% SDS and 3% Triton X-100 for annulus fibrous tissue. It was reported that trypsin treatment resulted in the lowest GAG content, followed by SDS and Triton X-100, and successful decellularization while maintaining its macroscopic structure was detected in the Triton X-100 group[73]. In our decellularization method, no significant loss was detected in either collagen or GAG content, which indicates the preservation of the ECM with minimum SDS concentration, according to the literature.
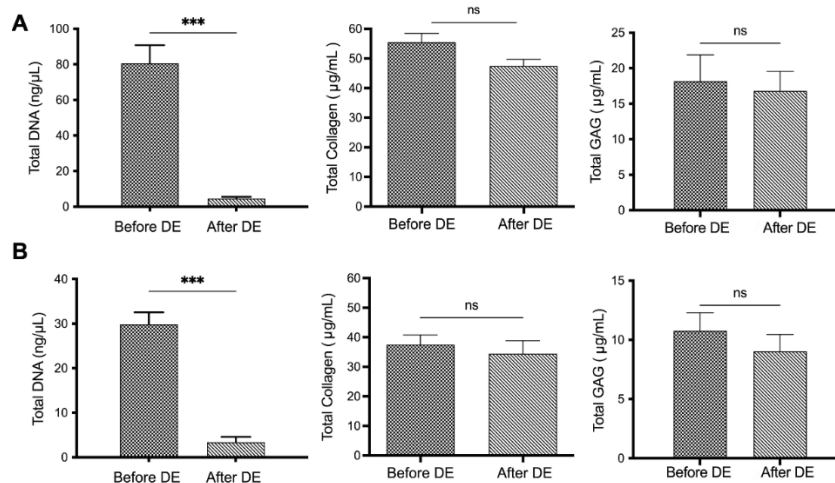
Figure 3.7. Biochemical analysis results of rabbit (A) and rat (B) bones before and after decellularization. The analyses were carried out using six replicates of the samples (n=6). ***p<0.001 indicates statistical differences of means in comparison to bone samples before and after the decellularization process. (DE: Decellularization)

According to the biochemical test results, the DNA content of the bone tissue is significantly decreased without any significant influenced on the ECM proteins and total collagen and GAG amounts were preserved by our decellularization method. It is confirmed that 0.1% SDS concentration is optimum for effective decellularization of bovine, rabbit and rat bone tissues.

3.2.3. Comparison of Mechanical Properties

Maintaining structural stability is another essential part of the decellularization process. Decellularized biological scaffolds provide a structural similarity of biochemical and biomechanical properties to guide cell attachment, proliferation and migration in the recellularisation process. Therefore, native and decellularized bone tissues were assessed with a compression test for the determination of biomechanical properties. The maximum compression force that can be applied on the untreated bone tissue was determined as 232.65 ± 25 N, 162.02 ± 11.81 N and 49.78 ± 8.72 N before decellularization for bovine, rabbit and rat bone tissues, respectively. These numbers were slightly reduced to 220.23 ± 16 N, 153.83 ± 10.57 N, and 42.72 ± 9.53 N after decellularization (Figure 3.8). There were no statistically significant differences between the maximum force values of untreated and decellularized bone tissues. The compression strength of the untreated bovine, rabbit and rat bone tissues was determined as 243.42 ± 22 MPa, 37.95 ± 2.15 MPa and 21.69 ± 1.21 MPa, respectively. After decellularization, the compression strength of the bone tissues was not significantly changed and there were no statistical differences before and after decellularization (Figure 3.8). In addition, Young's modulus of the bones was determined as 28.14 ± 32 MPa, 12.61 ± 21 and 7.72 ± 10 MPa before decellularization. The Young's modulus of both bone tissues was not significantly changed after decellularization. Besides, no statistically difference was found for Young's modulus, which confirm that the decellularization process was not affected biomechanical properties of the bones (Figure 3.8). Decellularization of different type of tissues using SDS caused significant loss of GAG[74,123] which is one of the main component for biomechanical properties of bone[124]. Maintaining of the mechanical strength and young modulus after decellularization which directly related with the preservation of the collagen fibers and GAG structure as described in the study by Xu et al. [125].
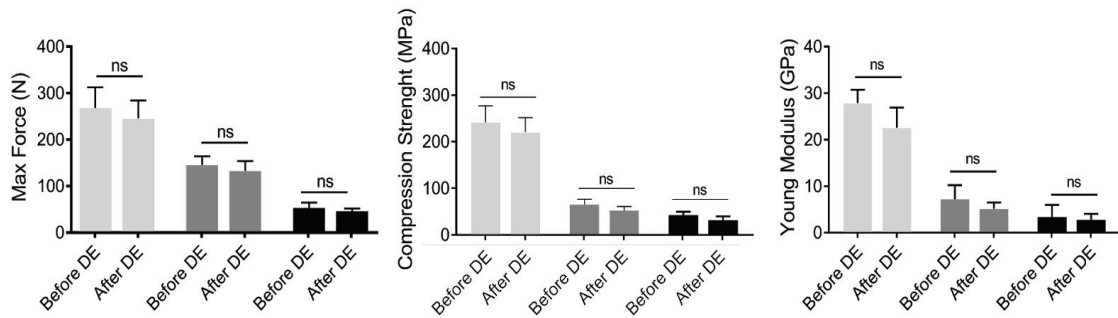
Figure 3.8. Biomechanical test results of bovine, rabbit and rat bone tissues before and after decellularization. Mechanical tests were performed using six replicates of samples (n=6). ns: no statistical differences of means in comparison to bone samples before and after the decellularization process. (DE: Decellularization)

3.2.4. Fluorescence Microscopy and SEM Analysis

To evaluate the nuclei in bone tissues DAPI staining was used and observed with confocal microscopy. Fluorescence images showed that cell nuclei in the untreated rabbit and rat bone tissue and, as expected, no cell nuclei were found in bone tissues after decellularization (Figure 3.9). Similar to histological results, fluorescence imaging demonstrated that cellular components of the bone tissues were separated successfully by our decellularization process.

The surface morphology and cross-sectional area of the bones were observed by SEM analysis before and after decellularization. In the SEM images of native bone tissue, Haversian canals in the middle of the osteon structures and canaliculi are seen on both rabbit and rat tissues (Figure 3.10). In addition, the pore structure of spongious bone in bovine bone tissue is shown. SEM images demonstrated that the general morphology of the bone surface did not change after decellularization. Collagen fibers in decellularized tissues were also shown at higher magnification, demonstrating the preservation of micro-histoarchitecture of bone.
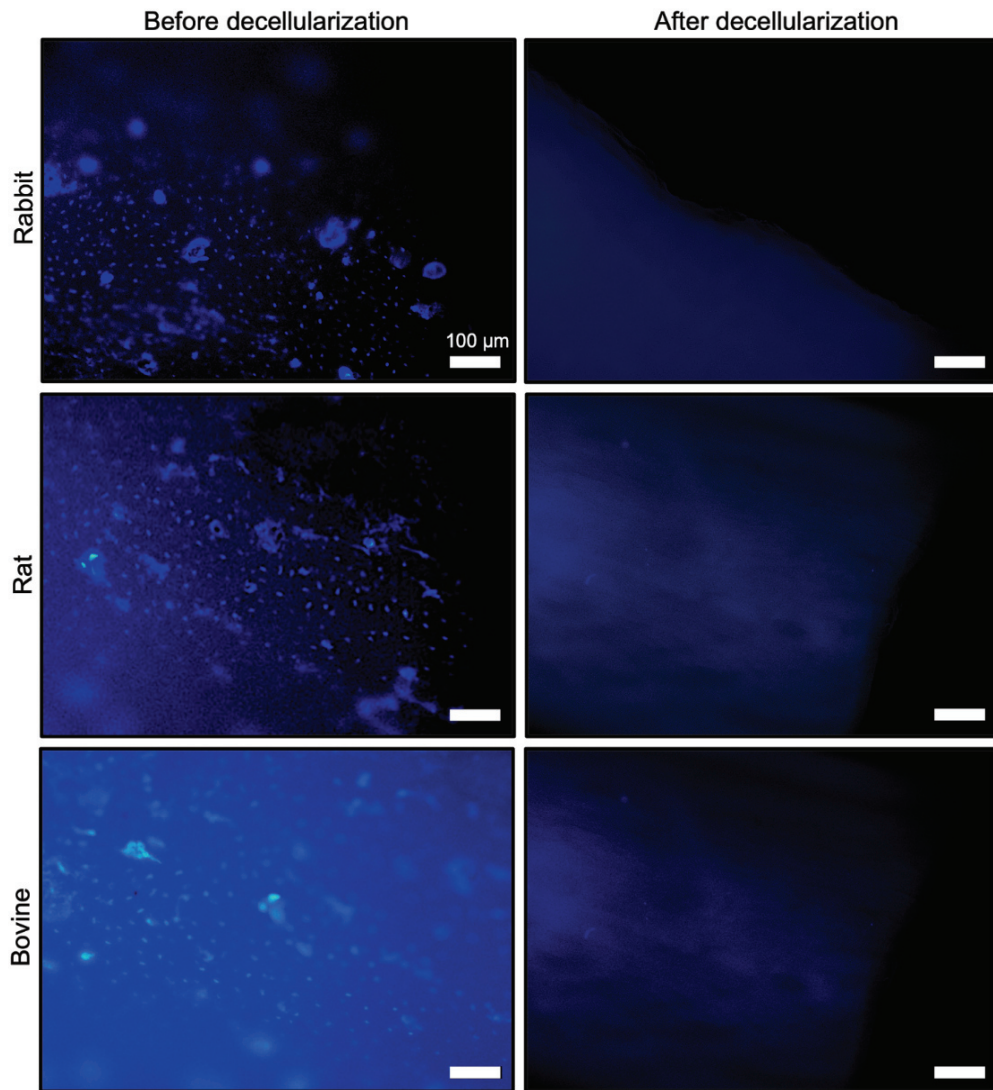
Figure 3.9. Fluorescence imaging of bone tissue before and after decellularization. Scale bars: 100 μm. DAPI: nucleus (blue).
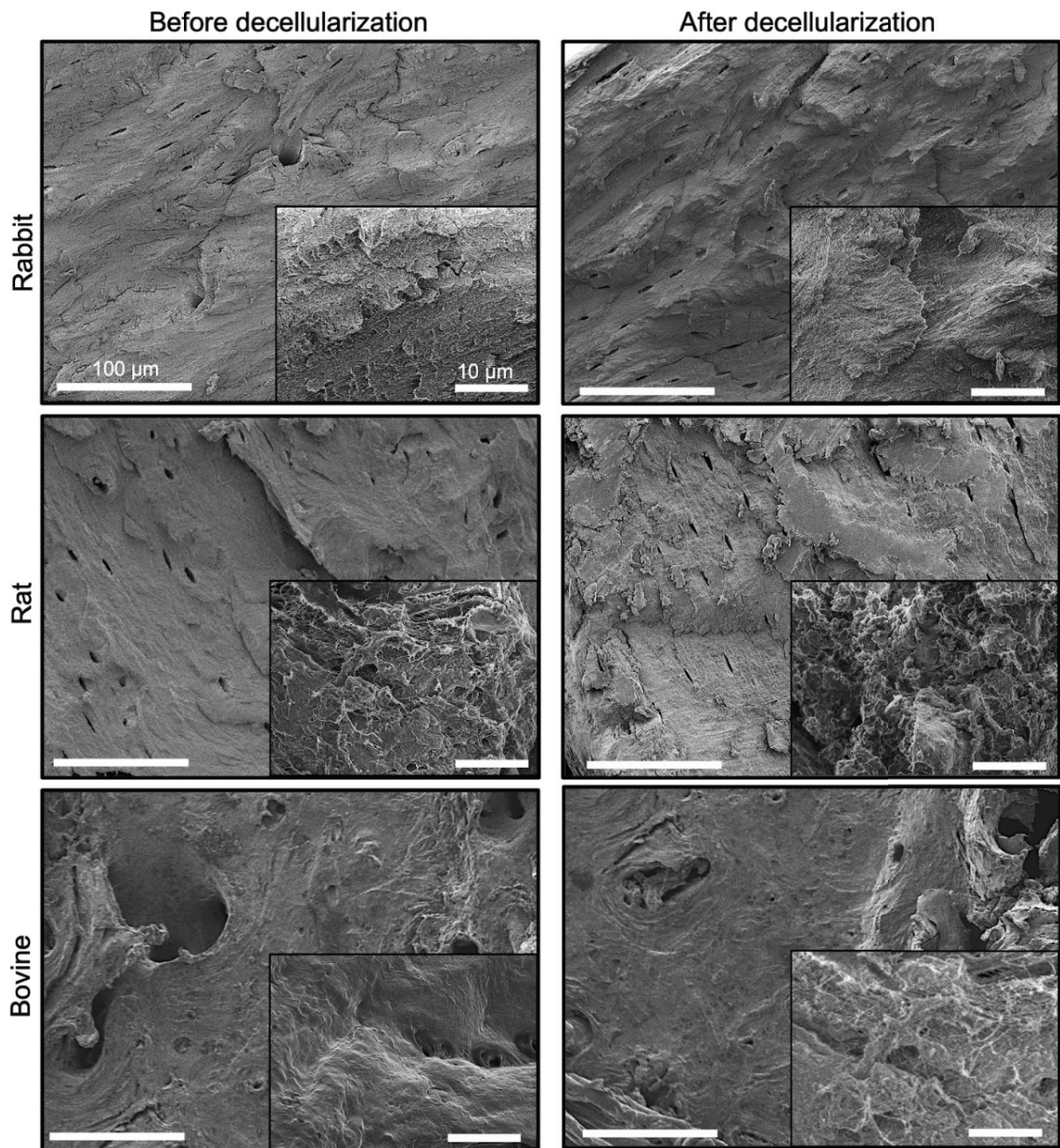
Figure 3.10. SEM images of bone tissues before and after decellularization show the surface morphology of the bone tissues and fibrillar collagen structure in the cross-sectional area. Scale bars: 100 µm and 10 µm (inlets).

3.3. Conclusions

Decellularized biological materials as tissue-specific scaffolds exhibit great potential for repairing and regenerating tissues and organs. For bone-tissue engineering, the decellularization method could provide a biomimetic scaffold candidate for bone-tissue regeneration due to its structural and mechanical features as well as the lack of immunogenic reactions. Several studies have reported regarding the decellularization of bone tissue with different detergents and different techniques. Using high detergent concentrations (0.5%, 1%) and applying a demineralisation process in addition to decellularization, however, could damage the natural ECM structure and affect the biomineralisation property which is unique for bone tissue.

In this chapter, we defined an effective decellularization method to prepare a biological bone ECM for bone regeneration. Our decellularization process consists of physical, chemical and enzymatic methods and allows for the removal of the cellular components from bone tissue by using a minimum chemical concentration without demineralization step. 0.1% SDS, the lowest concentration for bone decellularization in comparison to the studies existing in the literature, was chosen as an optimum detergent concentration. Histological observation results revealed that cellular components were removed from bone tissues, and collagen structures around empty lacuna were maintained in decellularized bovine, rabbit and rat bone tissues. Moreover, mineralisation sites, a unique feature of bone tissue, were observed after decellularization. Biochemical test results showed that the DNA content of the bone tissue significantly decreased, and a 96% reduction in DNA content was achieved with 0.1% SDS treatment, indicating effective decellularization. Total collagen and GAG amounts did not significantly decrease, which confirmed that 0.1% SDS concentration is optimal for the effective decellularization of bovine, rabbit and rat bone tissue. In addition, neither compression strength nor Young`s modulus changed with decellularization, proving that structural stability was maintained.

In conclusion, the results demonstrate that our decellularization method is effective for developing biological bone ECM containing both organic and inorganic compounds using a minimum concentration of SDS. It is foreseen that the obtained decellularized bone could be used as a biological substitute for bone-tissue engineering applications and would provide a favourable microenvironment for bone regeneration.

CHAPTER 4

DECELLULARIZED BONE INCORPORATED GELATIN BIOINKS

Additive manufacturing technology enables the development of three dimension (3D) structures for mimicking the complex structure of tissues by combining the principles of engineering, material science and biology. In this approach, 3D constructs are fabricated by a computer-aided manufacturing technique to pattern and assemble both living and non-living materials using cells and biological materials, termed 'biofabrication'. Biofabrication has excellent potential in tissue engineering and regenerative medicine by allowing the fabrication of biologically functional products from living cells, tissues, bioactive molecules and biomaterials through bioprinting[126].

For bone-tissue engineering applications, various studies have already been demonstrated as biomaterial inks or bioinks, including natural or synthetic polymers, such as alginate, collagen, gelatin, gelatin methacryloyl, hyaluronic acid, poly (lactide-co-glycolic acid), poly (e-caprolactone) and poly (ethylene glycol). Among these polymers, gelatin (GEL) has various advantages and is preferable due to its biocompatibility, nontoxicity and biodegradability[127–129]. In addition, the presence of an arginine-glycine- aspartic acid (RGD) sequence, which is described as a cell recognition motif in the protein structure, induces the biological compatibility of GEL in comparison to synthetic polymers that lack RGD cell recognition sequences[130]. In addition, GEL has been recognised as a Generally Regarded as Safe (GRAS) material by the United States Food and Drug Administration (FDA)[131]. In 3D printing applications, GEL is a favourable material due to its thermosensitivity and gelation properties by induced lower temperature[132,133]. Moreover, GEL can easily dissolved in water-based solution and crosslinked through chemical agents, such as glutaraldehyde[134], genipin[135,136], carbodiimides[137] and enzymatic treatments, such as transglutaminase[138] and horseradish peroxidases[139]. Among these crosslinkers, transglutaminase crosslinking improved cellular behaviour and exhibited better performance in terms of porosity, mechanical strength, cell adhesion and proliferation[140].

In 3D printing applications, maintaining 3D structure as a shape fidelity of the constructs while allowing cell proliferation is essential. The inferior mechanical properties of the 3D-printed constructs and low shape stability are the main disadvantages in 3D printing applications[105]. To overcome this limitation, mechanical properties can be enhanced using chemical treatments[141–144] or the addition of fillers[145,146]. As a filler material, tissues can also be treated by several methods to obtain natural-based compositions of extracellular matrix (ECM) with a high mimicry of the native tissue. A design of biomaterial inks containing native ECM components (e.g. hydroxyapatite, collagen, proteoglycan and growth factor) present in bone is a crucial strategy to develop functional scaffolds. At this point, decellularization techniques could be combined with 3D printing techniques to obtain biomaterial inks. The primary advantages of a decellularization technique is to maintain the physical characteristics of the tissues or organs and preserve the natural ECM components to promote cell behaviour during the recellularisation process[87,122]. With the advantages of the decellularization technique, decellularized tissues have the potential for a biofabrication approach. Decellularized bone (DB) has been used in various tissue-engineering applications, including the direct use of the DB as an ECM substitute, solubilisation of the DB-ECM as hydrogels[18] and pulverisation to obtain as particle[147]. Particles can be used as a reinforcement material within a hydrogel matrix; thus, it might be possible to develop and strengthen biomaterial inks. To the best of our knowledge, there has been no study on the use of DB particles (containing both organic and inorganic components of bone) in GEL matrix for 3D bioprinting. The advantages of both decellularized ECM and the highly cytocompatible GEL could allow for the production of a better biomaterial formulation for bone-tissue engineering applications. This chapter demonstrates the development of 3D-printed composite scaffolds and 3D-bioprinted composite bioinks composed of GEL and DB particles from rabbit and bovine for bone tissue engineering applications. For the bioink formulation, two cell types mouse pre-osteoblasts (MC3T3-E1 cells) and human telomerase reverse transcriptase (hTERT) expressing mesenchymal stem cells (MSCs) were used. The stability of the 3D-bioprinted constructs was maintained by crosslinking with microbial transglutaminase (mTG). 3D-printed constructs were cultured for 28 days and characterized in terms of cytocompatibility and bioactivity as well as morphologically, mechanically and chemically for potential application in bone-tissue engineering.

4.1. Materials and Methods

DB particles obtained from rabbit and bovine were added to GEL to prepare biomaterial ink. Firstly, DB tissues (described in *Chapter 3*) were pulverized using a laboratory mixer and filtered with 100 μm and 45 μm mesh diameters. Thus, two different DB particle types and sizes were obtained. 15% (w/v) GEL (from porcine skin, Type A, Sigma) was dissolved in ultrapure water at 80 °C for three h. For the sterilization, GEL solution was filtered using a 0.02 μm filter, and DB particles were sterilized by gamma sterilisation. GEL and DB particles were mixed at 37 °C for 10 min by stirring, resulting in a final concentration of 7.5 % GEL and 5% and 10 % (w/v) DB particles. Finally, different concentrations of DB particles (1%, 3%, 5% and 10% (wt%)) and two different particle sizes (45 μm and 100 μm) were prepared in order to evaluate the effects of DB particles into the GEL matrix. For the bioink composition, hTMSCs and MC3T3-E1 cells were used, and cell pellet (5×10^6 cells/ml) was prepared by centrifugation at 1250 rpm and then mixed with DB incorporated GEL hydrogel precursor (GEL/DB) using a mixing unit (Sophie et al., 2021). Prepared bioinks were bioprinted using a 3D extrusion bioprinter (Bioscaffolder 3.1, GeSiM, GmbH, Germany). The cartridge holder temperature was set to 25 °C to stabilize the viscosity. Bioinks were transferred into the cartridge and extruded through a 410 μm diameter conical needle with a tip velocity of 5–10 mm/s. The scaffolds were fabricated in a cylindrical shape with 10 layers. After printing, 10% microbial transglutaminase (mTG ; Ajinomoto ACTIVA WM, 85−135 U/g) was used as a crosslinker to stabilise the scaffolds. After washing twice, cell-laden scaffolds were placed inside the incubator. Bioprinted cell-laden scaffolds were cultured in αMEM (for MC3T3-E1 cells), DMEM (for hTERT-MSCs), containing 1% (v/v) L-glutamine, 10% (v/v) FBS and 1% (v/v) penicillin-streptomycin (Sigma Aldrich, all supplements) for 28 days at 37 °C in an incubator with humidified atmosphere of 5% CO and 95% humidity. For the osteogenic induction (+OS), 0.05mM ascorbic acid 2-phosphate, 10^{-7} M dexamethasone and 10 mM beta-glycerophosphate were added to the cell culture medium, and osteogenic differentiation of cells was induced starting from day one of the culture period. 3D-printed scaffolds were characterized in terms of printability as well as rheological, morphological, degradation and mechanical properties, and cytocompatibility, proliferation and osteogenicity of cells inside the 3D-bioprinted scaffolds were assessed.

4.2. Results and Discussions

4.2.1. Rabbit DB Particles Incorporated-GEL Biomaterial Inks

4.2.1.1. Rheological Assessments

In the context of 3D printing, biomaterial inks need to have specific properties: for instance, extrudability, viscosity, shear thinning behaviour and crosslinking capability to retain their shape fidelity[148]. The viscosity of the biomaterial ink is one of the critical parameters that depend on the polymer's concentration and molecular weight for the 3D printing process. Shear thinning behaviour is directly related to the viscosity behaviour of the ink with respect to shear rate. The viscosity of the biomaterial ink would be excessively high to be extruded through the nozzle without shear thinning behaviour[149]. Therefore, the rheological properties of the GEL and GEL/DB incorporated hydrogel precursors were assessed. Figure 4.1 shows the shear and temperature-dependent measurements of hydrogel precursors. According to the shear dependence measurements, the results indicate the elastic (solid) and viscous (liquid) states of the precursors. At their initial measurement points, precursors showed a gel state, represented by a dominating storage modulus. When the deformation was increased, precursors became more viscous, indicating a loss modulus increase. The flow point was reached when precursors deformed by over 500–600%, indicating that viscous behaviour starts to dominate. All GEL/DB precursors have similar flow points and deformation behaviour, as summarised in the shear stress graph (Figure 4.2). Temperature-dependent measurements showed that the sol-gel state was similar in all groups and was not dependent on the concentration of the particle, which indicates that the particle concentration did not influence printability. Thixotropy describes the structural recovery of the materials necessary for layer-by-layer formation in the 3D printing process. The DB-incorporated hydrogel precursors showed self-recovery properties with similar thixotropic behaviour and a slightly higher storage modulus (Figure 4.1).
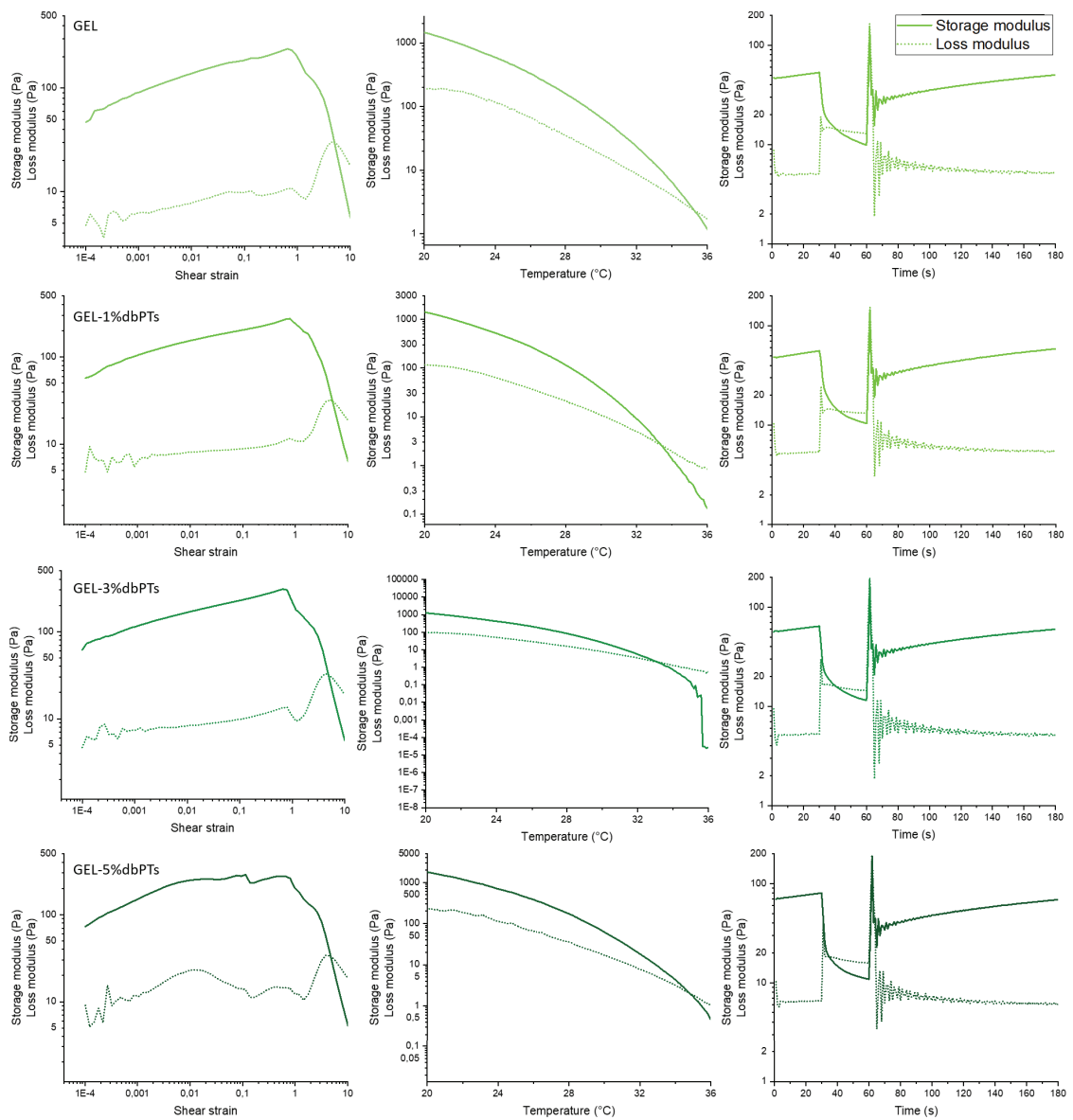
Figure 4.1. Rheological test results of the GEL and DB-incorporated hydrogel precursors. The rheological tests depending on shear, temperature and time were performed with three sample replicates (n=3), and data are presented as mean[150].
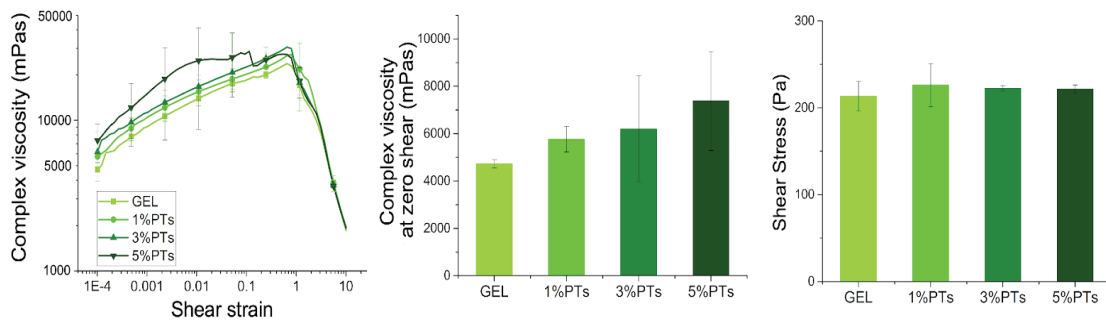
Figure 4.2. Rheological assessment of the GEL, GEL/1%DB, GEL/3%DB, and GEL/5%DB precursors. The tests were carried out with three sample replicates (n=3), and data are represented as mean ± SD[150].

By using the average of the first measurement point, complex viscosity at rest was quantified. The results showed that complex viscosity increased as the concentration of DB particles in the GEL precursor increased (Figure 4.2). The data indicate that adding DB particles slightly increases complex viscosity and shear stress. The data indicate that also shear stress slightly increased with the addition of DB particles (Figure 4.2). The samples representing the flow point for each group (the data obtained from shear dependence measurement showed in Figure 4.1) had similar shear stress. Shear stress at shear rate of 1/s was determined and the values increased slightly in DB-incorporated groups; however, no statistically significant differences were detected (Figure 4.2).

4.2.1.2. Fabrication of GEL/DB Composite Scaffolds

3D-printed composite hydrogels composed of GEL and DB particles were fabricated and crosslinked with mTG after printing. The influence of DB particles incorporation on the 3D structure was assessed using light microscopy images. 1%, 3%, and 5% DB (wt%) incorporated GEL composite hydrogels were fabricated as five layers with cylindrical geometries and 0°/90° strand patterns in a grid structure, resulting in square macropores between the strands. Pure GEL hydrogels were observed as transparent, however, high DB incorporated-GEL hydrogels become opaque and DB particles can be seen as a white colour inside the GEL/DB composite hydrogels (Figure 4.3 A). Additionally, increasing turbidity was observed when the

particle concentration increased in the scaffolds. GEL/5% DB composite scaffolds represented a white colour (opaque; Figure 4.3 A) compared to the transparent pure GEL hydrogels, indicating a higher particle content (Figure 4.3 A).
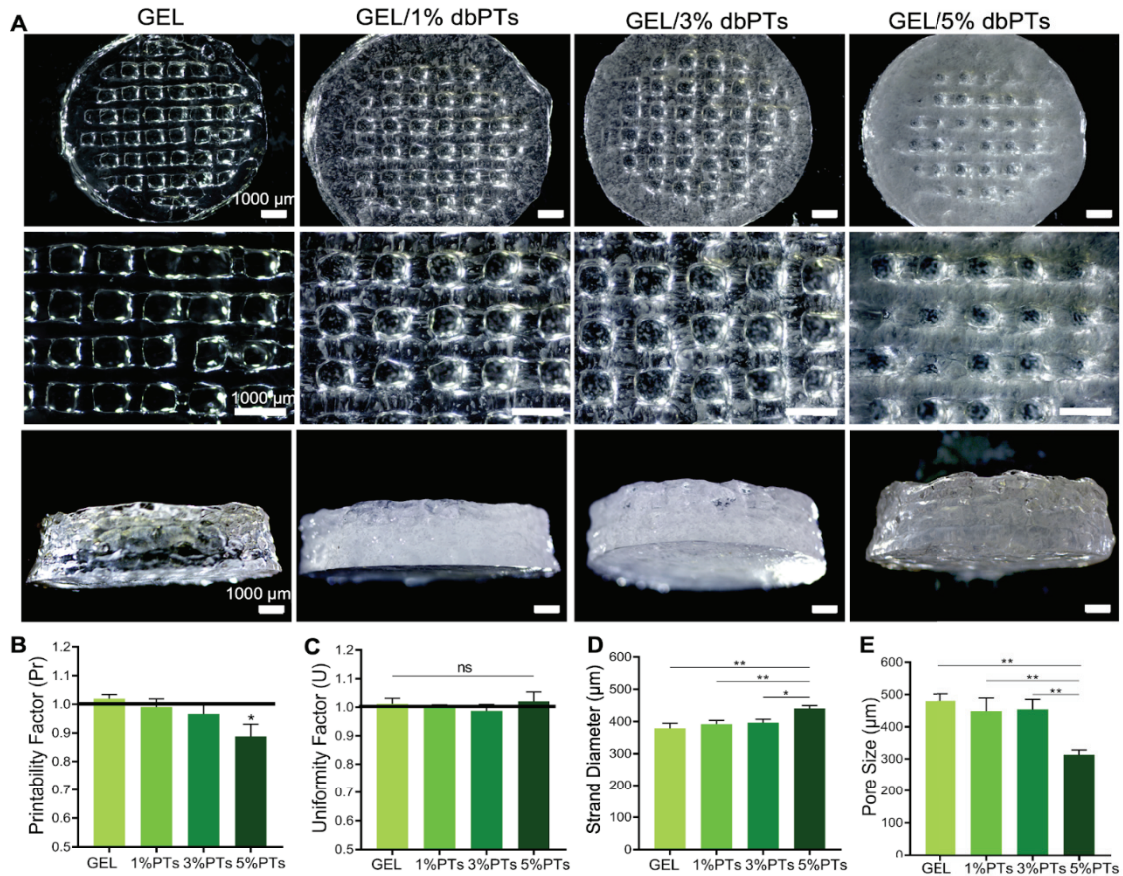
Figure 4.3. 3D-printed GEL and GEL/DB hydrogels. (A) Light microscopy images of the 3D GEL/DB hydrogels in the top and side view after crosslinking. Scale bar: 1000 µm. (B-E) Printability assessments of the GEL/DB (n=4), (B) Printability factor (Pr), (C) Uniformity factor (U), (D) strand diameter, and (E) pore size of the scaffolds. Data are shown as mean ± SD. *p<0.05 and **p<0.01 indicate statistically significant differences of means in comparison to 3D-printed hydrogels by one-way ANOVA tests[150].

The printability and uniformity factors were used to determine the printing accuracy and the results showed that pure GEL hydrogels represent an ideal square pore geometry and uniform strut morphology (Figure 4.3 B, C). The thermal pre-treatment of the GEL at 80°C for 3h resulted in partial hydrolysis of the GEL, improving

printability properties as reported previously[151]. This thermal treatment does not alter the chemical composition of GEL, but it does result in a changed molecular distribution and improved viscosity and shear thinning behaviour for 3D printing of GEL[151,152]. The GEL and GEL/DB biomaterial inks demonstrated successful printability owing to the improvement of the viscosity by the heat treatment of the GEL.

Printability of a bioink is a crucial requirement for the fabrication of 3D scaffolds and is directly correlated with the gelation of the material. As reported by Ouyang et al., extruded filaments exhibited a well-defined morphology, leading to square pores and uniform grids with a smooth surface and consistent width in 3D[115]. In contrast, the extruded filament displays a liquid-like state and the layers may fuse when the material is in an under-gelation condition. For optimal gelation and ideal printability, pore morphology should have a square geometry, recreating the initial G-code structure design[115]. Additionally, the value of the printability (Pr) factor and uniformity (U) factor should be close to one[115,116]. Considering this knowledge, Pr and U factors were calculated to assess the pore circularity and strand homogeneity of the 3D-printed hydrogels. The Pr quantification results showed the pure GEL group (Pr ~1) and hydrogels including 1% and 3% DB demonstrated a similar printability capacity to produce square pores. The Pr factor of the GEL/5%DB scaffolds, however, showed a slight decrease and a tendency for strand fusion, leading to a more circular pore geometry (Pr=0.89) (Figure 4.3 B). The measurements of the uniformity factor revealed that 3D-printed pure GEL and GEL/DB scaffolds have similar uniformity and no statistically significant differences between the scaffold groups for uniformity (Figure 4.3 C).

Additionally, as the amount of particles increased, the strut diameter of 3D-printed hydrogels increased as well. The highest strand diameter was measured in the GEL/5%DB hydrogels (443±3 μm), with statistically significant differences in comparison to other groups (Figure 4.3 D). The pore sizes of GEL and the GEL/1%DB, GEL/3%DB and GEL/5%DB hydrogels were determined as 489 μm, 447 μm, 437 μm and 317 μm, respectively. The GEL/5%DB group had statistically significant differences in comparison to the other groups (Figure 4.3 E). Nevertheless, the pore sizes measured in all groups are suitable for cell attachment, proliferation and migration in bone tissue engineering applications[153]. According to the printability assessment results, GEL and GEL incorporating 1% or 3% DB composite hydrogels exhibited the

most uniform strands with a square pore geometry in comparison to the 5%DB incorporated GEL hydrogels. The printability assessments indicate that the printability is reduced after a threshold of 5%DB, whereas we identified that ≤5% particle concentration is optimum for printability. However, GEL/5% DB concentration still exhibited a Pr factor of ~0.9 ± 0.04, indicating that it could be printed with proper shape fidelity in 3D printing applications[115].

After 3D printing, composite hydrogels were freeze-dried to obtain microporous structures and evaluate the cytotoxicity of the scaffolds and cell behaviour in GEL/DB biomaterial inks. Light microscopy images show the top view of all scaffolds (Figure 4.4 A). Following the freeze-drying process, micropores were formed on the structures and 3D-printed scaffolds exhibited both macro- (~750 μm) and micro-pores (~30 μm). SEM images demonstrated interconnected open micropores on the strands due to the freeze-drying (Figure 4.4 B). The interconnected open porous structures offer a substantial surface area and a favourable environment for cell attachment and support cell proliferation migration, and nutrition transfer. In addition, it is demonstrated that the pore surface of the pure GEL scaffolds is smoother than DB containing scaffolds (Figure 4.4 B). Moreover, the surface roughness was increased in higher DB particle concentration as seen in Figure 4.4 B. The surface morphology and subsequent increase in surface roughness of the scaffolds could be influenced by the fibrous collagen structure and hydroxyapatite content of the particles. According to previous studies, pores with a diameter of ≥ 300 μm are crucial for vascularisation and the connection of the surrounding tissues whereas pores with a diameter ~50 μm are effective for increasing surface area for cell attachment[154–156]. GEL/DB composite scaffolds have macro- and micropores in a range of 20-750 μm which is appropriate for mimicking the bone structure and bone tissue engineering applications. GEL, known as a polydisperse protein, is formed by irreversible acid-base hydrolysis of collagen and shows a chemical composition quite similar to collagen[130]. DB particles also consist of collagen fibers as described in *Chapter 3*. This resemblance could allow interaction and recognition of each other in the same environment. Therefore, 3D-printed GEL/DB composite hydrogels were investigated in terms of particle-polymer interaction by SEM analysis. SEM images show well interaction between DB particles and GEL matrix, notably, as embedded on the pore walls of the structures (Figure 4.4 C). This interaction between GEL and particles indicates the appropriate interface adhesion which could occur

between collagen fibers of DB particles and GEL matrix by secondary interactions[157]. Besides, the identical chemical composition of DB particles and GEL could allow them to behave as a single structure during stabilisation and homogeneous distribution of the DB particles within the GEL matrix.
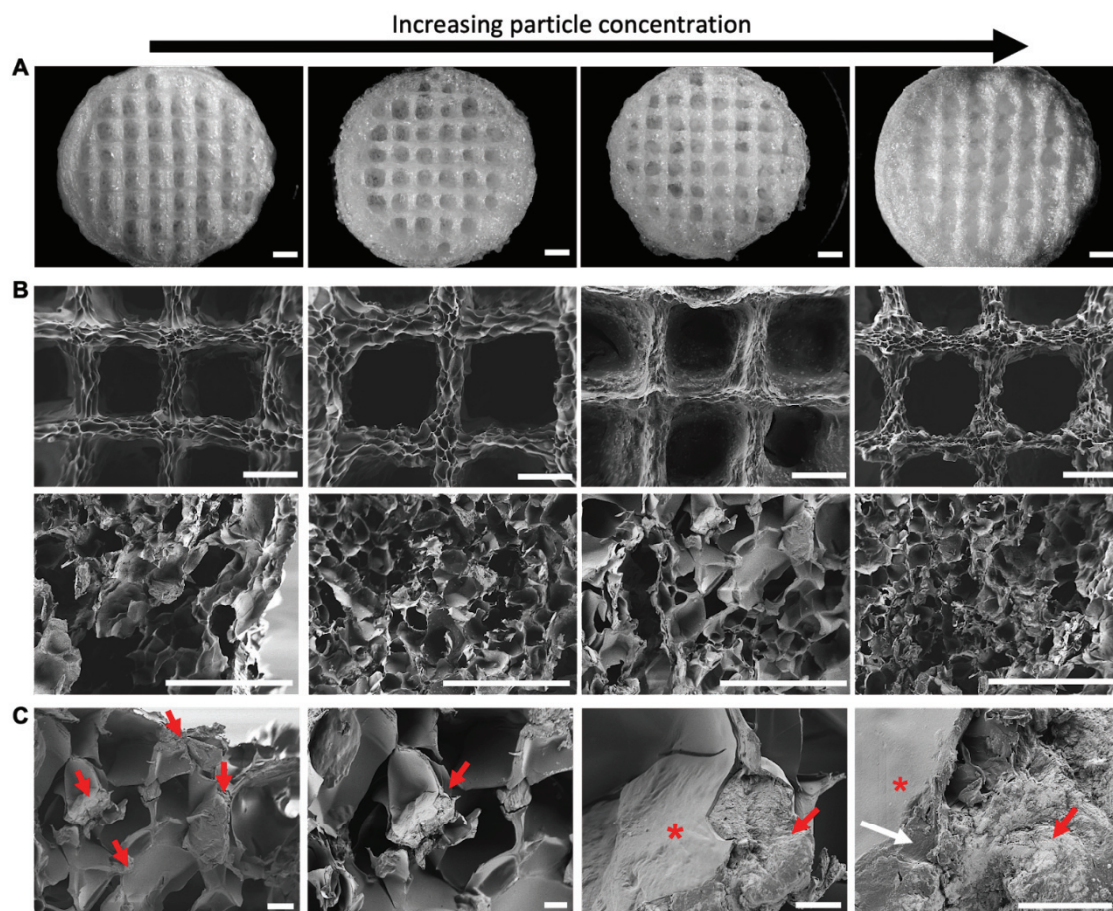
Figure 4.4. 3D-printed GEL, GEL/1% DB, GEL/3% DB and GEL/5% DB scaffolds after freeze-drying. Scaffolds display an increasing DB concentration from left to right. (A) Light microscopy images of the pristine GEL and D-incorporated GEL composite scaffolds. Scale bars: 1000 μm. (B) SEM images of the scaffolds show the surface morphology of the scaffolds in the top view (1st row) and pore structure in the cross-sectional area (2nd row) of the scaffolds. Scale bars: 500 μm. (C) GEL and DB particles interaction and DB particle bonding in GEL/1%DB scaffolds. Asterisk, red arrows and white arrows indicate polymer, particles and the GEL-particle interaction, respectively. Scale bars: 50 μm (first), 20 μm (second), 10 μm (third and fourth)[150].

The distribution of the DB particles and the pore morphology of the scaffolds were demonstrated by the µCT analysis (Figure 4.5). µCT analysis verified the generation of open-porous structures within the polymer network. DB particles are seen as bright dots and homogeneous distribution of the DB particles throughout the entire scaffold volume (Figure 4.5 A, B and C). Number of the particles within each DB particles containing GEL scaffolds was measured by µCT analysis (Figure 4.6. A). A homogenous, Gaussian particle size distribution was shown by the 3D analysis (Figure 4.6. B). Only a small number of bigger particles or agglomerates were seen. In GEL scaffolds containing DB particles, it was detected that nearly all of each group's particles range in size from 50 to 100 µm (Figure 4.6 C).
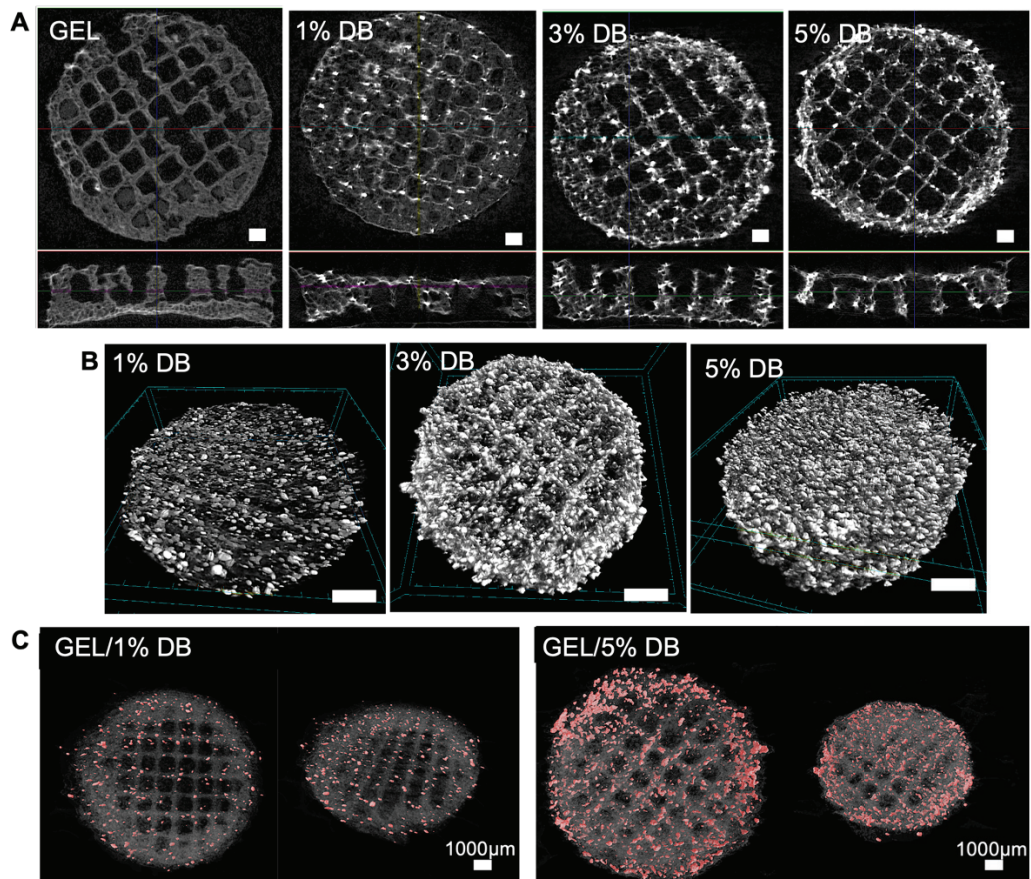
Figure 4.5. µCT analysis results of GEL and GEL/DB hydrgels. (A) Pore morphology and DB particle distribution inside the GEL matrix obtained by visual analysis of cross-sectional area (Scale bars: 1000 µm) and (B) volume rendering images. Scale bars: 500 µm. (C) Surface render analysis of DB particles (red) in composite hydrogels. Scale bars:1000 µm[150].
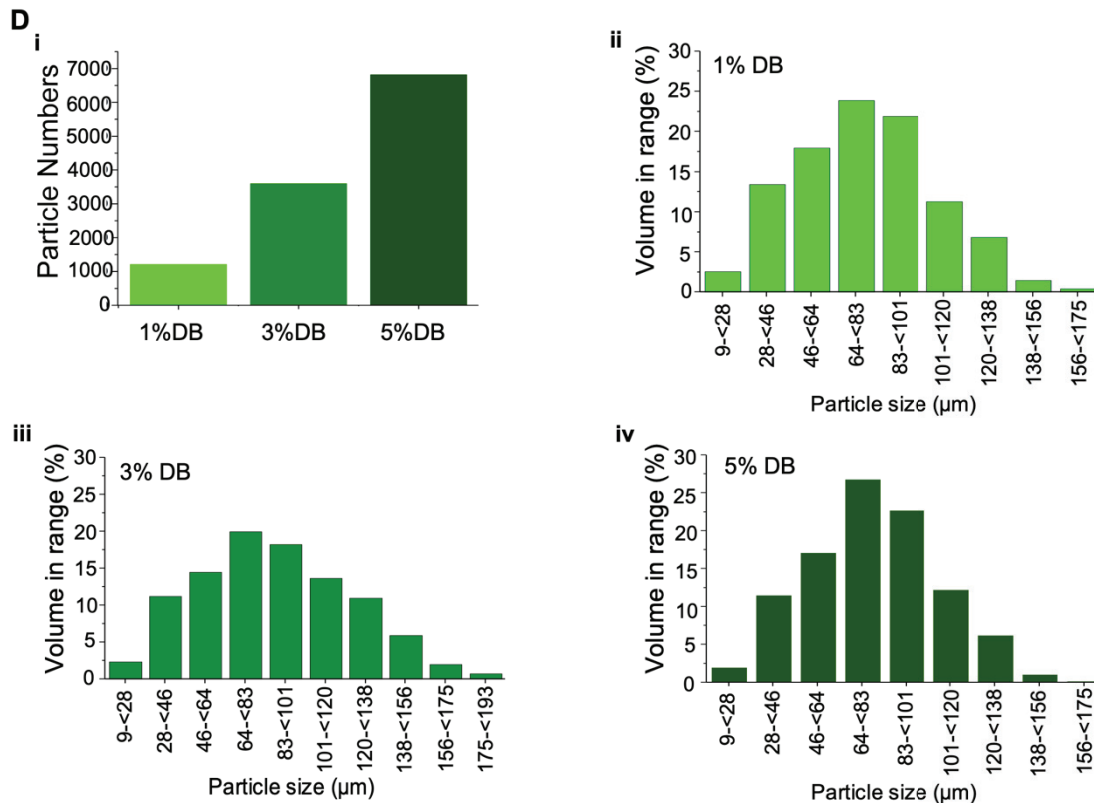
Figure 4.6. μCT analysis results of GEL and GEL/DB hydrgels. (A) Particle distribution within the composite scaffolds. (i) Particle numbers in the GEL/1%DB, GEL/3%DB, and GEL/5%DB scaffolds. Volume in range (%) analysis for (B) GEL/1%DB, (C) GEL/3%DB, and (D) GEL/5%DB scaffolds[150].

4.2.1.3. Mechanical Properties of the 3D-Printed Scaffolds

The mechanical properties of GEL and GEL/DB hydrogels were investigated by stress-relaxation tests to determine the effect of DB particles on the mechanical properties of the scaffolds. Figure 4.7 A displays the light microscopy images of the pure GEL and GEL/DB composite hydrogel discs. The compressive stress of hydrogels over time is shown in Figure 4.7 B. Hydrogels containing DB particles exhibited viscoelastic behaviour and stress relaxation due to the potential matrix reorganisation during test period. The stress-relaxation time was defined as the period during which 75% of the initial stress (upon 15% initial displacement) dissipated in the hydrogels (Figure 4.7 C). According to the test results, GEL/1%DB exhibited quicker relaxation than the other groups, whereas GEL/5%DB exhibited the slowest relaxation time. Apart

from a statistical difference between 1% and 5% of the DB-containing hydrogels, all groups exhibited a similar stress–relaxation time. The influence of hydroxyapatite crystals on the mechanical characteristics of the gelatin matrix was shown by Sartuqui et al. to exhibit interconnected micro- and macro-porosity[158]. Particles disrupt the hydrodynamic environment of the polymer and have the potential to control hydrogel relaxation by affecting the mechanical characteristics that support the influence of DB on hydrogel relaxation[158]. Young's modulus of the hydrogels was determined by calculating as a slope of the linear elastic deformation region in the stress–strain curve between 5% and 10% deformation. GEL/5%DB hydrogels exhibited the highest Young's modulus (29 ± 3 kPa), which was statistically significantly higher than the GEL hydrogels (24 ± 3 kPa). Young's modulus of 1%DB and 3%DB containing hydrogels was calculated as 27 ± 3 kPa and 28 ± 2kPa, respectively (Figure 4.7 D).
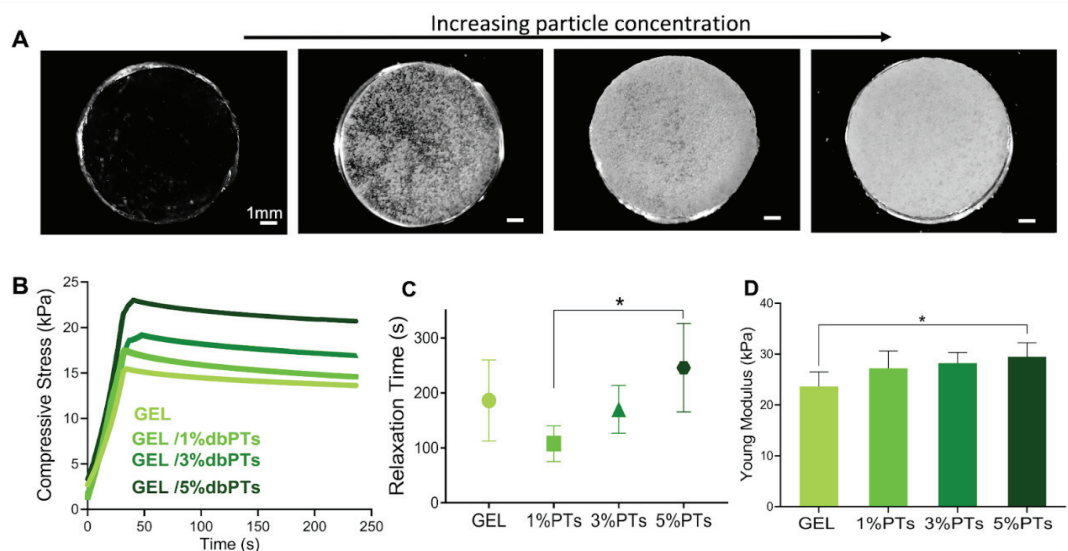
Figure 4.7. Mechanical characterization of the GEL and GEL/DB hydrogels: (A) light microscopy images of the GEL, GEL/1%DB, GEL/3%DB and GEL/5%DB hydrogels prepared for the mechanical tests (from left to right, scale bars: 1 mm), (B) compressive stress and (C) stress–relaxation time, described as the time after which 75% of the initial stress (upon 15% initial displacement) dissipated and (D) Young's modulus of the hydrogels. The tests were carried out using six replicates (n=6, mean ± SD). *p<0.05 indicates statistically significant differences of means compared to 3D-printed GEL and GEL/5%DB hydrogels by a one-way ANOVA test[150].

Mechanical tests indicate that the addition of DB particles improved the Young`s modulus of the pristine GEL. The proper particle–polymer interaction, as shown in the SEM images, allowed a decent load transfer between the GEL and particles as two different biomaterials according to the composite theory[159,160]. Therefore, this strong interface bonding enhanced the mechanical properties of the GEL/DB composite hydrogels. Since DB comprise fibrous collagen and hydroxyapatite crystals, DB particles appear to ensure optimum bonding to the GEL polymer matrix.

4.2.1.4. Physicochemical Properties of the 3D-Printed Scaffolds

The swelling/degradation behaviour of the GEL and GEL/DB composite scaffolds were assessed by measuring the weight changes. Scaffolds were observed during 49 days of incubation, and light microscopy images were displayed in Figure 4.8 A. All samples were swollen for two days, and higher weight gain was detected on day one for GEL/5DB scaffolds, with a total weight gain of approximately 70%. Scaffolds containing 1%DB and 3%DB demonstrated similar swelling behaviour, with a 60% total weight gain, and pure GEL scaffolds showed lower swelling, with a 30% total weight gain (Figure 4.8 B). After freeze-drying, both micropores and macropores were formed on the surface, as shown in the SEM images (Figure 4.4). Thus, surface area was enlarged, which facilitated the culture media absorption and promoted the scaffolds' swelling behaviour.

It has been shown that the liquids first fill the macropores of the scaffolds before filling the micropores, which then become immobilised[161]. Most of the adsorbed liquid remains mainly free in the polymer network due to the extensive interconnected pore structure in GEL hydrogels. The interconnected pores allow strong permeability and quickly absorb liquids from the environment[162]. The swelling of the pure GEL scaffolds was influenced by particle reinforcement in addition to the microporous and interconnective pore structure. The GEL/5% DB group with a greater particle concentration showed a more robust swelling capability (Figure 4.8 B). In addition, the fibrous collagen structure present in the DB might influence the swelling capacity, as shown previously[163,164]. The effect of particle content and micro- and macropore structure offers a benefit and improves the swelling capacity of the pure GEL scaffolds. After reaching the maximum swelling point, the DB-incorporated composite

scaffolds started to lose mass. Degradation started after 7 days, proceeding with mainly constant degradation trend, then between 14 and 42 days, a 40% mass loss was observed (Figure 4.8 C). The main limitation of the GEL is that the degradation rate is relatively fast for tissue engineering applications. To overcome this limitation, we used a higher concentration of crosslink; 10% mTG (w/v). Therefore scaffolds remained stable throughout the long period of degradation. In addition, GEL degradation could be tailored by the concentration of mTG. It was also reported that higher concentration of mTG led to a stable structure with a decreased degradation rate[165]. Figure 4.7 B depicts the degradation (erosion) of the scaffolds after 42 days (Figure 4.8 D). Additionally, the degradation rates of scaffolds were assessed and the highest rate was detected in 5%DB scaffolds with statistical differences in comparison to the pure GEL scaffolds (***$p<0.001$). In addition, the 1%DB and 3%DB incorporated groups showed similar degradation behaviour, with statistical differences (*$p<0.05$) compared to pure GEL scaffolds.

The chemical composition of the GEL/DB composite scaffolds was assessed by FTIR analysis. Figure 4.8 E depicts the FTIR absorbance spectra of the scaffolds made of DB, GEL, GEL/1%DB, GEL/3%DB and GEL/5%DB. The absorbance peaks of DB particles showed the main characteristic bands of collagen, defined to the C=O peptide group of amide I, the N–H bending vibration and the C–N stretching vibration of amide II, and the C–C stretching vibrations of collagen III, which were recorded at 1635 cm^{-1}, 1540 cm^{-1} and 1240 cm^{-1}, respectively[166]. The P–O stretching band was responsible for the broadest absorption band, recorded at about 1015 cm^{-1}. Additionally, the O–P–O bending mode of hydroxyapatite is attributed to P–O bending, recorded at 650 and 570 cm^{-1}. The primary characteristic peaks of gelatin were also detected as amide I, II and III, with the broadband at around 3350 cm^{-1} and 3082 cm^{-1}.[151]
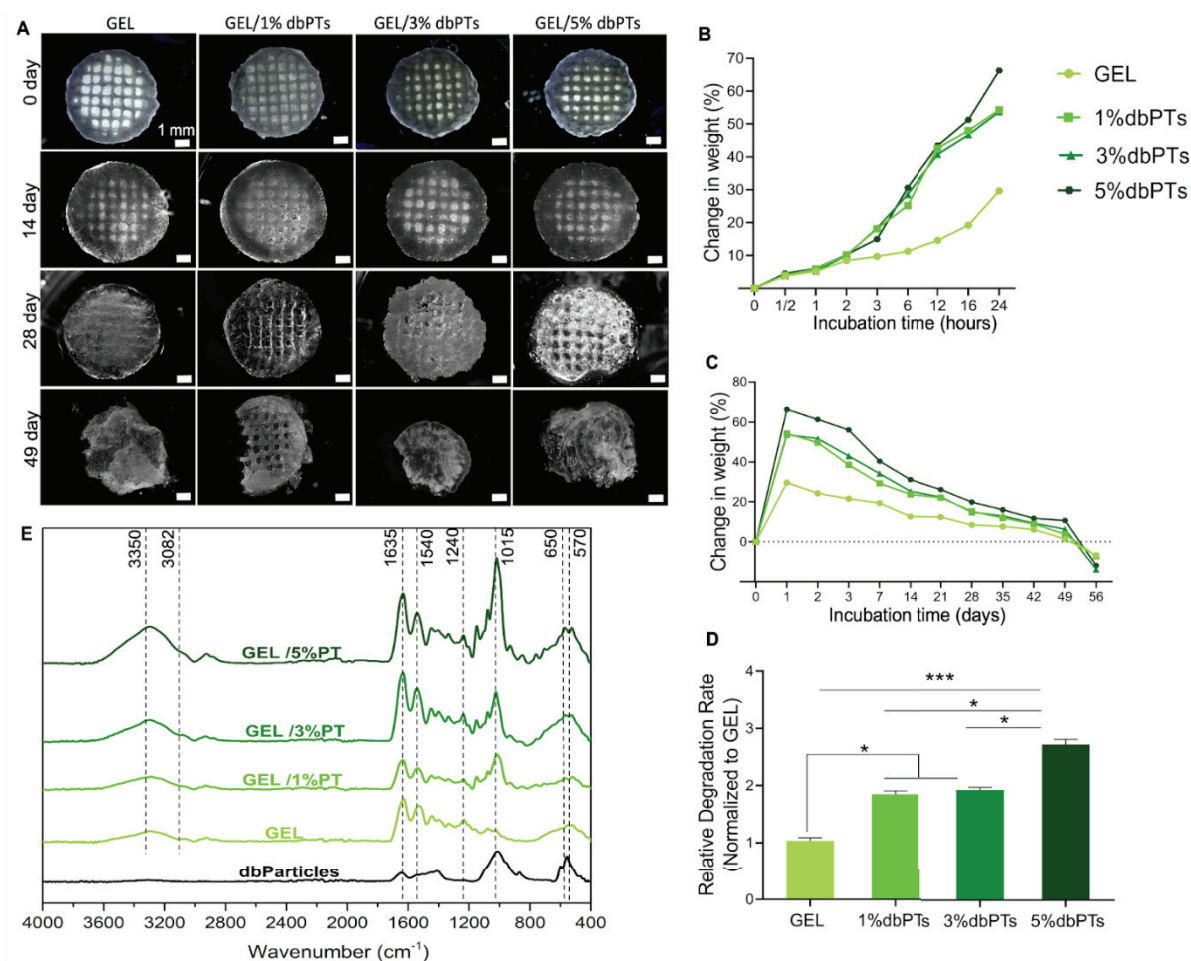
Figure 4.8. Physicochemical characterizations of the 3D-printed GEL and GEL/DB composite scaffolds. (A) Light microscopy images of the scaffolds on 0, 14, 28 and 49 days to assess the degradation/swelling behaviour. Scale bars: 1mm. (B) Weight changes of the scaffolds after 24 h and (C) 56 days (n=6, mean ± SD). (D) Quantification of the degradation rate by a linear slope of the weight changes between 24 h and 21 days with statistically significant differences (*p<0.05 and ***p<0.001). (E) FTIR spectrum of the DB, GEL and GEL/DB composite scaffolds (n=3)[150].

4.2.1.5. *In vitro* Cytocompatibility Assessment

MC3T3-E1 cells were used for *in vitro* cell culture experiments to evaluate the cytocompatibility of GEL/DB scaffolds (Figure 4.9 A). For the cell culture study, 1%DB and 3%DB incorporated GEL scaffolds were utilized owing to their higher printability capability and reproducibility. Tissue culture polystyrene (TCP) and pure GEL scaffolds served as the control groups. The results show that cells grew and proliferated on each scaffold group. LDH release experiments were carried out to determine the potential cytotoxicity of the composite scaffolds and findings revealed similar LDH releasing for each group without statistically significant differences between time periods and groups, indicating no cytotoxicity on cells (Figure 4.9 B).

Cytotoxicity of the GEL and GEL/DB scaffolds were evaluated after cell seeding as illustrated in Figure 4.9 A. The LDH releasing measurement showed that LDH levels releasing by cell stable during 28 day culture period which indicate higher viable cell density (Figure 4.9 B). Additionally, WST-8 data demonstrated that the metabolic activity of cells seeded on composite scaffolds was increased during the 21-day incubation (Figure 4.9 C). The highest viability level was detected on day 21 for all groups and statistically significant differences were found compared to TCP (**$p < 0.01$). In particular, the 1% DB particle incorporated group showed higher viability on day 21, with statistically significant differences compared to the other groups (***$p < 0.001$). Live/Dead staining results showed cell viability on the GEL and GEL/DB groups (Figure 4.9 D). The cells spread and proliferated in all groups after 14 days. It was hard to detect dead cells even after 14 days; therefore, fluorescence images only represent live cells as a green fluorescence. Cell viability was high and no dead cells were found during the cell culture period, indicating that 3D-printed DB composite scaffolds are cytocompatible and suitable for cell growth (Figure 4.9 D). The cytotoxicity assessments revealed that pristine GEL and GEL/DB composite scaffolds have a favourable environment for MC3T3-E1 pre-osteoblasts and exhibit promising properties for cell viability. Similar to our results, the biocompatibility of GEL scaffolds with various cell types has been reported in numerous studies[167,168]. Besides the cytocompatibility of GEL, cell viability was improved significantly by the incorporation of DB particles, which might be led by the collagen hydroxyapatite content of the particles[169].
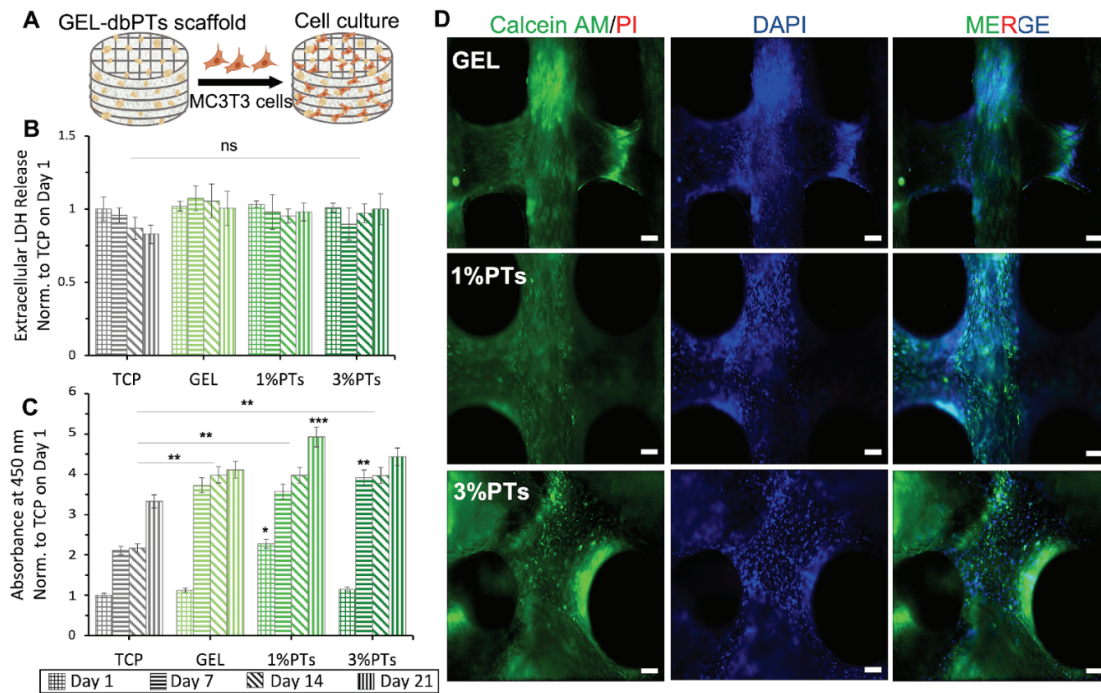
Figure 4.9. *In vitro* cytocompatibility results of the 3D-printed composite scaffolds. (A) Schematic illustration of the cell culture with MC3T3-E1 pre-osteoblasts. (B) Quantifying the extracellular LDH release for 21 days with no statistical significant differences (ns) between groups and time points (n=6). (C) WST-8 assay of MC3T3-E1 cells on the GEL/DB scaffolds (n=6), normalised to TCP control on the first day of incubation. All data are represented as mean ± SD. *p<0.05, **p < 0.01, ***p<0.001 indicate statistically significant difference of means. (D) Fluorescence microscopy images of MC3T3 cells on the scaffolds cultured for 14 days. Calcein AM (green), PI (red), and DAPI (blue) staining represent live and dead cells and cell nuclei, respectively. (Scale bars: 100 μm) [150].

SEM analysis was performed to assess the cell growth and attachment on the pristine GEL and GEL/DB composite scaffolds. Images displayed spindle-shaped, elongated pre-osteoblasts on the surface of the scaffolds and cells covering the entire surface (Figure 4.10 A). Cells spread on the surface until confluency, with a favourable cell-material interaction. Figure 4.10 B demonstrates that pre-osteoblasts not only spread on the surface but also migrated into the interconnected pores and covered the pore walls during 14 days of cell culture (Figure 4.10 B). Moreover, a dense cell layer with a multi-layered ECM production was observed on the composite scaffolds (Figure

61

4.10 C). Cell proliferation was determined by PicoGreen assay and total dsDNA content was quantified. The results indicated that cell proliferation gradually increased on the composite scaffolds during the cell culture period (Figure 4.10 D). The cells grown on the 1% and 3% DB containing scaffolds showed higher proliferation than those grown on the TCP and GEL groups at each time point. There were statistically significant differences for 21 days (**p<0.0.1) as well as 28 days (***p<0.0.1) compared to the other groups. The RGD sequence of GEL and cytocompatible DB particles improved cell attachment and proliferation. The particle incorporation, notably the homogeneous distribution of DB particles within the GEL matrix, as displayed previously in the μCT images (Figure 4.5), could be associated with increased cell proliferation.
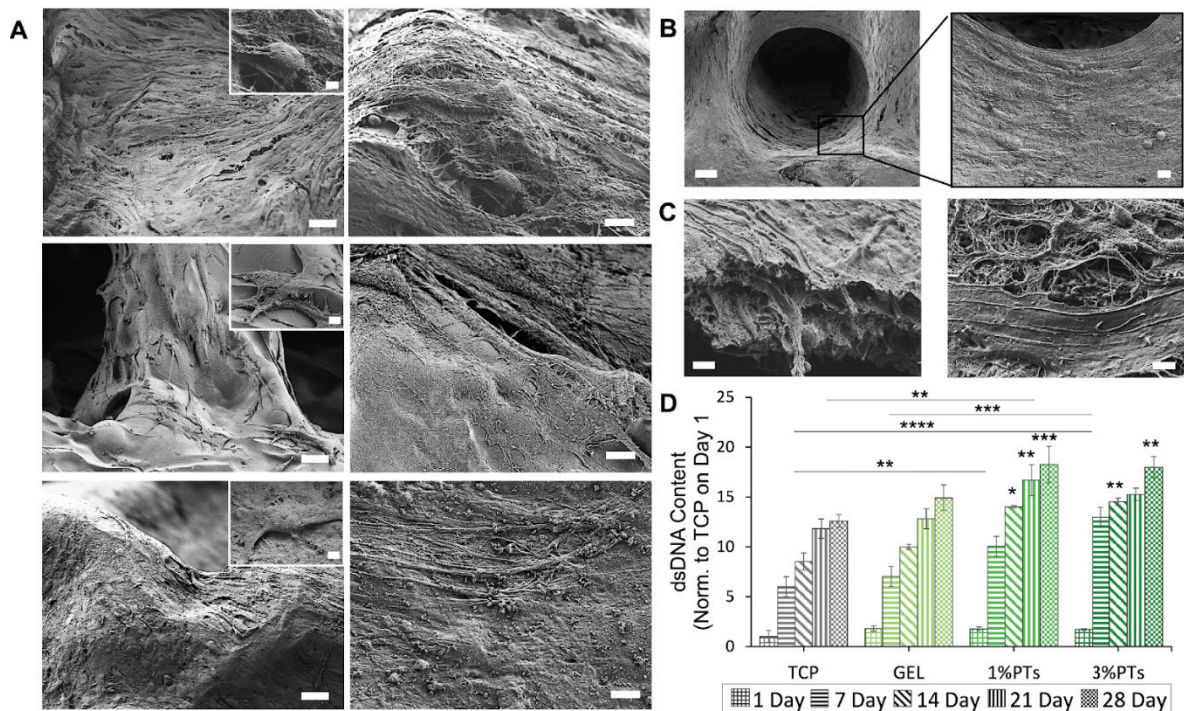
Figure 4.10. Cell growth and proliferation on the 3D-printed scaffolds. (A) SEM images of MC3T3-E1 cells on 14 days of culture on GEL, GEL/1%DB, and GEL/3%DB scaffolds (from top to bottom). Scale bars: 20 μm (left images), 5μm (right images), 2μm (insets). (B) SEM images of the cells covering the pore structure in circular patterns. Scale bar: 100 μm (left), 10 μm (right). (C) SEM images of dense cell layers on the surface of scaffolds with a multi-layered ECM production after 14 days. Scale bar: 1 μm. (D) PicoGreen proliferation assay result of cells on the GEL and GEL/DB

scaffolds (n=6), normalised to TCP control on the first day of cell culture. Data are shown as mean ± SD and *, **, ***, and **** indicate p<0.05, p<0.01, p<0.001, and p<0.0001 statistically significant data by one-way ANOVA analyses[150].

Figure 4.11 displays the SEM analysis and multiphoton imaging demonstrating cell-material and cell-particle interactions over 14 days. MC3T3-E1 pre-osteoblasts covered the scaffolds' surface and spread on the DB particles while exhibiting effective interaction (Figure 4.11 A). When combine with SEM analysis, similar cell adhesion was observed by multiphoton microscopy (Figure 4.11 B). DAPI staining (cyan) and F-actin (red) staining indicated the nucleus and cytoskeleton of the cells, respectively. DB particles showed a bright (as shown in blue) second harmonic generation signal (SHG) due to the autofluorescence property of fibrous collagen presence in DB (Figures 4.11 B and C). MC3T3-E1 pre-osteoblasts attached and surrounded DB particles within the GEL matrix (Figures 4.11 D and E). Multiphoton microscopy images confirm that cells proliferated on the scaffolds and migrated through the pores while interacting with particles, which may result in due to the collagen fibers presence in DB that facilitate cell adhesion and cell–material interaction, or, enzymatically, mTG crosslinking could support the cell adhesion [140]. In addition, it is already known that the porous structure of the scaffold could be another beneficial factor the cell adhesion, since micropores formed after freeze-drying . Notably, during the degradation process, porosity may increase, leading to an increased surface area; thus, cells can spread over larger surfaces, and homogenous cell–material interaction can occur. As reported by Yung et al., when degradation starts, cells move through to the GEL matrix, which is tuneable by the mTG[140,170]. Thus cells can move through the scaffolds and migrate inner part of the scaffolds[140,170]. The cell culture study demonstrated favourable cell–particle and cell–matrix interactions in 3D-printed GEL/DB composite scaffolds and showed promising results for bone-tissue engineering applications. Preserving the natural hydroxyapatite and collagen composition of the DB particles by our decellularization method, enhanced the cell adhesion, proliferation and migration, as well as the mechanical and physicochemical properties.
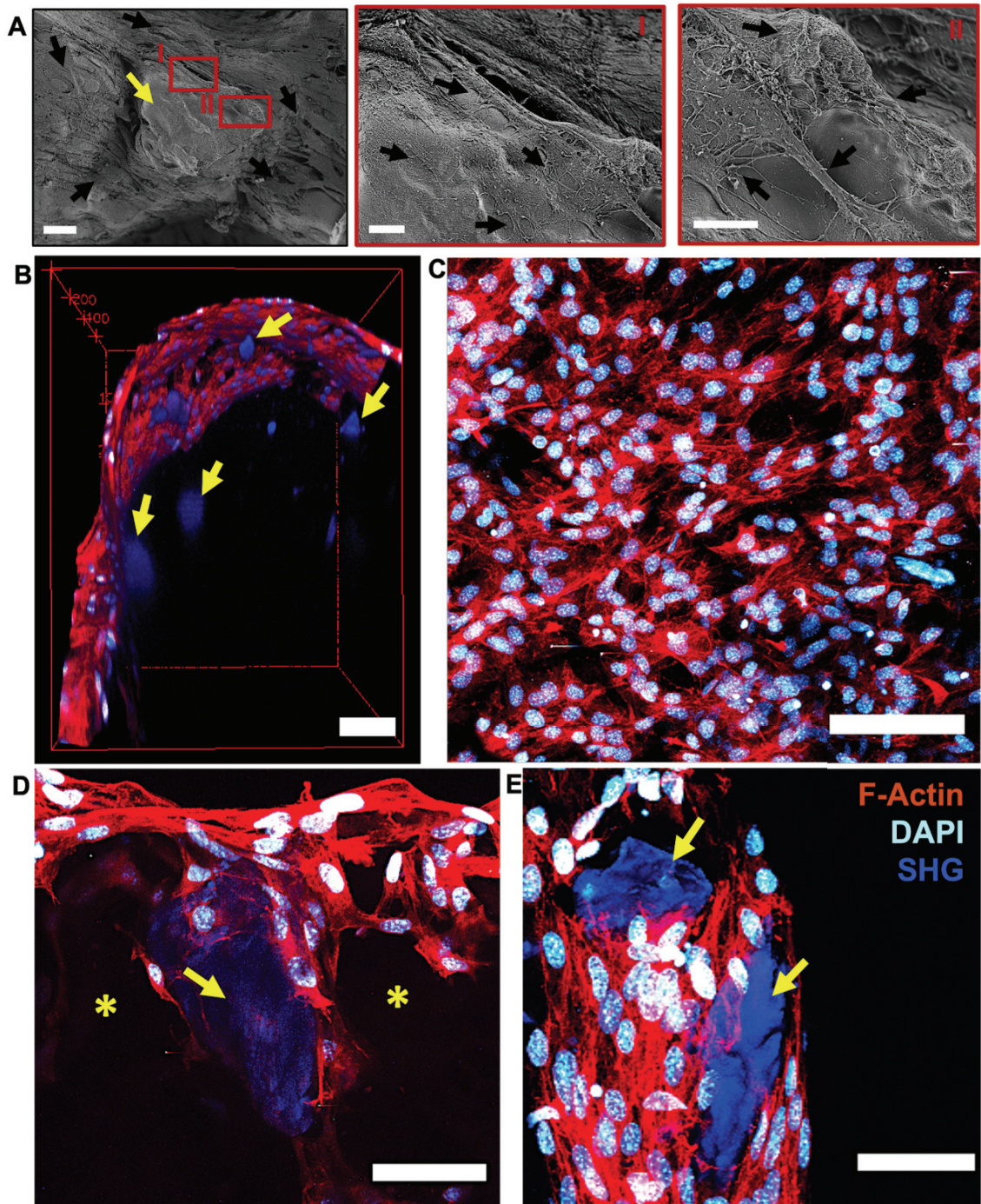
Figure 4.11. The interaction between cells (black arrows) and particles (yellow arrows) in the GEL/DB composite scaffolds for 14 days. (A) SEM analysis of MC3T3-E1 pre-osteoblasts interacted with DB particles on composite scaffolds. Scale bar: 20 μm (left), 5μm (right). (B-E) Multiphoton microscopy images, DAPI (cyan, nuclei), F-Actin (red, cytoskeleton), SHG (blue, DB particles). Maximum intensity projection. (B) 3D view of pre-osteoblasts growing on GEL/DB composite scaffolds. Scale bar: 100

μm (C) The surface of the scaffolds covered with a dense cell layer. Scale bar: 100 μm. (D) 3D view of cells growing on pore structures and around DB particles (yellow stars indicated particles in blue colour). Scale bar: 50 μm. (E) Cell-particle interaction and complete cell coverage around the particle. Scale bar: 50 μm[150].

Similar to our approach, DB-ECM mixed with poly-ε-caprolactone (PCL) was compared with nonbiological hydroxyapatite additive materials, which are frequently used in bone tissue engineering in terms of cell proliferation and osteogenicity. The results showed that DB-ECM materials increased the proliferation and expression of the osteogenic markers for adipocyte-derived stem cells[147]. Numerous studies reported the fabrication of the scaffold containing hydroxyapatite-like inorganic additives or collagen as a supportive biological derived polymer in bone tissue engineering[171–174]. In addition to the promising findings of previous studies, DB provide a natural source of natural collagen fibers and hydroxyapatite crystals. Fabricated DB-particle-incorporated GEL scaffolds demonstrated the proper features for bone-tissue engineering and exhibited favourable cell–material and cell–particle interactions. The addition of DB particles to the GEL matrix increased cell attachment and proliferation, and cells migrated into the pores, interacting with particles. This enhancement in cell behaviour was assumed due to the collagen fibers and hydroxyapatite components present in the decellularized bone. As hypotheses, the remaining natural bone histoarchitecture by our decellularization method promoted cell behaviour within the GEL matrix, and DB incorporated biomaterial inks exhibited promising features for 3D-printing applications. With the successful fabrication of the GEL/DB biomaterial inks and the promising cell response, it was considered that including a smaller size of bone particles within the GEL matrix could enhance printability, allowing for a higher concentrations of DB particles. Therefore, smaller sizes (45 μm) of bone particles were prepared and mixed with GEL, then mechanical and rheological characterization as well as *in vitro* biological activity of cells were investigated for further studies.

4.2.2. Bovine DB Particle Incorporated GEL Bioinks

4.2.2.1. Rheological Assessments

The rheological characterization of the GEL and DB incorporated GEL biomaterial inks was assessed (Figure 4.12). Shear rate sweep tests were performed for each group by measuring the viscosity by increasing the shear rate from 0 to 300 s^{-1} (with a shear rate increment of 0.1 s^{-1} per second). The test results revealed that the viscosity of the DB-particle-incorporated-GEL and pure GEL materials decreased while the shear rate is increased, which indicates that all materials exhibited shear-thinning behaviour, as described previously[175]. In addition, with the addition of DB particles, the viscosity increased (Figure 4.12 A). At a shear rate of 1/s, the viscosity of GEL and GEL/5DB (100 μm) were similar and determined as ~130 and ~150 Pa.s, respectively. The viscosity of the smaller (45 μm) DB-particle-incorporated GEL was increased, however; notably, 10% concentration of DB particles was determined as the highest viscosity. The viscosity of GEL/5DB (45 μm) and GEL/10%DB (45 μm) materials were found as ~180 and ~300 Pa.s, respectively, at a shear rate of 1/s (Figure 4.12 B). In the 3-interval thixotropy test, GEL and DB incorporated GEL showed self-recoverable properties, indicating that biomaterial inks can maintain their shapes after 3D printing (Figure 4.12 C). The concentration of DB particles in GEL influenced the self-recovery property of composite biomaterial inks. The recovery of pure GEL was the lowest compared to the DB-incorporated GEL biomaterial inks. The most prominent recovery of the viscoelastic property was determined for the GEL/10% DB material group. The rheological tests demonstrated that DB particles incorporated-GEL and pure GEL materials exhibit a shear-thinning behaviour and self-recoverability which indicates that prepared biomaterial inks are printable. The prepared GEL/DB composite biomaterial inks demonstrate promising rheological properties for potential application for 3D printing.
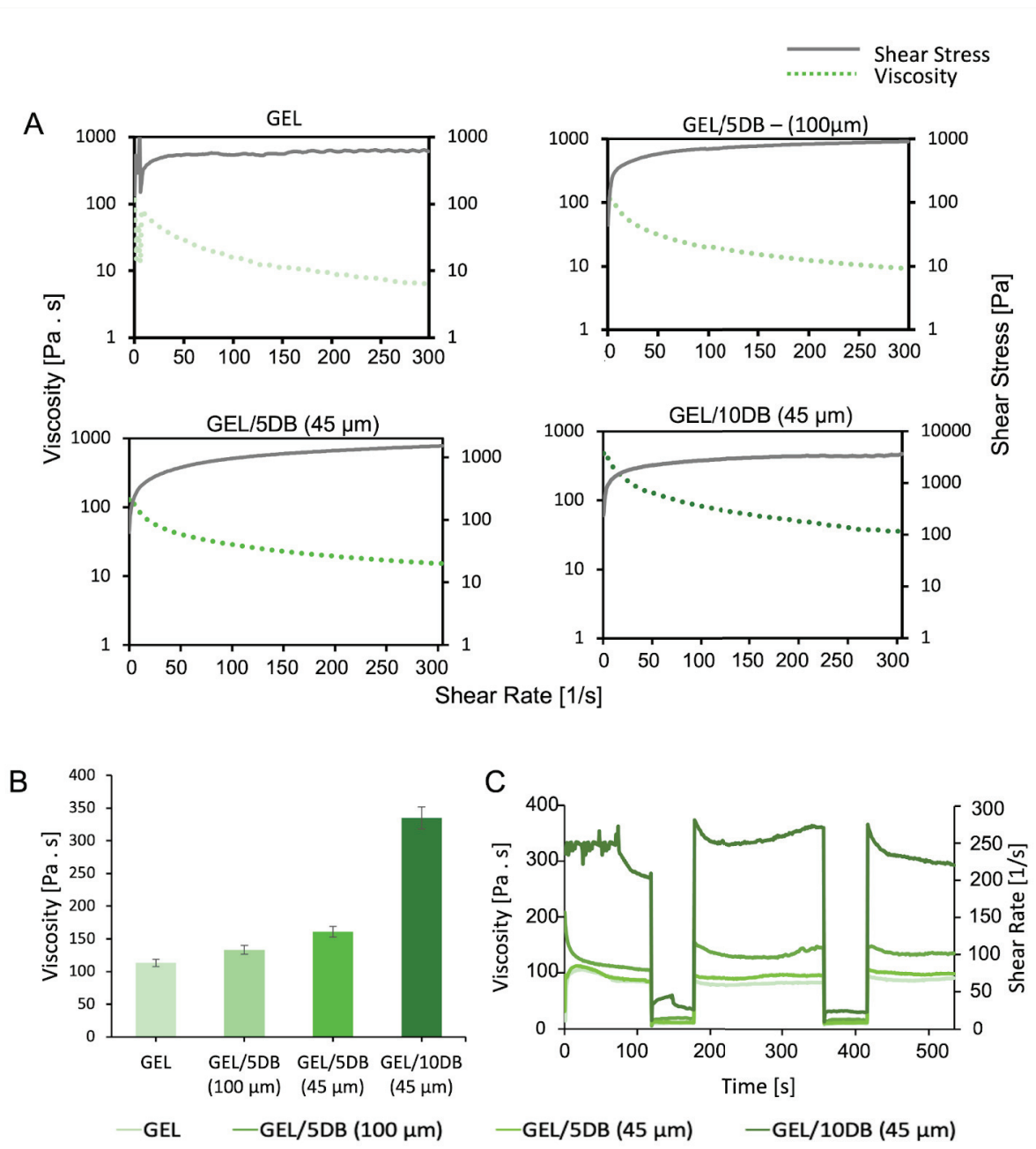
Figure 4.12. Rheological test results of the GEL/DB biomaterial inks. (A) The shear rate sweep test results show viscosity when the shear rate increases. (B) Viscosity of the GEL and GEL/DB groups at a shear rate of 10/s. (C) The 3-interval thixotropy test indicates the shape recovery during printing.

4.2.2.2. Fabrication of 3D-Printed GEL/DB Composite Scaffolds

GEL/DB composite scaffolds containing 5% and 10% DB particles (wt%) were 3D printed in cylindrical shapes and 0° /90° strand patterns.(Figure 4.13 A). The composite scaffolds were easily fabricated in all groups. The printing of 10% DB particle-incorporated GEL material, however, was not possible in the 100 μm DB particle-incorporated group due to the clogging of the nozzle. Therefore, an attempt was made to use a smaller particle size (45 μm) to evaluate the influence of more DB particle incorporation into the GEL matrix. Light microscopy images demonstrated the well-shaped 3D-printed structures, resulting in ideal, square-shaped macropores. (Figure 4.13 A). In addition, DB particles are seen in the 3D-printed structures as a white colour phase in the microscopy images. In addition, increasing turbidity was detected when particle amount increased in structures (Figure 4.13 A). As seen in the GEL/10DB group, scaffolds showed a white colour in comparison to the other groups, which indicates higher amount of DB particles (Figure 4.13 A). Furthermore, incorporation of the smaller size of the DB particles increased the turbidity of the scaffolds when compared to the 100 μm DB particle-incorporated GEL scaffolds.

The printability accuracy of the bovine-bone-particle-incorporated hydrogels was determined with the assessments of the Pr and U factors based on the strand homogeneity and pore circularity of 3D-printed structures. The quantification of Pr showed that all groups have a similar printability capacity (Pr ~1) to produce square pores. The pure GEL hydrogels and the hydrogels containing 5% and 10% DB of 45 μm size showed similar Pr factors (Pr ~1) (Figure 4.13 B). The Pr factor of hydrogels with 5% DB of 100 μm size, however, showed only a slight decrease and a tendency for strand fusion (Pr=0.88) (Figure 4.13 B). Both rabbit and bovine bone particles at the 5% concentration demonstrated a similar printability capacity (Figure 4.3 B and 4.13 B). In addition, as intended, reducing the particle size increased printability and allowed the use of higher concentration of particles (10% DB particles).
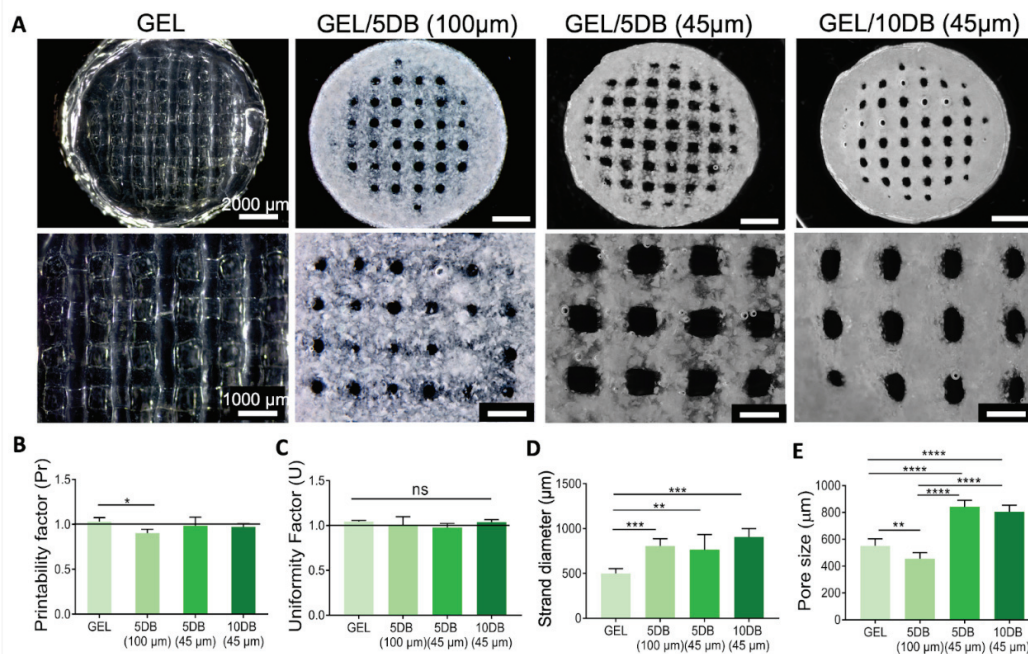
Figure 4.13. 3D-printed bovine DB particles incorporated-GEL hydrogels. (A) Light microscopy images of 3D-printed composite hydrogels. Scale bars: 2000 μm (top), 1000 μm (bottom). Printability assessments of hydrogels based on the measurement of (B) Pr and (C) U factors, (D) strand diameter and (E) pore size. Data are shown as mean ± SD. *p<0.05, **p<0.01, ***p<0.001 and ****p<0.0001 indicate statistically significant differences compared to 3D-printed structures by one-way ANOVA tests.

The measurements of the U factor demonstrated that the U factors of the 3D-printed hydrogels were very close to 1, and all hydrogels had a similar U factor without statistically significant differences (Figure 4.13. C). Moreover, the strand diameter of 3D-printed scaffolds increased as the DB particle concentration increased. The pure GEL hydrogels showed the lowest strand diameter: 505 ± 23 μm. The strut diameters of hydrogels containing 5% DB (100 μm), 5% DB (45 μm) and 10% DB (45 μm) were measured as 806 ± 22 μm, 765 ± 51 μm and 907 ± 33 μm, respectively (Figure 4.13 D). Statistically significant differences were found in the DB-incorporated groups compared to the pure GEL hydrogels. The pore sizes of the 3D-printed GEL, GEL/5% DB (100 μm), GEL/5% DB (45 μm) and GEL/10% DB (45 μm) were determined as 596 μm, 456 μm, 815 μm and 765 μm, respectively. There are statistically significant differences between GEL and GEL/5%DB (100 μm) groups, in addition, when compare

GEL/5%DB (100 µm) groups with GEL/5%DB (45µm) and GEL/10%DB (45 µm) groups (Figure 4.13 E). The measurements indicate that pore sizes in all groups are proper for cell attachment, migration and proliferation in bone tissue engineering applications[153]. Considering all measurements, 3D-printed composite hydrogels exhibited printability capacity with the formation of the 3D layer-by-layer structures, indicating promising bioink formulations for bone tissue engineering applications.

4.2.2.3. Mechanical Properties of 3D-Printed GEL/DB Scaffolds

The mechanical properties of the GEL and GEL/DB hydrogels were investigated with compression tests. Mechanical tests revealed the effect of the DB particle incorporation into the GEL matrix. Young`s modulus and the maximum force borne by the hydrogels until failure increased with the incorporation of the particles, as seen in Figure 4.14 A. The Young`s modulus of the pure GEL group measured the lowest, at 15.89 ± 2 kPa, and statistically significant differences were found in comparison to the other groups (****$p<0.0001$). The Young`s modulus of each of the 5% DB-containing groups in both the 100 µm and 45 µm sizes was similar and determined as 26.79 ± 2 kPa and 29.56 ± 3 kPa, respectively, without any significant differences (Figure 4.14 A). 10% DB-containing GEL composite hydrogels demonstrated the highest Young's modulus (46.61 ± 2 kPa), with statistical differences compared to the other groups (Figure 4.14 A). Additionally, the maximum borne by the hydrogels during tests were determined. Similar to the Young`s modulus determination, the maximum force borne by the hydrogels increased as the incorporation of the particle concentration increased (Figure 4.14 B). The maximum forces were determined as 14.87 ± 2 kPa, 25.14 ± 3 kPa, 32.53 ± 2 kPa and 52.52 ± 4 for the GEL, GEL/5% DB (100 µm), GEL/5% DB (45 µm) and GEL/10% DB (45 µm) groups, respectively. Statistically significant differences were found among all groups (Figure 4.14 B). The compression test results demonstrate the influence of the particles on the mechanical properties of hydrogels, indicating that particle incorporation into the GEL matrix improves its mechanical properties. The incorporation of the decellularized rabbit bone particles increased Young`s modulus slightly, with no statistical differences except in the 5% particle concentration group, as shown in Figure 4.6. Young`s modulus of GEL/5%DB rabbit and bovine (in 100 µm size) hydrogels were found as 29 ± 3 kPa and 26.79 ± 2 kPa, respectively. In 45 µm

particle size GEL/5%DB bovine bones group, Young`s modulus determined as 29.56 ± 3 kPa and there were no statistical differences between 100 μm particle size bovine and rabbit groups (Figure 4.14 A). The increasing DB particle concentrations (5% DB and 10% DB) increased the mechanical properties of the GEL hydrogels, however, particle size (100 μm and 45 μm) did not effected significantly. The addition of the inorganic reinforcement could increase the mechanical stiffness of the 3D structures, as shown previously[176]. Biscaia et al. developed hydroxyapatite reinforced PCL scaffolds with a 3D printing technique and compared the materials' compressive modulus among groups[176]. The highest compressive modulus was found in the higher hydroxyapatite containing group, resemblance with our results caused by the higher concentration of DB particles due to the higher content of hydroxyapatite[176]. One of the primary purposes of using a higher particle concentration is to improve mechanical properties, which is a requirement for 3D-printed hydrogels with low mechanical properties for bone-tissue engineering applications. Using DB particles at higher concentration could overcome this limitation, as demonstrated by the 10% DB-incorporated group. The proper particle–polymer interaction, as shown in the SEM images (Figure 4.4 C), allowed for a load transfer between particle and GEL, according to the composite theory. Therefore, the mechanical properties of the composite hydrogels were enhanced.
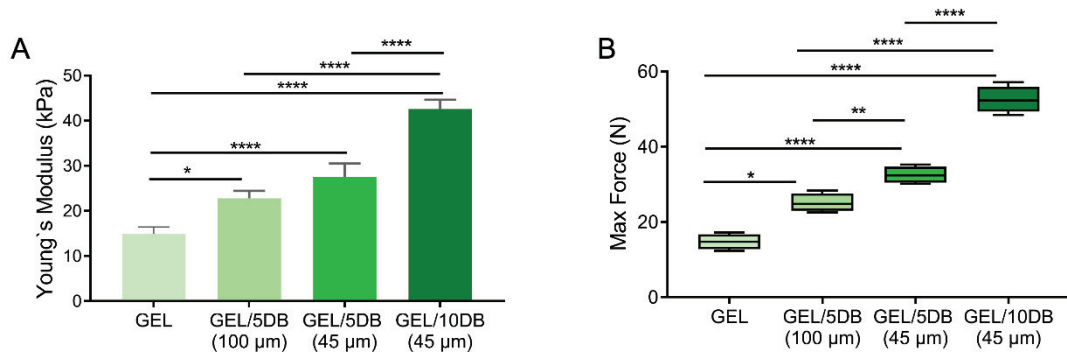
Figure 4.14. Mechanical characterization of the bovine DB particles incorporated-GEL composite hydrogels. (A) Young's modulus of the hydrogels and (B) Maximum force the samples could bear until failure. The compression tests were performed using six replicates (n=6). Data are shown as mean ± SD. *$p<0.05$, **$p<0.01$, ***$p<0.001$ and ****$p<0.0001$ indicate statistically significant differences compared to 3D-printed GEL and GEL/DB hydrogels by one-way ANOVA test.

4.2.2.4. Cytocompatibility and Cell Growth inside the 3D-Bioprinted Constructs

GEL/DB hydrogels prepared with two different sizes of DB particles (45 μm and 100 μm) were bioprinted using hTERT-MSCs in circular shapes with 5 layers and cultured for 28 days. The biological activity of cell-laden scaffolds was assessed in terms of cytotoxicity, biological activity and osteogenecity.

The cell viability inside the 3D-bioprinted structures was evaluated with a Live/Dead staining assay, and cell-laden scaffolds were observed by fluorescence microscopy. Live/Dead staining images revealed cell growth inside the GEL and GEL/DB scaffolds (Figure 4.15) during the 28 day culture period. After 7 days, cells were elongated and spread over the hydrogels with high cell viability. In fluorescence microscopy images, DB particles were observed as a blue colour due to the autofluorescence feature of the collagen. The spreading of hTERT-MSCs was favourable at each time point, and complete cell coverage was observed after 28 days of culture. Moreover, the density of live cells (green) was quite high on all incubation days. It is difficult to find dead cells (red) on day 28, indicating that DB-incorporated composite bioink formulations are cytocompatible and suitable for cell growth.

The potential extracellular cytotoxicity effects of the scaffolds were quantified using LDH cytotoxicity assay after bioprinting. Cell-laden scaffolds were cultured for 28 days, and LDH was measured from the cell culture supernatant at each time point. The results showed that the cytotoxicity level of the scaffolds was stable and not increased in any group during the 28 days of the culture period. No statistical differences were detected during the culture period, indicating that the prepared bioink formulations had no cytotoxic effect on hTERT-MSCs (Figure 4.16 A). As shown also in the rabbit-DB-particle-incorporated-GEL scaffolds, bovine DB particles have no cytotoxicity effects on hTERT-MSC either (Figure 4.9 B). It was found that different sizes and concentrations of DB particles have no influence on cytotoxicity and cell viability, as reported by Dong et al. in a comprehensive review regarding the size-dependent cytotoxicity of silica nanoparticles[177].
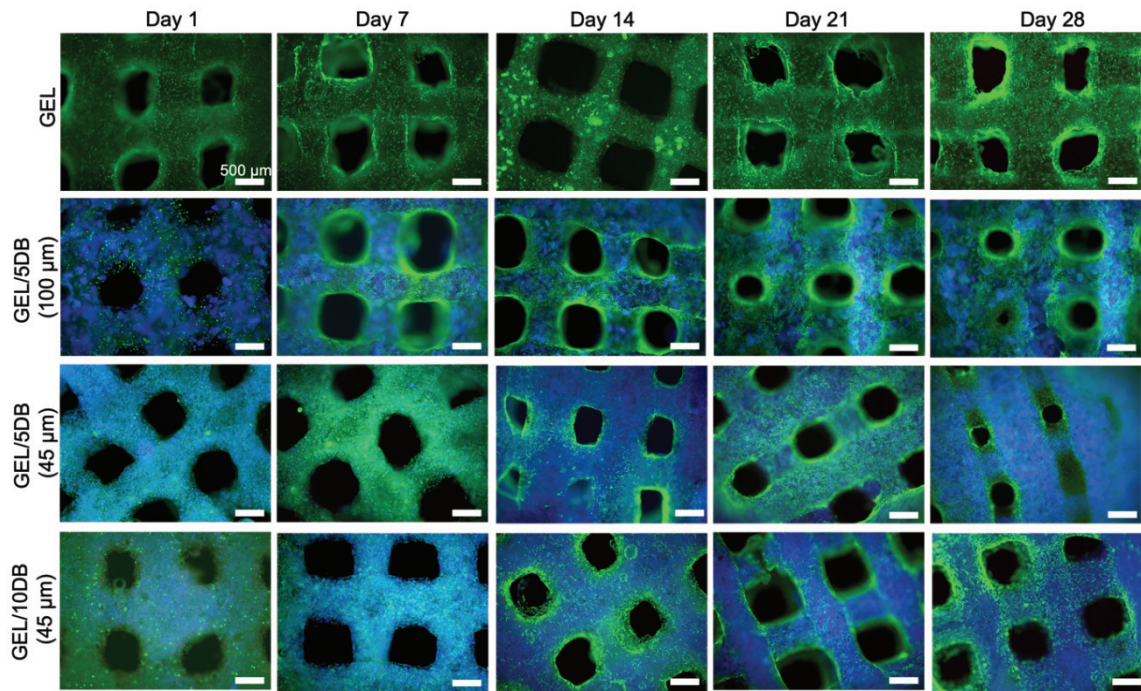
Figure 4.15. Live/Dead staining results of hTERT-MSC cells inside the bioprinted GELand GEL/DB composite scaffolds for 14 days of the cell culture. Calcein AM (green) and PI (red) staining represent live and dead cells, respectively. The blue color indicates the particle`s autofluorescence.

Cell proliferation was assessed by a PicoGreen assay based on the quantification of the dsDNA content of the cell-laden constructs. The dsDNA quantification results showed that hTERT-MSCs proliferated during the 28 days, with an increasing trend (Figure 4.16 B). The highest proliferation of hTERT-MSCs was detected for the GEL/10DB group in comparison between all groups at each time point of the culture. In addition, cell proliferation significantly increased inside the GEL/DB structures, and it was found that as DB particle concentration increased, the dsDNA number increased as well. Increasing cell proliferation might be directly associated with the DB particle addition as well as the homogeneous distribution of DB particles within the GEL matrix (Figure 4.5). Particle-cell interaction promote proliferation inside the GEL hydrogels. The particle incorporation significantly supported cell proliferation, which may be related to the collagen and hydroxyapatite composition of DB particles shown in the results of histological staining and biochemical analysis (*Chapter 3*, Figures 3.5, 3.6 and 3.7). In addition, numerous studies reported that 3D-bioprinted structures using several biopolymers with hydroxyapatite and the addition of hydroxyapatite significantly

supported the cell proliferation and osteogenicity in vivo[178,179]. According to our cytotoxicity and DNA assessment results, the DB-incorporated GEL composite hTERT-MSCs-laden scaffolds showed no toxic effects on cells and have a suitable environment for cell growth, with cytocompatibility.

The hTERT-MSCs inside the 3D-bioprinted GEL/DB scaffolds were cultured both with (+OS) and without (-OS) an osteogenic induction medium for 28 days to assess the differentiation capacity of the cells. Cell differentiation was determined by PicoGreen dsDNA and ALP activity assays for 28 days. The dsDNA assay results show that hTERT-MSCs proliferated gradually inside 3D-bioprinted scaffolds in both the +OS and -OS groups (Figures 4.16 B and D). The addition of the DB particles in both sizes enhanced the cell proliferation with and without osteogenic induction. Due to the collagen and hydroxyapatite composition of the particles, cell proliferation was supported during the culture period, and the highest cell proliferation was determined in the GEL/10DB group on day 28. Statistically significant differences were found at 7, 14, 21 and 28 days compared to the pure GEL group in both the -OS and +OS groups. In the +OS induced groups, it was detected that cells proliferated more, and the amount of dsDNA was higher on day 7 compared to the -OS groups. Afterward, the cells continued to proliferate, but proliferation did not increase significantly, which could be explained by the differentiation of the cells, as shown in Figure 4.16 E.

The ALP activity of the cells gradually increased during the 28 days in both -OS and +OS induction. Higher ALP activity was detected in the groups containing more DB particles compared to the pure GEL groups. In addition, ALP activity was detected to be increased even without -OS induction, which may be associated with DB particles' presence in the scaffolds and decent cell–particle interaction. The cells inside the GEL/10DB group (-OS and +OS) showed the highest ALP activity on day 28, with statistical differences compared to the other groups (Figures 4.16 C and E). These high levels of ALP may be due to the hydroxyapatite content of the DB particles, which induce osteogenic differentiation. In a parallel approach, Meesuk et al. demonstrated the proliferation and osteogenic activity of MSC seeded on 3D-printed hydroxyapatite scaffolds for bone regeneration, and 3D-printed hydroxyapatite scaffolds exhibited higher ALP activity and osteogenic gene expression compared to the control group[180].
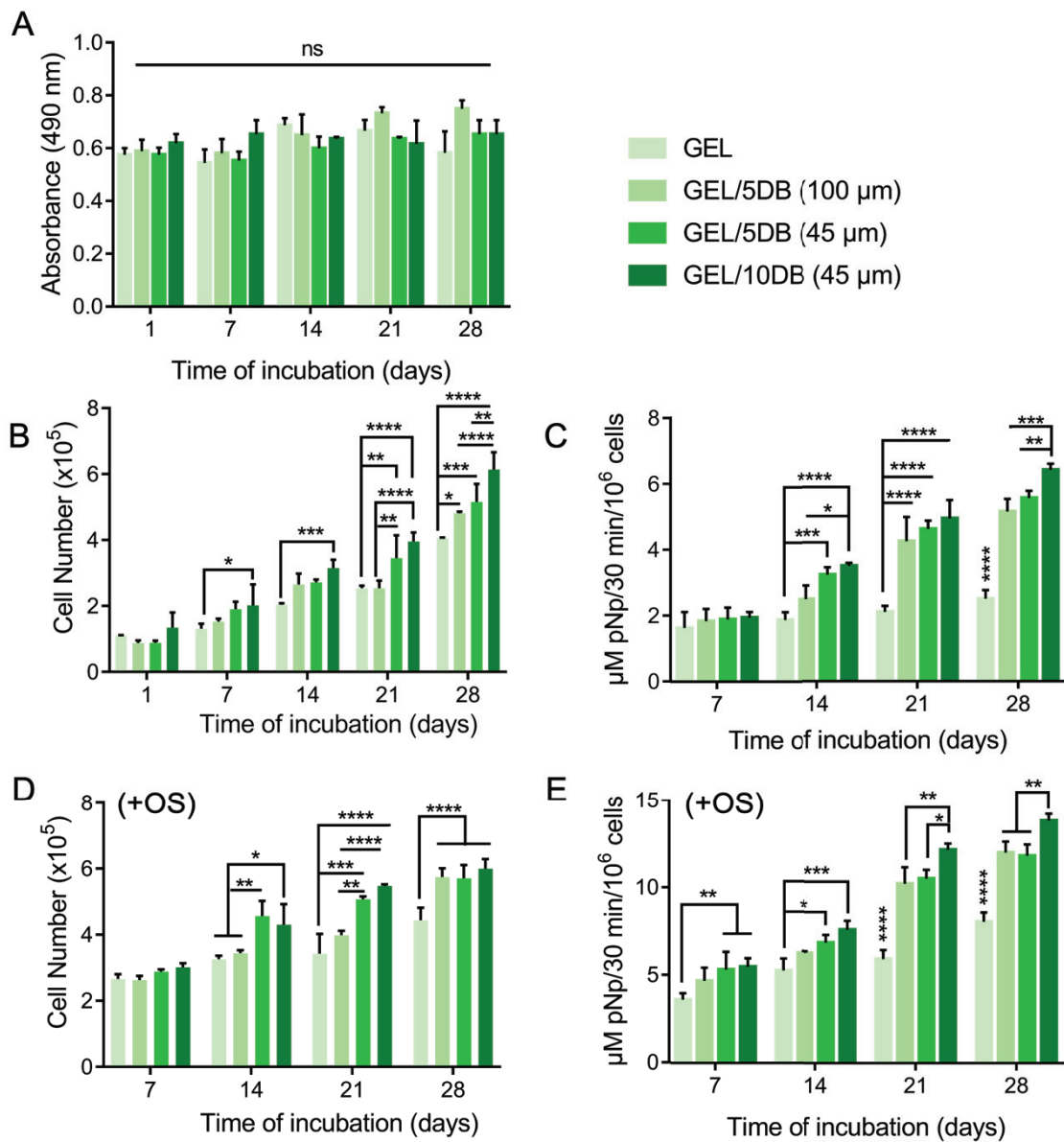
Figure 4.16. Biological activity of hTERT-MSC cells inside the bioprinted GEL/DB scaffolds. (A) Potential cytotoxicity determined by LDH assay. (B) PicoGreen dsDNA assay results show the total number of cells inside the bioprinted scaffolds. Differentiation capacity of cells was assessed by (D) total cell number and ALP secretion (C) without and (E) with osteogenic induction. Data are represented as mean ± SD. *p<0.05 and **p<0.01, ***p<0.001 and ****p<0.0001 indicate statistically significant differences of means between groups by one-way ANOVA tests.

The differentiation study results revealed that scaffolds containing DB particles could support the differentiation of cells both with and without +OS induction, confirming that DB particles could support osteogenic activity. In addition, the synergetic effect of the natural biomineralisation capacity of the DB particles (preserved by our decellularization method) and +OS induction supported the osteogenic differentiation of the hTERT-MSCs, showing that the cells growing inside the GEL/DB scaffolds have a higher differentiation capacity compared to pure GEL scaffolds. Thus, the differentiation studies confirmed the support of osteogenic differentiation using decellularized bone particles, which is the central hypothesis of this thesis study.

4.2.2.5. Cell Morphology inside 3D-Bioprinted GEL/DB Constructs

Confocal microscopy imaging was performed to investigate in detail the cell morphology inside the 3D-bioprinted scaffolds. DAPI and F-Actin stainings were used for cell nuclei (blue) and cytoskeleton (green), respectively (Figure 4.17). DB particles showed a bright autofluorescence, which may result from fibrous collagen in the DB particles, which were seen as a red/pink colour. Confocal microscopy images revealed the morphology and spreading of hTERT-MSCs inside the structures. The images indicate that cells grow and proliferate, interacting with DB particles and covering the entire surface of both the pure GEL and the DB particle incorporated-GEL scaffolds (Figure 4.17). 3D confocal images shows that attached and elongated hTERT-MSCs were observed both inside and on the surface of the 3D-bioprinted structures, showing the cell proliferation and migration throughout the surface of the 3D-bioprinted constructs in both pure GEL and GEL/DB constructs. In GEL/DB groups, cell adhesion demonstrated that cells interacted ideally with homogeneously distributed DB particles in the GEL matrix. The collagen fibers of DB particles may induce cell adhesion inside the GEL matrix. As the DB particles were homogeneously distributed throughout the GEL matrix, as shown in the light microscopy images, cells might be similarly distributed in the 3D-bioprinted structure interacting with the DB particles. Confocal microscopy results reveal that both GEL and DB-incorporated GEL composite bioinks support cell attachment and cell–material interaction.
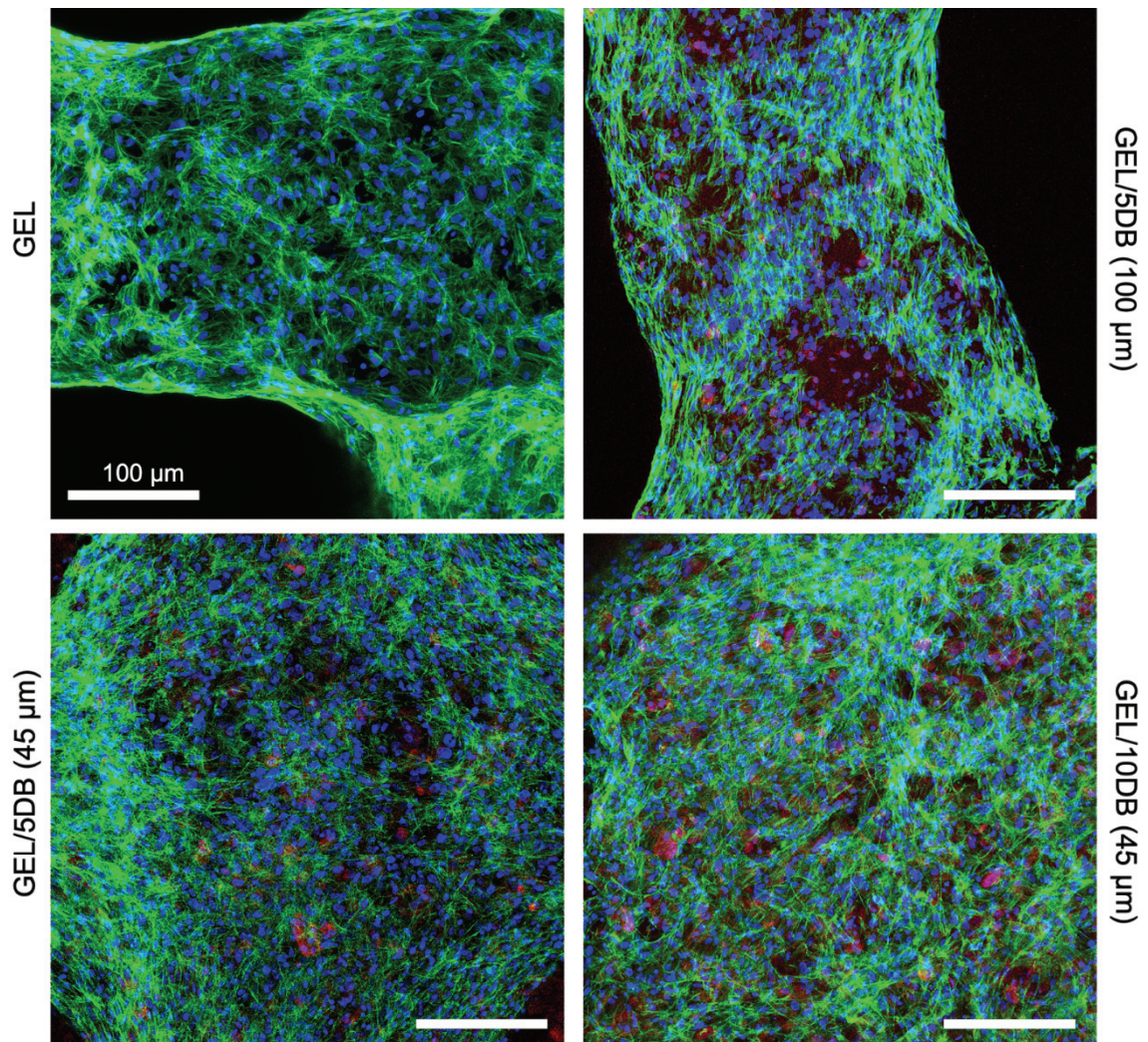
Figure 4.17. Confocal microscopy images of the hTERT-MSCs growing inside the 3D-bioprinted GEL and GEL/DB structures for 14 days of the cell culture period. Nucleus (blue): DAPI, cytoskeleton (green): Actin 488. DB particles (red/pink): autofluorescence. Scale bars: 100 μm.

4.3. Conclusions

This chapter demonstrates the successful fabrication of DB-incorporated composite scaffolds by 3D printing and 3D bioprinting technique. The incorporation of rabbit and bovine bone particles in different sizes and concentrations into the GEL matrix was assessed in terms of their material characteristics and biological activity.

Bone particles were homogeneously distributed within GEL matrix, as revealed by µCT analysis. Rabbit DB particles incorporated-GEL scaffolds were fabricated by the combination of 3D-printing and freeze-drying techniques. 3D-printed composite rabbit-particle-incorporated GEL scaffolds displayed high porosity, with macro- and microporous structures. According to the printability assessment results, pristine GEL and 1% or 3% DB particle incorporated GEL scaffolds exhibited the most uniform strands, with a square-shaped pore morphology compared to 5% group. The Pr factor of the biomaterial inks showed that printability capacity decreased with increasing particle concentration in the groups containing a 100 µm particle size. The highest concentration (5%DB) groups, however, still exhibited a printability of ~0.9, indicating that they could be printed with sufficient shape fidelity for 3D-printing applications. While the data indicate that the 100 µm DB particle concentrations >5% mitigates printing capacity, *in vitro* experiments highlighted that DB particle concentrations <5%, with high printability properties, showed no cytotoxicity but enable a suitable microenvironment for cell proliferation and effective cell–material and cell–particle interactions. The smaller size (45 µm) of bovine particles improved printability using 5% and 10% DB particle concentrations. The bovine particle-incorporated GEL composite biomaterial inks demonstrate appropriate rheological property, with suitable self-recoverability for potential 3D bioprinting applications. The cell culture assays showed similar cellular behaviour compared to the 5% particle concentration. In addition, the 10% particle group demonstrated the highest proliferation and osteogenic differentiation compared to the other groups. hTERT-MSCs were differentiated inside the particle incorporated-GEL structures without osteogenic induction, which might result from the particles' natural hydroxyapatite content. It was demonstrated that cells could migrate inside the structure and completely cover the surface after 3D bioprinting. In addition, as expected, more effective cell–particle interaction was observed inside the 3D-bioprinted structures compared to the cell-seeded scaffolds which exhibited good cell-particle and cell-material interaction as well. The 3D-bioprinting of the composite structures allowed for more cell–particle interactions inside the GEL matrix and increased cell proliferation during the culture period.

The approach of using DB particles as a natural source of collagen and hydroxyapatite in the 3D-bioprinting technique provides excellent interaction with cells, which offers a potential application for the bioinks in bone tissue engineering.

CHAPTER 5

DECELLULARIZED BONE INCORPORATED ALGINATE BIOINKS

The 3D-bioprinting technique offers promising results and allows for the production of tissue-specific scaffolds with a controllable complex microstructure[107,181]. In biofabrication strategies, it is possible to pattern and fabricate living materials with a predefined three-dimension (3D) architecture using computer-aided design and production techniques[99]. In 3D bioprinting, the biomaterial ink and cells or cell-based bioactive components, which are crucial for tissue regeneration, are combined to create a printable material is defined as a 'bioink'. The simultaneous printability of hydrogels with the target tissue cells as a bioink formulation results in the production of 3D live constructs that allow for cell growth inside the construct and that have a strong regeneration capacity for the defected tissues[38].

Most hydrogels are relevant candidates for 3D-bioprinting applications due to their high water content and biocompatibility, providing a 3D environment[108]. In addition to the biocompatibility of hydrogels, the shape fidelity and spatial control ability of the structures after printing are key requirements for the production of complex 3D contracts[182]. Moreover, cells should grow and proliferate inside the printed structures while depositing without adverse effects on the viability and phenotype of the cells[183]. If these requirements are accomplished successfully, 3D constructs could be produced with clinically appropriate shapes and sizes regarding predefined shapes and pore structure. Alginate (ALG), as a biodegradable polymer obtained from brown algae, is commonly used for printing or bioprinting applications. It has high liquid absorption capability, providing good thixotropic properties, and can also be easily cross-linkable with $CaCl_2$, which allows for shape fidelity after printing[184]. Its inferior mechanical properties, however, must be increased to obtain more stable structures. There are various methods to improve mechanical strength: for instance, using a higher polymer concentration or mixing with other polymers. Methylcellulose (MC) is a polysaccharide-based, non-toxic, biocompatible and highly hydrophilic biopolymer that

is used as an additive for food and drug administration in Europe, the USA and most other countries in the world. It has also been used as a viscosity-enhancing polymer; therefore, incorporating MC might improve the alginate hydrogel's viscosity[185]. Besides, the incorporation of the decellularized bovine bone (DB) particles could enhance the mechanical properties of the hydrogels and induce the differentiation of the constructs.

In this chapter we discuss the incorporation of the DB particles into ALG–MC hydrogels and evaluate the printability and biological activity of cells inside the 3D-bioprinted constructs for bone-tissue engineering applications. For this purpose, ALG–MC hydrogels were prepared and mixed with DB particles, then with 3D-bioprinted using human telomerase reverse transcriptase (hTERT) expressing mesenchymal stem cells (MSCs). The stability of the 3D-bioprinted cell-laden constructs was maintained by crosslinking with $CaCl_2$. After 3D-bioprinting, the cell-laden constructs were cultured for 28 days and were characterized in terms of their cytocompatibility and bioactivity as well as morphologically, mechanically and chemically for potential application in bone-tissue engineering.

5.1. Materials and Methods

Preparation of the bioink formulations ALG, MC and DB particles were used. Firstly, ALG (sodium alginates, Sigma-Aldrich) and MC (Sigma-Aldrich; MW=88 kDa) were autoclaved for sterilisation. ALG (3% (w/v)) was dissolved in sterile PBS then mixed with 5% and 9% (w/v) concentrations of MC individually. ALG–MC and DB particles in 100 μm size were mixed at room temperature, resulting in a final concentration of 3% (w/v) ALG, 5% and 9% (w/v) MC and 5% (w/v) DB by stirring until a homogeneous blend was obtained. To prepare bioink composition, hTERT-MSCs were initially sub-cultured in Dulbecco's Modified Eagle Medium (DMEM) supplemented with 1% (v/v) L-glutamine, 10% (v/v) Fetal Bovine Serum (FBS) and 1% (v/v) penicillin-streptomycin. Next, cells were detached from the cell culture flask using Trypsin/EDTA, and the cell number was determined. Cell pellets at a concentration of $5x10^6$ cells/ml were obtained by centrifugation at 1500 rpm and gently mixed with the ALG–MC/DB inks using a mixing unit[186]. The prepared ALG–MC/DB hydrogels with different MC concentrations were referred as ALG-5MC, ALG-9MC, ALG-9MC/DB

and ALG-9MC/DB to indicate the MC concentrations as 5% (w/v) MC (5MC), 9% (w/v) MC (9MC), respectively.

The prepared bioinks were bioprinted at 25 °C using a 3D extrusion bioprinter (GeSiM 3.1, GmbH, Germany). Bioinks were transferred into the cartridge and extruded through a 410 μm diameter conical needle with a tip velocity of 5–10 mm/s. The cell-laden scaffolds were fabricated in a cylindrical shape with 10 layers. After printing, the cell-laden constructs were crosslinked using 100 mM $CaCl_2$ (Sigma-Aldrich, Germany), then placed inside the incubator to return the cells to the physiological environment immediately. The bioprinted cell-laden scaffolds were cultured in DMEM supplemented with 1% (v/v) L-glutamine, 10% (v/v) FBS and 1% (v/v) penicillin-streptomycin (Sigma Aldrich, all supplements) for 28 days in an incubator at 37 °C in a humidified atmosphere of 5% CO and 95% humidity. For the osteogenic induction (+OS), osteogenic supplements: 10^{-7} M dexamethasone, 10 mM beta-glycerophosphate and 0.05 mM ascorbic acid 2-phosphate were added to the cell culture medium, and osteogenic differentiation of cells was induced starting from day 1 of the culture period. 3D-printed scaffolds were characterized in terms of their printability, rheological, morphological, degradation and mechanical properties. The cytocompatibility, proliferation and osteogenicity of the cells inside the 3D-bioprinted scaffolds were also assessed.

5.2. Results and Discussion

5.2.1. Rheological Assessments

The rheological characterization of the ALG-5MC, ALG-9MC, ALG-5MC/5DB, and ALG-9MC/5DB hydrogel precursors was carried out to observe the effect of MC and DB incorporation into the ALG matrix. The viscosity curves revealed that viscosity decreased while the shear rate increased (Figure 5.1 A). All prepared materials, with and without DB particles, demonstrated shear-thinning behaviour, which indicates that all hydrogel precursors prepared have printability capacity. The results, however, were more pronounced for the ALG-9MC and DB-incorporated ALG–MC hydrogel precursors. Viscosity was determined as ~150 Pa/s for the 3ALG-5MC at a

shear rate of 1/s and increased to ~1200 Pa.s for 3ALG-5MC/5DB. Also, the viscosity of 3ALG-9MC and 3ALG-9MC/5DB was determined at 650 Pa.s and 1016 Pa.s, respectively, at a shear rate of 1/s (Figure 5.1 B). The results indicate that viscosity and shear stress were increased with the addition of DB particles. The thixotropy tests described the structural recovery of the material results performed, and all hydrogel precursors showed self-recovery properties. The addition of DB particles did not influence the thixotropic properties (Figure 5.1 C). Although ALG has been commonly used for printing applications, it has poor viscosity. For optimum printability, viscosity is the main parameter, and increasing the polymer concentration is a traditional and quite basic approach. The higher polymer concentration, however, could reduce the viability of cells inside the bioinks while improving printability. From this point of view, the combination of different polymers and the incorporation of biological additives could allow for enhancing viscosity and consequently printability. In a previous study, MC was used as a viscosity-enhancing agent to prepare ALG-based bioink formulation, and ALG–MC blend allowed the printability at clinical size with the relevant rheological properties[187]. In another study, different ALG and MC blends were evaluated to optimise the extrudability properties[188]. MC was chosen as a second polymer due to its thixotropic property and the fact that it allows tunable viscosity for ALG-based bioink formulation. Hence, the 5%MC and 9%MC groups showed the relevant rheological properties. Moreover, the addition of the DB particles significantly increased the viscosity, notably in the 5% MC groups, allowing self-recovery and printability capacity.
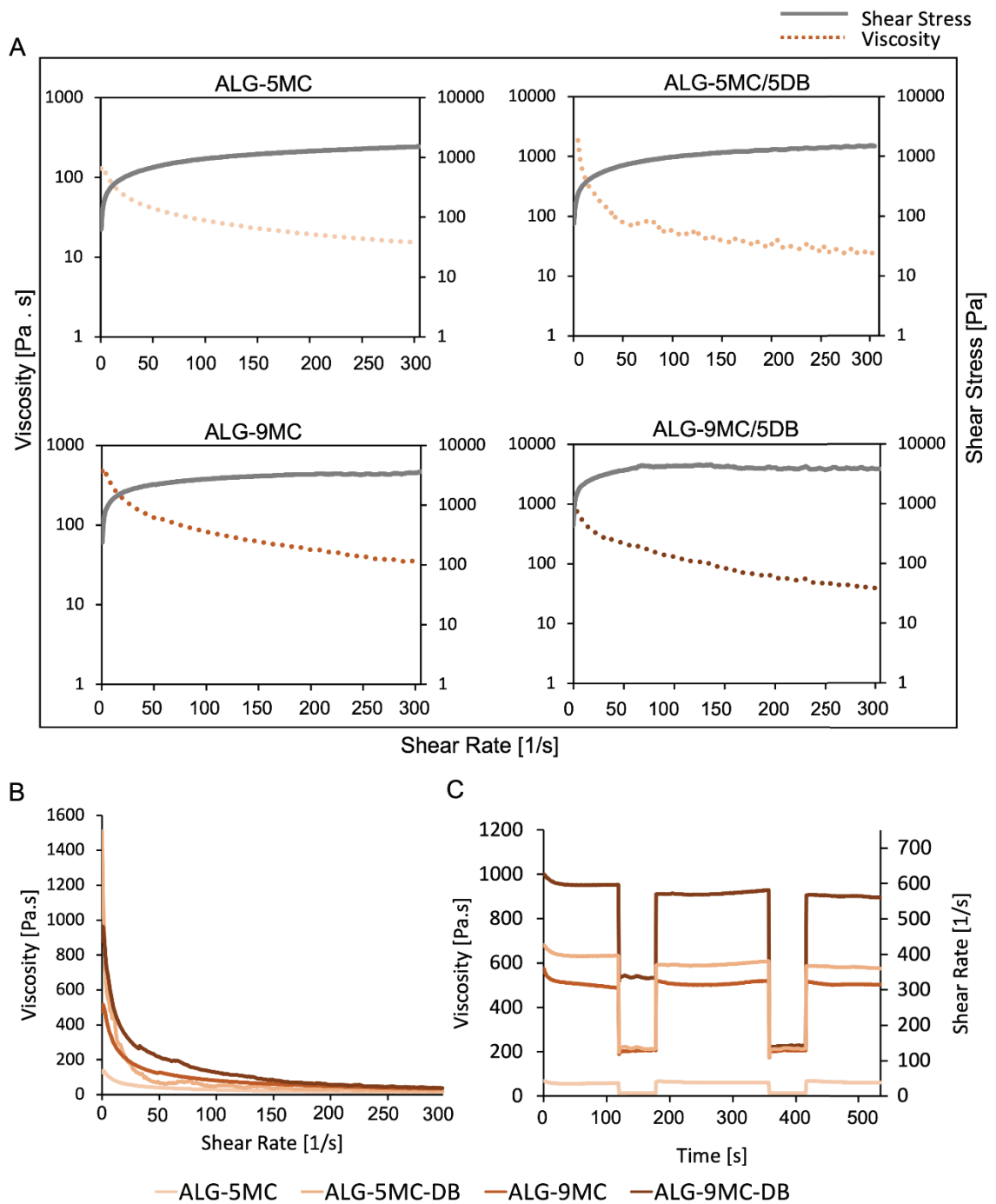
Figure 5.1. Rheological properties of the DB incorporated ALG-MC hydrogels. The measurements were carried out using four sample replicates (n=4), and data are represented as mean.

5.2.2. Fabrication of 3D-Printed ALG-MC/DB Composite Scaffolds

The ALG–MC/DB composite scaffolds were fabricated in circular shapes with 5 layers and 0°/90° strand patterns prior to bioprinting to assess their printability and material characterizations. Figure 5.2 demonstrates the top views of the 3D-printed ALG–MC/DB scaffolds obtained by light microscopy. The light microscopy images depict well-shaped 3D printed structures and a uniform strand diameter (Figure 5.2 A). It was easier to print 3ALG-9MC groups compared to the 3ALG-5MC group. 3ALG-5MC ink tended to fuse during printing due to its low viscosity, as shown in rheological tests (Figure 5.1). In addition, the incorporation of DB particles enabled a precise strand deposition, led by a stable layer-by-layer structure with a neat pore geometry (Figure 5.2 A). Moreover, 3ALG-9MC and DB-incorporated 3ALG-9MC scaffolds were printed easily with consistent strand width, exhibiting higher printability capacity.

The Pr factor was quantified using light microscopy images defined by Ouyang et al.[115]. The DB-incorporated ALG–MC hydrogels exhibited a defined morphology with consistent width in 3D, leading to square pores and uniform grids, which indicate the optimum gelation property for ideal 3D printing. The Pr factor of 3D-printed hydrogels was determined as similar, which was very close to 1 (Figure 5.2 B). The Pr factor of ALG-5MC hydrogels was low compared to the ALG-9MC and showed a tendency toward the fusion of the strands, leading to a more circular pore geometry (Pr=0.9). This value, however, is still acceptable for sufficient 3D deposition[115]. The measurements of the uniformity factor revealed that 3D-printed hydrogels have similar uniformity without statistically significant differences (Figure 5.2 C).

In addition to the Pr and U factors, the strand diameter and pore size of the hydrogels were determined. The strand diameter of ALG-5MC and ALG-5MC/DB groups were measured as 797 ± 6 µm and 730 µm, respectively, and statistically significant differences were detected compared to the ALG-9MC and ALG-9MC/DB groups (Figure 5.2 D). The pore sizes of the 3D-printed ALG-5MC, ALG-5MC/DB, ALG-9MC and ALG-9MC/DB were determined as 420 µm, 389 µm, 624 µm and 642 µm, respectively. The addition of the higher concentration of MC increased the pore size of the 3D-printed hydrogels. Statistically significant differences were detected between 5MC- and 9MC-containing groups (Figure 5.2 E). Hydrogels containing 5MC and 9MC showed statistical differences in both pore size and strand diameter

assessments, but DB incorporation had no influence on the printability and structure of the hydrogels. In accordance with the results of Gelinsky et al., ALG–MC hydrogels were printed with successive layer deposition[187], and with the addition of DB particles did not change the printability in this study.
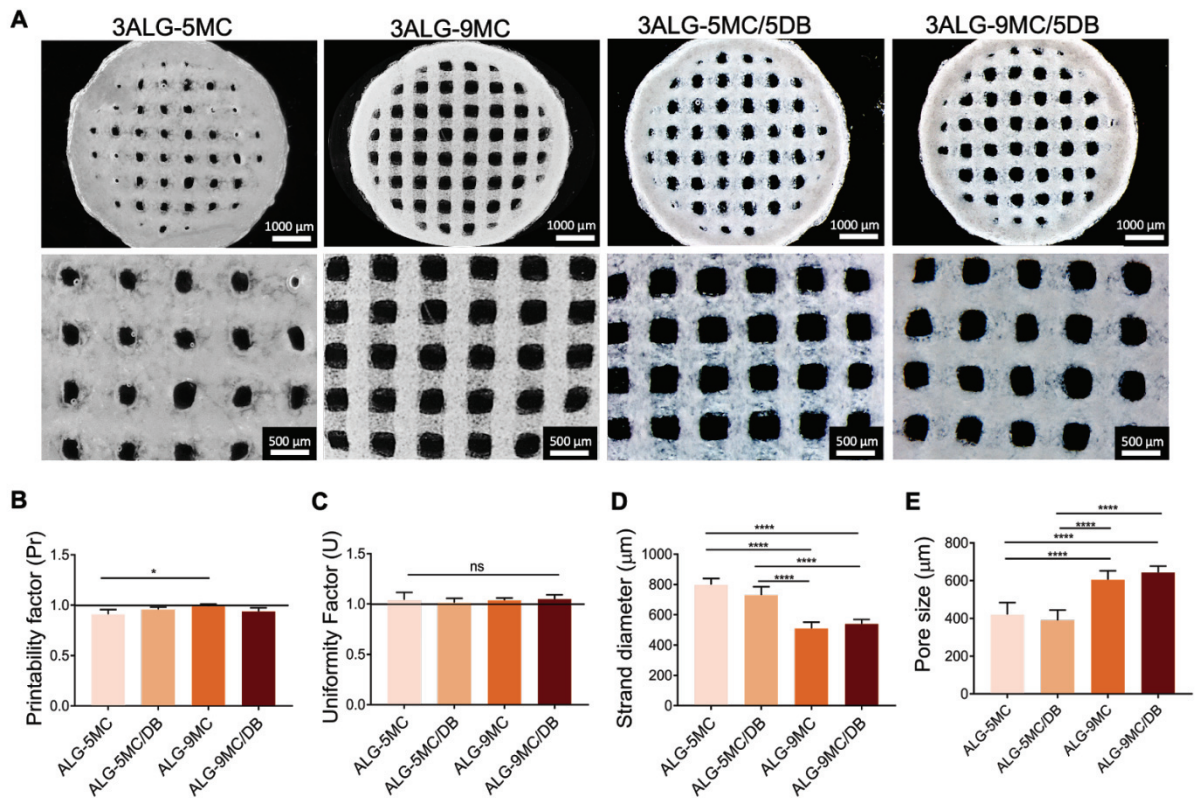
Figure 5.2. Light microscopy images of 3D-printed ALG-MC and ALG-MC/DB composite hydrogels. (A) Light microscopy images of the hydrogels in top and side view after crosslinking. Scale bars: 1000 μm (top), 500 μm (bottom). (B-E) Printability assessments of the ALG-MC and ALG-MC/DB hydrogels (n=4), (B) Printability factor (Pr), (C) Uniformity factor (U), (D) strand diameter, and (E) pore size of the scaffolds. Data are shown as mean ± SD. *p<0.05 and ****p<0.0001 indicate statistically significant differences of means.

5.2.3. Mechanical Properties of ALG-MC/DB Scaffolds

The mechanical properties of ALG–MC and DB-incorporated ALG–MC hydrogels were investigated with compression tests. The samples were printed as 15 layers, and mechanical tests were performed on wet hydrogels. Young's modulus and maximum force that the hydrogels bore until 80% deformation were assessed. Young's modulus of the ALG-5MC and ALG-9MC were found to be 10.74 ± 3 kPa and 13.12 ± 3.6 kPa, respectively, similar to the results of Li et al.'s study[188]. ALG-9MC/DB hydrogels exhibited the highest Young's modulus (16.32 ± 3.1 kPa), and statistically significant differences were found compared to the ALG-5MC and ALG-9MC groups (Figure 4.3A). In addition, Young's modulus of the DB-incorporated ALG-5MC group (13.74 ± 4 kPa) was higher than that of the ALG-5MC (10.74 ± 3 kPa) group, with a statistical difference ($*p<0.05$). In addition, the maximum forces that hydrogels bore until 80% deformation were determined. The data showed that DB incorporation increased the maximum force (Figure 4.3B). Maximum forces were determined as 20.33 kPa, 27.90 kPa, 57.53 kPa and 63.78 kPa for the ALG-5MC, ALG-5MC/DB, ALG-9MC and ALG-9MC/DB groups, respectively. The maximum force bore by the hydrogels increased as the incorporation of the particle increased, and statistically significant differences were found (Figure 5.3B). The compression test results demonstrate the influence of the particles on the mechanical properties of 3D-printed hydrogels, indicating that particle incorporation into the polymer matrix improves the mechanical properties.
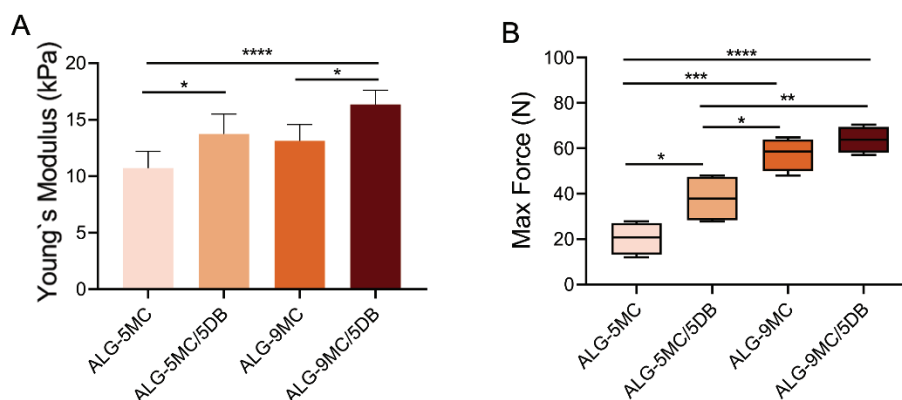
Figure 5.3. Mechanical characterization of the ALG-MC/DB composite hydrogels. (A) Young's modulus of the 3D-printed hydrogels and (B) Maximum force that

the samples can bear until 80% deformation. The compression tests were performed using six replicates (n=6). Data are shown as mean ± SD. *p<0.05, **p<0.01, ***p<0.001 and ****p<0.0001 indicate statistically significant differences by one-way ANOVA test.

5.2.4. Degradation Behaviour of 3D-Printed ALG-MC/DB Scaffolds

The swelling/degradation properties of the ALG–MC and ALG–MC/DB composite hydrogels were assessed by measuring weight changes. Scaffolds were freeze-dried and incubated by immersing cell culture medium for 35 days. At each time point, scaffolds were observed by light microscopy (Figure 5.4 A). All 3D-printed scaffolds were swollen for three days, and higher weight gain was measured on day one for all groups, then scaffolds stayed in the swollen phase for 3 days (Figure 5.4 B). The swelling capacity of the ALG-9MC scaffolds was higher than that of the ALG-5MC groups, with a total weight gain 20% and 25%, respectively on day three (Figure 5.4 B). As similar results, it was also shown previously that the higher MC concentration in ALG–MC composition increased the swelling capacity of the scaffolds[189]. DB-incorporated ALG-5MC and ALG-9MC groups exhibited higher swelling behaviour and were measured as 28% and 32%, respectively on day three. The measurements indicate that the DB particles could increase the swelling capacity. In addition, the scaffolds started to lose mass after reaching the maximum swelling point. Degradation started after 3 days, proceeding with a constant degradation, and approximately 10-15% mass loss was observed for all groups on day 21 then proceed with mass loss on 35 day (Figure 5.4 B). DB particles incorporated groups exhibited more stable behaviour compared to the other groups that lost more mass on day 35 (Figure 5.4 B). It could be concluded that the higher concentration of MC increased the stability of the structure and with the addition of the DB particles, degradation rate decreased.

ALG and ALG-based materials have a slow degradation rate, and mammalian cells has no ability to produce enzymes to degrade the materials[190]. In order to improve degradation behaviour, it can be synthesised by modification of functional groups and could mix with other polymers, such as MC, or incorporation of bioactive particles, as we presented in this thesis study. In addition, the degradation by-products of MC are

mainly glucose, which could be a nutrient for cell culture[185]. Therefore, degradation of the ALG–MC scaffolds could support cell growth during the cell culture period due to its biocompatible by-products.
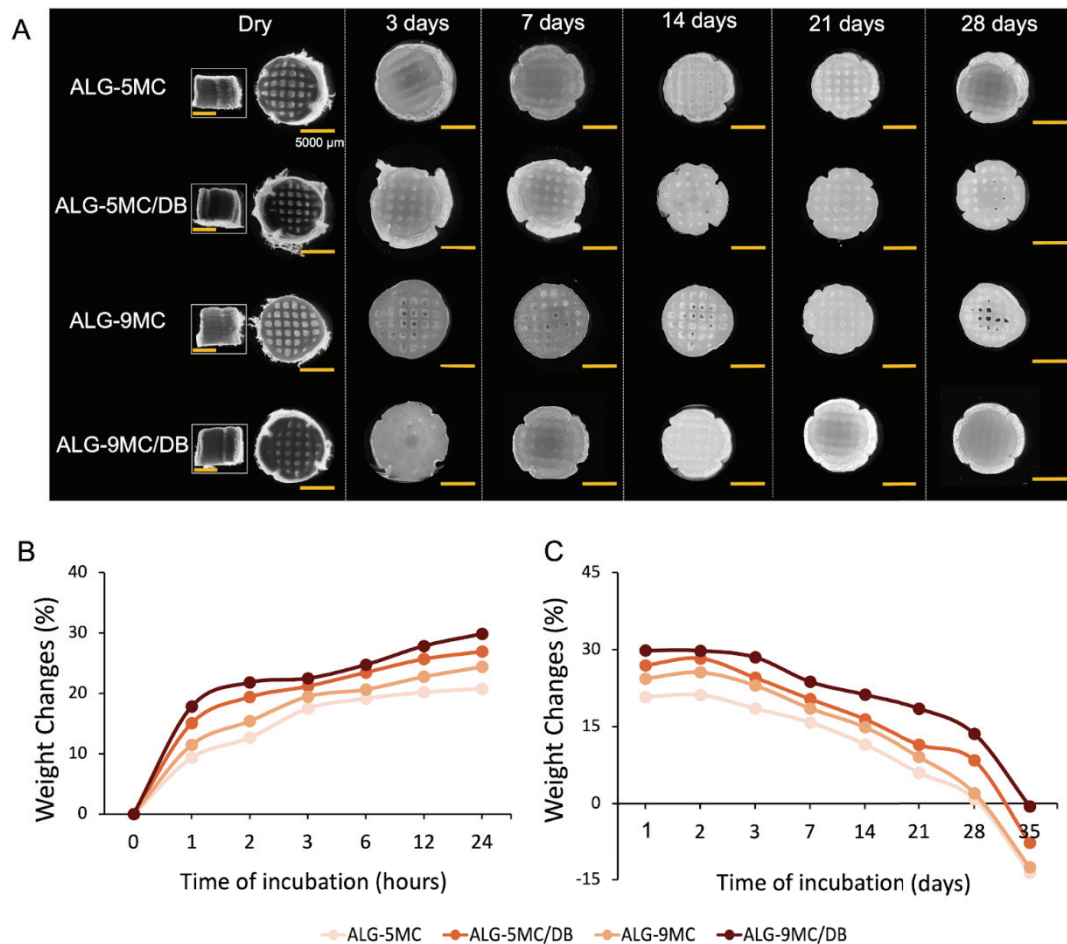
Figure 5 4. . Degradation behaviour of the 3D-printed ALG-MC/DB composite scaffolds. (A) Light microscopy images of the scaffolds at 0, 3, 7, 14, 21 and 28 days of the incubation. Scale bars: 5000 μm. (B) Weight changes of the scaffolds after 24 hours and (C) 35 days incubation.

5.2.5. Cytocompatibility, Cell Growth and Osteogenicity of Cells Inside 3D-Bioprinted Constructs

ALG-MC/DB bioinks were 3D-bioprinted using hTERT-MSCs in circular shapes with 5 layers and cultured for 28 days. The biological activity of the cell-laden scaffolds was assessed in terms of cytotoxicity, biological activity and osteogenecity.

Live/Dead staining was performed to evaluate the cell viability inside the constructs during the culture period. The results reveal cell viability in the 3D-bioprinted ALG–MC and ALG–MC/DB constructs for 28 days of the culture period (Figure 5.5). In the ALG–MC groups, cell viability was higher on day 1, but after day 14 cell viability was slightly decreased. The DB-incorporated ALG–MC scaffolds showed cell viability at each time point of the culture period, and some elongated and spread cells were observed in the 3ALG-5MC/5DB scaffolds.
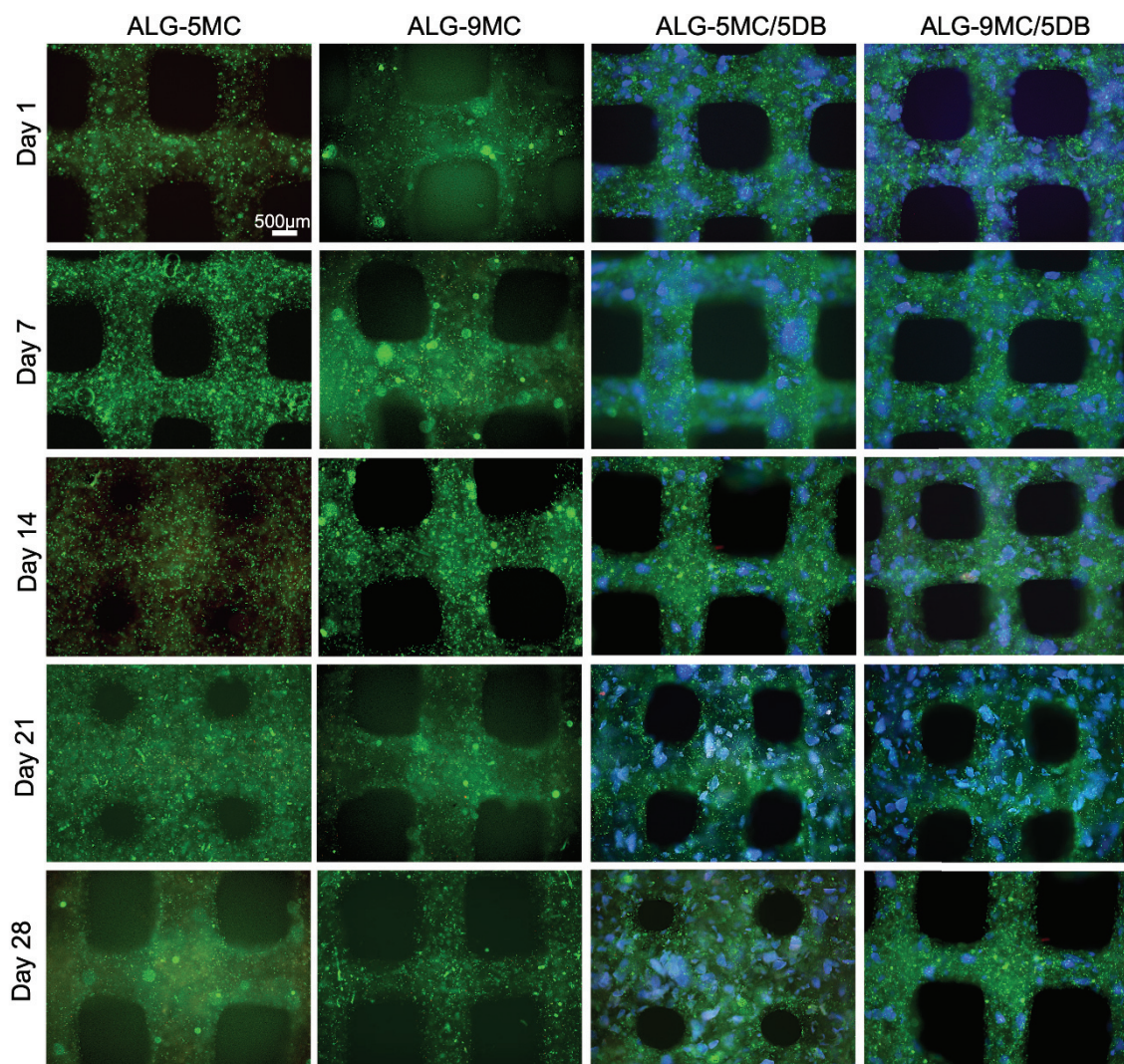
Figure 5.5. Live/Dead staining results of 3D-bioprinted ALG-MC and ALG-MC/DB constructs during 28 days of the culture period. Live cells (Calcein AM, green), dead cells (Ethidium bromide, red), and DB particles (blue, autofluorescence). Scale bars: 500 μm.

The possible cytotoxicity, proliferation and osteogenic differentiation of the cells inside the 3D-bioprinted constructs were investigated (Figure 5.6). The LDH cytotoxicity assay results showed similar LDH levels, except for the ALG-5MC group. A statistical difference was found for the ALG-5MC group compared to the other groups on day seven. LDH levels for ALG-5MC, however, decreased after 7 days. In addition, the LDH levels did not increase during the 28 days of the culture period, which indicates that prepared ALG–MC/DB scaffolds are not toxic for hTERT-MCSs (Figure 5.6 A).

The proliferation of cells inside the scaffolds was quantified with PicoGreen assay based on the dsDNA for 28 days. The dsDNA quantification shows that hTERT-MSCs proliferated and that the DB-incorporated groups exhibited higher cell numbers compared to the ALG-5MC and ALG-9MC groups at each time point (Figure 5.6 B). The cell numbers increased throughout the 14 days in all groups, and the highest cell number was found in the ALG-9MC/DB group, with significant differences compared to the ALG-9MC groups (Figure 5.6 B). After 14 days, the cell number had decreased in both the DB-incorporated and -unincorporated groups (Figure 5.6 B). No statistical differences were found at 14, 21 and 28 days. According to the cell proliferation results, the DB-incorporated ALG–MC composite scaffolds show a more suitable environment for hTERT-MSC cells than do the ALG–MC groups without particles. As a biocompatible polymer, alginate is a good candidate to support cell growth, but MC acts like an inert polymer and does not support cell attachment or growth[191]. For this reason, cell proliferation was affected, and the number of living cells decreased (Figure 5.6 B). In addition, with the addition of the DB particles into the ALG–MC blend, cell proliferation was supported and increased. Similar to our approach, cell proliferation was improved by the addition of different materials, for instance Ahlfeld et al., demonstrated plasma-based AGL-MC bioinks and evaluated MSCs biological activity inside the 3D-bioprinted structures. They found that the plasma-based bioinks support the cell proliferation and differentiation compared to the ALG-MC bioinks[192]. In addition, Liu et al. demonstrated that egg-white powder addition into ALG–MC bioinks improves the biological properties[193].
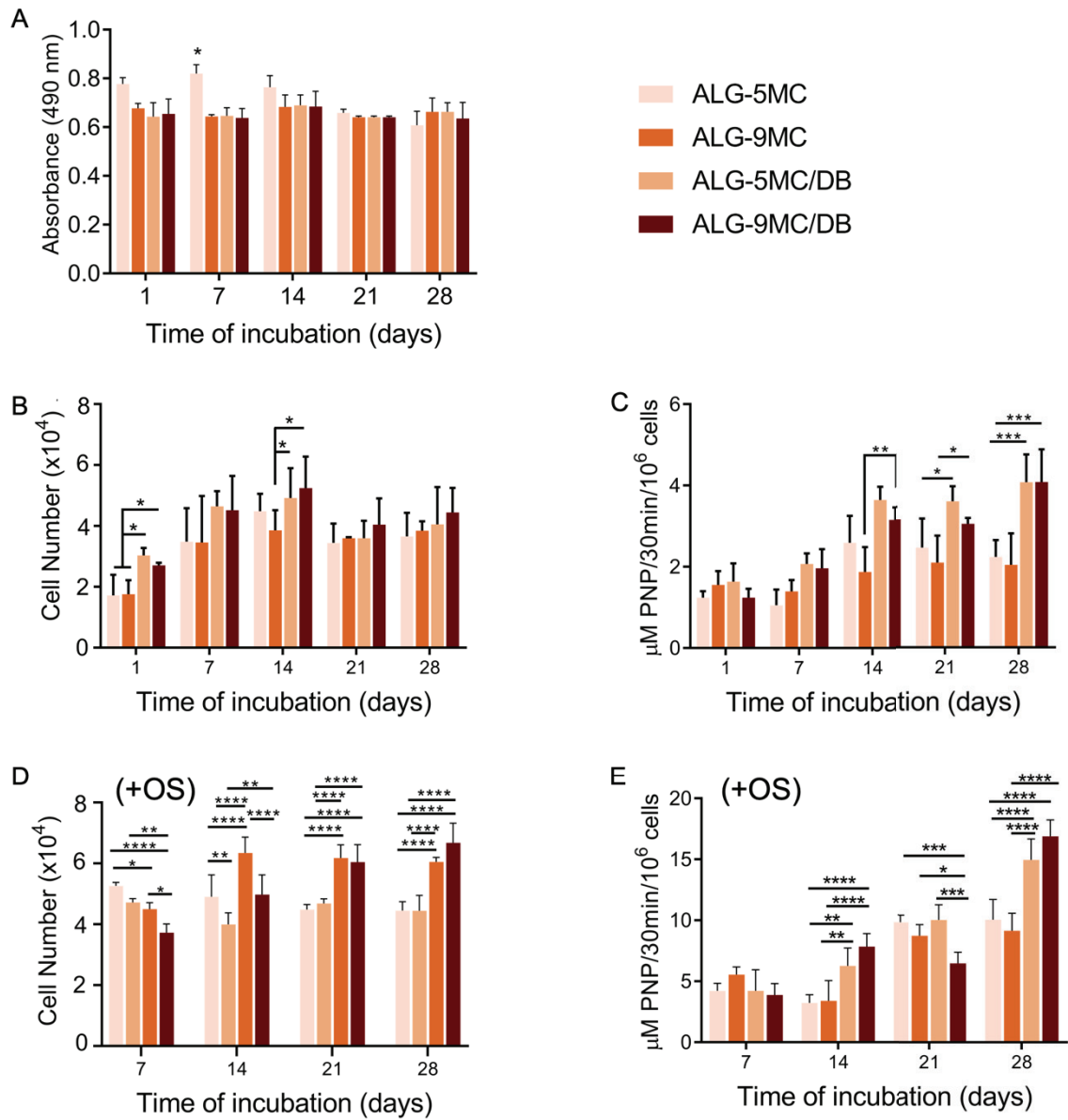
Figure 5.6. Biological activity of hTERT-MSC cells inside the bioprinted ALG-MC/DB constructs. (A) Potential cytotoxicity determined by LDH assay. (B) PicoGreen dsDNA assay results show the total cell number inside the 3D-bioprinted constructs. The differentiation capacity of cells was assessed by (D) total cell number, ALP secretion (C) without and (D) with (+OS) osteogenic induction. Data are represented as mean ± SD. *p<0.05 and **p<0.01, ***p<0.001 and ****p<0.0001 indicate statistically significant differences of means between groups by one-way ANOVA tests.

The osteogenic differentiation capacity of hTERT-MSCs in 3D-bioprinted ALG-MC and ALG-MC/DB constructs was evaluated during the 28 days of the incubation period in terms of proliferation and ALP activity assays. 3D-bioprinted ALG–MC and DB incorporated ALG-MC constructs were cultured with an osteogenic induction (+OS) medium for 28 days. The cell proliferation based on the dsDNA assay shows that hTERT-MSCs proliferated gradually inside the 3D-bioprinted DB incorporated constructs during cell culture period, but the cell number decreased for the ALG-5MC and ALG-9MC groups (Figures 5.6 D). Unlike the non-osteogenic-induced groups, the cell number increased in the DB-incorporated ALG-MC constructs, especially in the ALG-9MC/DB group. Moreover, cell numbers remained relatively the same in the ALG-5MC and ALG-9MC groups during the 28 days of the incubation period. Furthermore, statistically significant differences were found for 7, 14, 21 and 28 days between the DB-incorporated and non-incorporated groups. In the +OS induced groups, it was detected that the hTERT-MSCs inside DB-incorporated ALG-MC groups proliferated more, and the amount of dsDNA was higher on days 21 and 28 compared to the -OS groups.

ALP activity of the MSCs in the 3D-bioprinted constructs was evaluated for the 28-day culture period. The ALP activity of cells in the ALG-5MC and ALG-9MC groups with -OS induction was stable during the 28 days; in the +OS induced groups, however, ALP activity increased as expected, especially on days 21 and 28 (Figures 5.6 C and E). The ALP activity of cells for the DB-incorporated ALG–MC constructs gradually increased during the 28 days in both -OS and +OS induction (Figures 5.6 C and E). The highest ALP activity in the +OS induction groups was detected in the ALG-9MC/DB constructs, with statistically significant differences compared to the other groups (Figure 5.6 E). In addition, ALP activity was detected to be increased even -OS induction, which may be associated with the DB particles present in the constructs. These high levels of ALP may be due to the hydroxyapatite content of the DB particles, which induces osteogenic differentiation.

The differentiation study results reveal that 3D-bioprinted constructs containing DB particles could be more supportive of the differentiation of cells with and without +OS induction. In addition, the synergetic effect of the natural biomineralisation capacity of the DB particles (preserved by our decellularization method) and +OS induction induced osteogenic differentiation of the hTERT-MSCs, showing that the

cells inside the ALG–MC/DB constructs have higher differentiation capacity than without DB incorporation. Thus, the differentiation studies confirmed the support of osteogenic differentiation using decellularized bone particles, which is the main hypothesis of this thesis study.

5.2.6. Cell Morphology inside 3D-Bioprinted ALG-MC Constructs

Confocal microscopy imaging was performed to investigate the cell morphology inside the 3D-bioprinted constructs. DAPI and F-Actin stainings were used for cell nuclei (blue) and cytoskeleton (green), respectively. The DB particles showed a bright signal due to the autofluorescence of fibrous collagen in the DB particles, which were seen as a blue/red/pink colour (Figure 5.7). Confocal microscopy images revealed the morphology of hTERT-MSCs inside the structures. The images indicate that cells grow inside the constructs. Cell adhesion, cell spreading and cell coverage of the construct, however, was not observed in the 3D-bioprinted structures as much as in 3D-bioprinted GEL/DB constructs. This may be caused by the dense structure of the ALG–MC materials. As reported previously, cells have the ability to grow inside the constructs due to the nontoxicity of the biomaterials and cell viability maintained, however, cells cannot be attached to the materials [188]. In numerous studies showed that ALG-based bioinks have lack of cell attachment and with the addition of different materials cell proliferation and attachment improved. It was reported previously, ALG-based bioinks exhibit low cell attachment or cell proliferation (as also shown in Figure 5.6 B) and cells have ability to maintain their viability with loose attachment/interaction with the material[190,194].
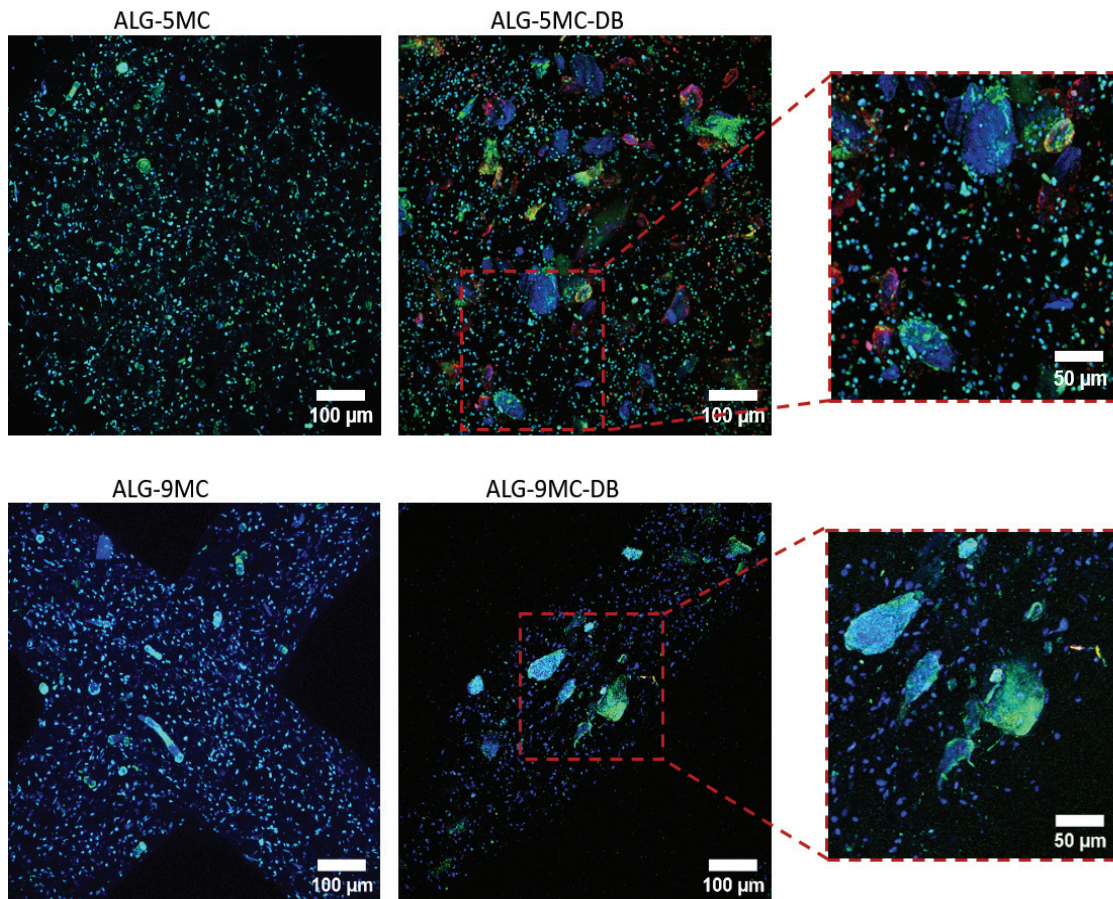
Figure 5.7. Confocal microscopy images of the cells inside the 3D-bioprinted ALG-MC/DB constructs for 14 days of the cell culture period. Nucleus (blue): DAPI, cytoskeleton (green): Actin 488, DB particles (blue/red/pink): autofluorescence. Scale bars: 100 μm, 50 μm (images in red frame).

5.3. Conclusions

This chapter demonstrated 3D biofabrication of DB-incorporated ALG–MC constructs with hTERT-MSC and evaluated its printability, degradation and mechanical stiffness as well as the biological activity of cells inside 3D-bioprinted constructs.

DB-incorporated ALG–MC scaffolds were successfully 3D-bioprinted in 5% MC and 9% MC concentrations. All prepared materials exhibited shear thinning behaviour and have structural recovery capacity according to the rheological test (Figure 5.1). The addition of DB particles significantly increased the viscosity, notably in the 5% MC groups. DB-incorporated ALG-5MC and ALG-9MC scaffolds were 3D-

printed easily and exhibited well-shaped 3D structures with uniform strand diameter (Figure 5.2 A). The incorporation of DB particles enabled a regular strand deposition, led by a stable layer-by-layer 3D structure (Figure 5.2 A). The ALG-5MC group without DB particles showed a tendency to fuse the strands due to its low viscosity, as shown in rheological tests (Figure 5.1). DB incorporation into the ALG-5MC group, however, enhanced printability, as seen in Pr and U factor quantification (Figure 5.2 B). Pr and U factors of 3D-printed hydrogels were determined as similar, which were very close to 1, indicating the optimum gelation property for ideal 3D printing (Figures 5.2 B and C). ALG–MC hydrogels were printed with successive layer deposition, and DB incorporation had no influence on the printability and structure of the hydrogels. In addition, according to the mechanical test results, DB-particle incorporation into the polymer matrix improves the compressive modulus (Figure 5.3 A). With the swelling/degradation experiments, it was confirmed that all 3D-printed scaffolds are swollen for three days, then degradation begins, with a consistent degradation and 20% mass loss observed for day 21 (Figures 5.4 B and 5.4 C).

ALG-MC/DB bioinks were 3D-bioprinted using hTERT-MSCs and cultured for 28 days. LDH assays confirmed the non-toxicity of the materials (Figure 4.6A), and dsDNA quantification showed that cell number decreased after 14 days (similar to the Live/Dead staining), but the DB-incorporated groups exhibited higher cell numbers compared to the ALG-5MC and ALG-9MC groups (Figure 5.6 B). The ALP activity of cells in the ALG–MC/DB groups gradually increased, especially on days 21 and 28 in the +OS induced groups (Figures 5.6 C and 5.6 E). In addition, increasing ALP activity was detected in the ALG–MC/DB groups without osteogenic induction, indicating that DB particles support osteogenic differentiation, as also demonstrated in *Chapter 4*.

In conclusion, DB-particle-incorporated ALG–MC composite scaffolds exhibited well-shaped 3D structures with the high printability capacity of the ALG–MC blends. Although exhibited lower cell viability in the later period of the culture, ALG–MC/DB bioinks allowed for the differentiation of cells inside the structures and supported osteogenic differentiation. The results show that, with the addition of DB particles, both the mechanical properties and biological activity of cells were enhanced due to the collagen fibers and hydroxyapatite crystal content of the DB particles. Thus, a novel bioink was developed that could be a promising candidate for bone tissue engineering applications.

CHAPTER 6

DECELLULARIZED BONE INCORPORATED ALGINATE-GELATIN BIOINKS

Biofabrication technique with tailored architecture and cell organisation is a main focus in additive-manufacturing and regenerative-medicine applications. Recently, many studies have described the novel techniques and novel materials for the fabrication of three-dimemsion (3D) structures[108,195,196]. Hydrogels are mainly used with cells for the fabrication of 3D structures due to their highly hydrated 3D environment and as they allow cell encapsulation. The main important points in the fabrication of cell-laden structures are the production of 3D constructs with clinically relevant sizes and high shape fidelity constructs with adequate mechanical stiffness, as well as the maintenance of cell viability and bioactivity[187]. Therefore, the key challenge faced in the 3D-biofabrication technique is the development of ideal tissue-specific materials that can maintain the balance between the shape fidelity of the structure and cell growth after bioprinting.

Alginate-based bioinks are the most-used biopolymer in biofabrication techniques due to their good thixotropic property, easy printability and crosslink capacity[184,197–199]. On the other hand, gelatin (GEL) provides a suitable environment for cell growth due to its biocompatibility and arginyl-glycyl-aspartic acid (RGD) sequence. As demonstrated in *Chapter 4*, bioprinting of GEL bioinks with human telomerase reverse transcriptase (hTERT) expressing mesenchymal stem cells (MSCs) exhibited high cell viability, proliferation and complete cell coverage of the 3D-bioprinted structures. In addition, gelation of the GEL is controllable due to its thermoresponsive property and easily crosslinkable with biocompatible microbial transglutaminase (mTG), as shown in *Chapter 4*. Besides the excellent cytocompatibility of GEL, alginate-methylcellulose (ALG–MC) bioinks exhibited higher shape fidelity and printability capacity, however, lower cell viability was observed, as shown in Chapter 5. Therefore, in this chapter, ALG–GEL-based bioinks with hTERT-MSCs were prepared to obtain higher shape fidelity and higher cell

viability. Decellularized bone (DB) particles obtained from bovine femurs were used as a bioactive additive to improve the mechanical strength and biological activity of MSCs. After bioprinting, stability of the cell-laden constructs was maintained by crosslinking with $CaCl_2$ and mTG. 3D-bioprinted constructs were cultured for 28 days and characterized in terms of their cytocompatibility and bioactivity as well as morphologically, mechanically and chemically for potential application in bone-tissue engineering.

6.1. Materials and Methods

ALG–GEL-based biomaterial inks were prepared using 3% (w/v) ALG, 7.5% (w/v) GEL and 5% (w/v) MC, then mixed with 5% (w/v) DB particles to obtain composite inks. ALG, GEL and MC were prepared by dissolving in ultrapure water as described *Chapter 4* and *Chapter 5*. The concentration of ALG, GEL, MC and DB particles did not change, but different volumes of ALG and GEL were used as 1:1, 1:2 and 2:1 (ALG:GEL (v/v)) to assess the addition of GEL in ALG–MC blends. Next, 5% DB particles (100 μm size) were mixed with each blend to assess the incorporation of DB particles. For the bioink formulation, hTERT-MSC cells were used.

For the bioink composition, hTERT-MSCs were used, and a cell pellet (5×10^6 cells/ml) was prepared by centrifugation at 1250 rpm, then mixed with prepared ink materials using a mixing unit[186]. Prepared bioinks were bioprinted using a 3D-extrusion bioprinter (Bioscaffolder 3.1, GeSiM, GmbH, Germany). The cartridge holder temperature was set to 25 °C to stabilise the viscosity. Bioinks were transferred into the cartridge and extruded through a 410 μm diameter conical needle with a tip velocity of 5–10 mm/s. The scaffolds were fabricated in a cylindrical shape with five layers. After printing, cell-laden constructs were crosslinked using equal amounts of 10% mTG (Ajinomoto ACTIVA WM, 85−135 U/g) and 100 mM CaCl to stabilise the scaffolds. After washing twice with HBSS, DMEM containing 1% (v/v) L-glutamine, 10% (v/v) FBS and 1% (v/v) penicillin-streptomycin (Sigma Aldrich, all supplements) were added to the cell-laden scaffolds. The bioprinted cell-laden scaffolds were cultured for 28 days in an incubator with a humidified atmosphere of 5% CO and 95% humidity. For the osteogenic induction (+OS): 0.05 mM ascorbic acid 2-phosphate, 10^{-7} M

dexamethasone and 10 mM beta-glycerophosphate were added to the cell culture medium, and osteogenic differentiation of cells was induced, starting from day one of the culture period. 3D-printed scaffolds were characterized in terms of printability as well as their rheological, morphological, degradation and mechanical properties, and the cytocompatibility, proliferation, and osteogenicity of the cells inside the 3D-bioprinted scaffolds were also assessed.

6.2.   Results and Discussions

6.2.1. Rheological Assessments

Rheological characterization of the ALG-GEL-MC and ALG-GEL-MC/DB hydrogel precursors was performed to observe the influence of GEL and DB addition to the ALG–MC precursors and evaluate the viscosity properties for printing. All prepared materials, both with and without DB particles, exhibited a shear-thinning behaviour that indicates that all materials have printability capacity (Figure 6.1 A). In addition, shear stress increased when the shear rate increasing during the tests (Figure 6.1 A). Shear stress of all precursors exhibited similar behaviour under shear rate similar with the viscosity results. The viscosity curves show that viscosity decreased while the shear rate increased (Figure 4.1 B). The addition of the GEL increased viscosity, as notably seen in the curve of the 1:2 group (Figure 6.1 C). In addition, DB incorporation increased the viscosity in each prepared blend. At a shear rate of 1/s, the viscosity of the 1:1, 1:2, 2:1, 1:1/DB, 1:2/DB and 2:1/DB groups was determined as 410 Pa.s, 653 Pa.s, 494 Pa.s, 526 Pa.s, 680 Pa.s, 505 Pa.s, respectively (Figure 6.1 C). The highest viscosity was obtained for 1:2/DB group containing DB particles and higher GEL content.
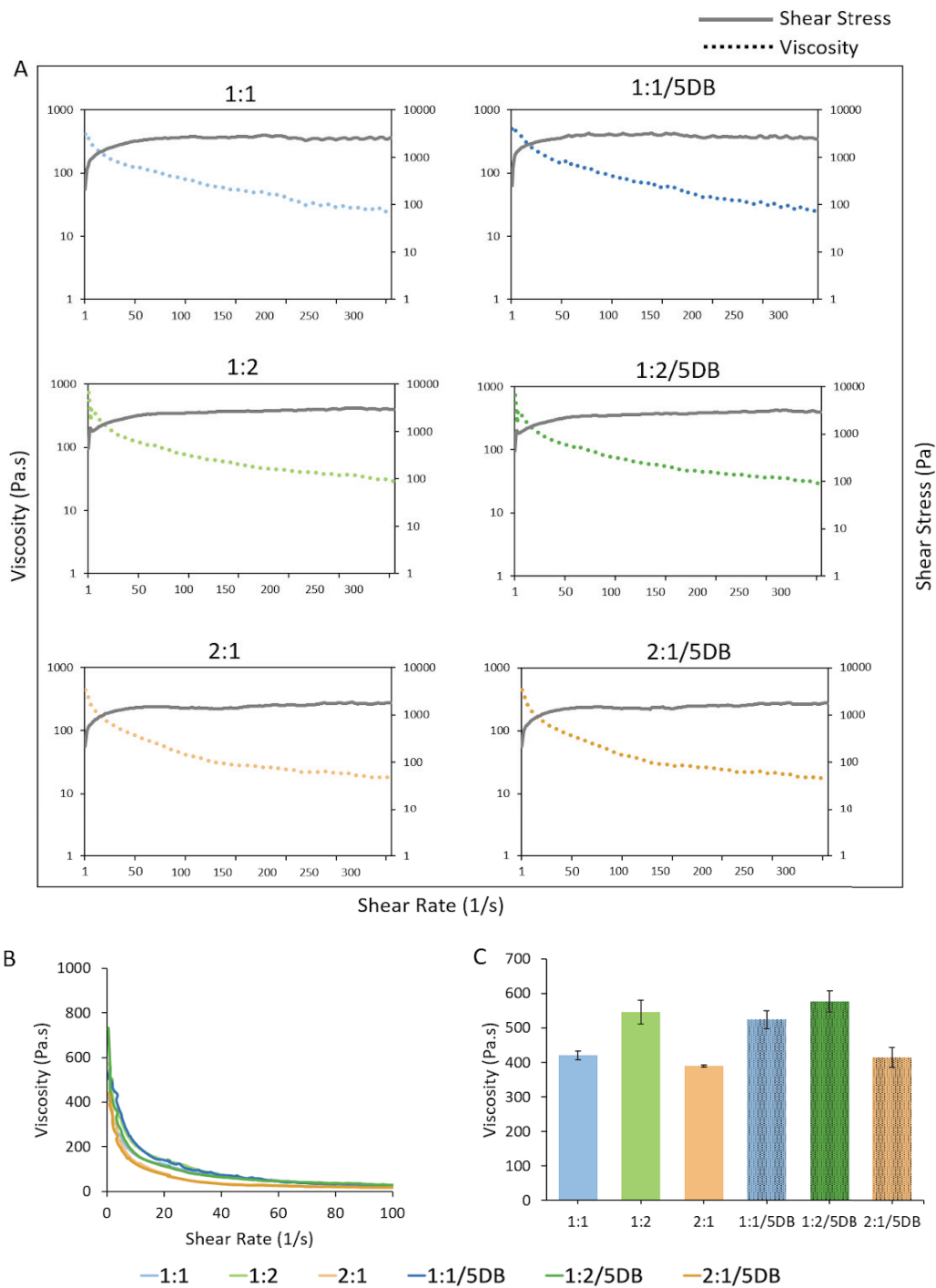
Figure 6.1. Rheological properties of the ALG-GEL-MC and ALG-GEL-MC/DB blends (A). The measurements were carried out using four sample replicates (n=4), and data are represented as mean. (B) The decreasing viscosity of prepared blends while shear rate increasing, which indicate printability capacity. (C) Viscosity of ALG-GEL-MC and ALG-GEL-MC/DB blends obtained at a shear rate of 1/s.

6.2.2. Fabrication of 3D-Printed ALG-GEL-MC/DB Scaffolds

ALG-GEL-MC/DB composite scaffolds were fabricated in a circular shape with five layers prior to bioprinting with cells. Figure 6.2 A shows a top view of the 3D-printed scaffolds obtained by light microscopy. Light microscopy images depicted well-shaped 3D-printed structures with ideal, square pore geometry (Figure 6.2 A). Printing of the 3ALG-5MC did not change with the addition of the GEL and it was easy to preserve the shape fidelity of the 3D scaffolds. As seen in light microscopy images, 1:1 group exhibited the optimum square pore geometry compared to the other scaffolds. The 2:1 and 1:2 groups, however, also have well-shaped structures, and it was possible to print more than 15 layers. In addition, the incorporation of the DB particles increased the strand diameter, notably in the 2:1/DB groups (Figure 6.2 A and 6.2 D). Nevertheless, well-shaped 3D scaffolds were obtained with suitable shape fidelity.

The Pr factor, U factor, strand diameter and pore size of the 3D-printed scaffolds were quantified using light microscopy images. The DB-incorporated ALG-GEL-MC scaffolds exhibited defined morphology, leading to square pores and uniform grids. The Pr factor of the 3D-printed hydrogels was determined as similar, which was very close to 1 (Figure 6.2 B). The Pr factor of the 2:1 and 2:1/DB scaffolds was lower compared to the other groups, but the Pr factor (Pr=0.9) was still acceptable for sufficient 3D deposition (Ouyang et al., 2016). The measurements of the uniformity factor revealed that 3D-printed hydrogels have similar uniformity, and there were no statistically significant differences between the scaffold groups (Figure 6.2 C). The strand diameters of the 1:1, 1:2, 2:1, 1:1/DB, 1:2/DB and 2:1/DB scaffolds were measured as 566 µm, 447 µm, 721 µm, 618 µm, 467 µm and 643 µm, respectively (Figure 6.2 D). The highest strand diameter was determined in the 2:1 and 2:1/DB groups, with statistically significant differences compared to the other groups (Figure 6.2 D). The pore sizes of the 1:1, 1:2, 2:1, 1:1/DB, 1:2/DB and 2:1/DB scaffolds were determined as 623 µm, 610 µm, 458 µm, 609 µm, 600 µm and 564 µm, respectively (Figure 6.2 E). Statistically significant differences were detected among these groups. Similar to the strand diameter data, no statistical differences were found between the DB-incorporated and DB-non-incorporated groups (Figure 6.2 E). In addition, the pore sizes obtained in all hydrogel groups are suitable for cell attachment, proliferation and diffusion of the nutrients in bone tissue engineering applications[98,153].

With the combination of the rheology and printability assessments, the results indicate that all blends have printability capacity and exhibit well-shaped 3D geometry, with suitable shape fidelity.
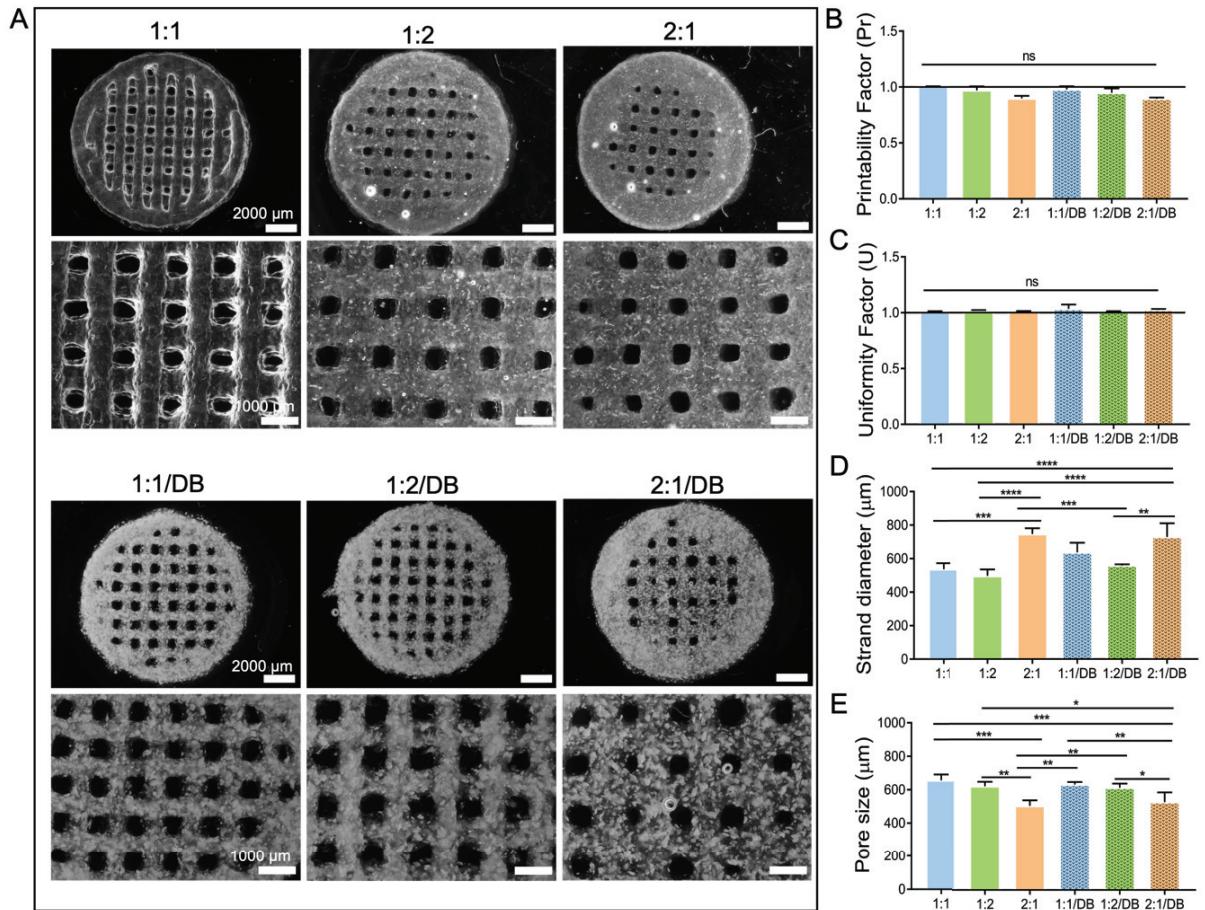
Figure 6.2. Light microscopy images of 3D-printed ALG-GEL-MC and ALG-GEL-MC/DB composite hydrogels. (A) Light microscopy images of the hydrogels in top view after crosslinking. Scale bars: 2000 μm (top), 1000 μm (bottom). (B–E) Printability assessments of the ALG-GEL-MC and ALG-GEL-MC/DB hydrogels (n=4), (B) Printability factor (Pr), (C) Uniformity factor (U), (D) strand diameter, and (E) pore size of the scaffolds. Data are shown as mean ± SD. *p<0.05 **p<0.01, ***p<0.001 and ****p<0.0001 indicate statistically significant difference of means.

6.2.3. Mechanical Properties of 3D-Printed ALG-GEL-MC/DB Scaffolds

The mechanical properties of ALG-GEL-MC and DB-incorporated ALG-GEL-MC scaffolds were investigated with compression tests. Samples were printed as 15 layers, and compression tests were performed with wet hydrogels. Young`s modulus and the maximum force that the hydrogels could bear until 80% deformation were quantified. Young`s modulus of the 1:1, 1:2, 2:1, 1:1/DB, 1:2/DB and 2:1/DB scaffolds was found to be 11.20 ± 1.8 kPa, 16.01 ± 2 kPa, 23.86 ± 5 kPa, 14.19 ± 2 kPa, 15.42 ± 3.4 kPa and 16.55 ± 3.9 kPa, respectively (Figure 6.3A). The 2:1 scaffold exhibited the highest Young's modulus, and statistically significant differences were found between it and the 1:1 and 2:1/DB groups. The incorporation of the DB particles slightly increased Young's modulus, but there were no statistical differences between DB-incorporated and non-incorporated groups except the 2:1/DB group.
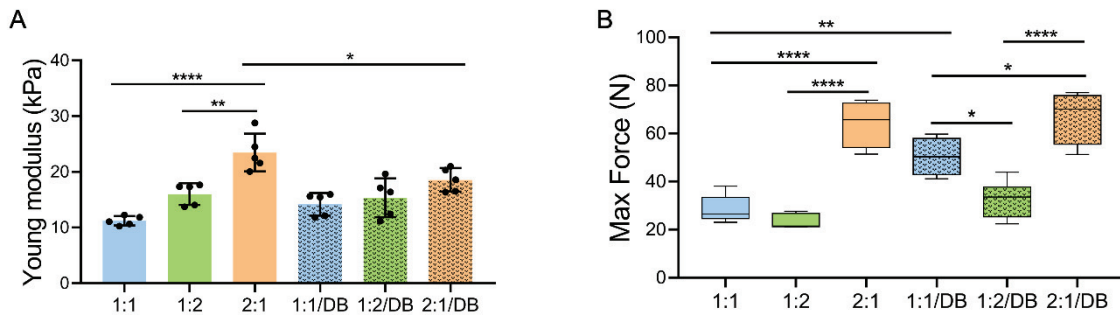
Figure 6.3. Mechanical characterization of the DB particles incorporated-ALG-GEL-MC composite hydrogels. (A) Young's modulus of the 3D-printed hydrogels and (B) Maximum force that the samples can bear until 80% deformation. The compression tests were performed using six replicates (n=6). Data are shown as mean $\pm$ SD. *p<0.05, **p<0.01, ***p<0.001 and ****p<0.0001 indicate statistically significant differences compared to 3D-printed ALG-GEL-MC and ALG-GEL-MC/DB hydrogels by one-way ANOVA test.

In addition, the maximum forces that the hydrogels could bear until 80% deformation were determined with compression tests. The data showed that DB incorporation increased the maximum force (Figure 6.3B). Maximum forces were

determined as 28.48 kPa, 22.32 kPa, 54.15 kPa, 50.34 kPa, 31.91 kPa and 57.12 kPa for 1:1, 1:2, 2:1, 1:1/DB, 1:2/DB and 2:1/DB scaffolds, respectively. The highest maximum force was found in the 2:1 and 2:1/DB groups, and statistical differences were found compared to the other groups (Figure 6.3B). Moreover, the maximum force borne by the hydrogels increased with the incorporation of DB particles, notably between the 1:1 and 1:1/DB groups, with statistically significant differences (Figure 6.3B). The compression test results demonstrate the influence of the particles on the mechanical properties of 3D-printed hydrogels, indicating that particle incorporation into the polymer matrix improves the mechanical properties.

6.2.4. Cytocompatibility, Cell Growth inside the 3D-Bioprinted Constructs

ALG-GEL-MC/DB scaffolds with different ALG and GEL combinations 1:1, 1:2 and 2:1 (ALG:GEL (v/v)) were bioprinted using hTERT-MSC cells in a circular shape with five layers and the biological activity of the cell-laden scaffolds was evaluated by fluorescence microscope and biochemical assays.

Live/Dead staining assay was performed to evaluate the cell viability inside the scaffolds during the culture period. Fluorescence images depicted cell viability in the 3D-bioprinted ALG-GEL-MC/DB scaffolds during the 28 days of the culture period. The fluorescence images showed the live cells (green), dead cells (red) and DB particles (blue, autofluorescence property of particles; Figure 6.4). On day one, dead cells were visible inside the bioprinted constructs then the number of dead cells decreased on the following days of the culture. At each incubation time, cell viability was high in all scaffolds, and the attached cells formed clusters, especially in 1:2/DB scaffolds, on day one and then spread inside the 3D-bioprinted constructs. On day 14, the cells started to elongate in the constructs, especially in the 2:1/5DB scaffolds. As seen in the fluorescence images cells elongated on the DB particles showing a well interaction with both material and particles (Figure 6.4). Cells growing inside the bioprinted constructs maintained their viabilities until day 28 of the culture period, which indicates that the prepared bioink formulations are cytocompatible.
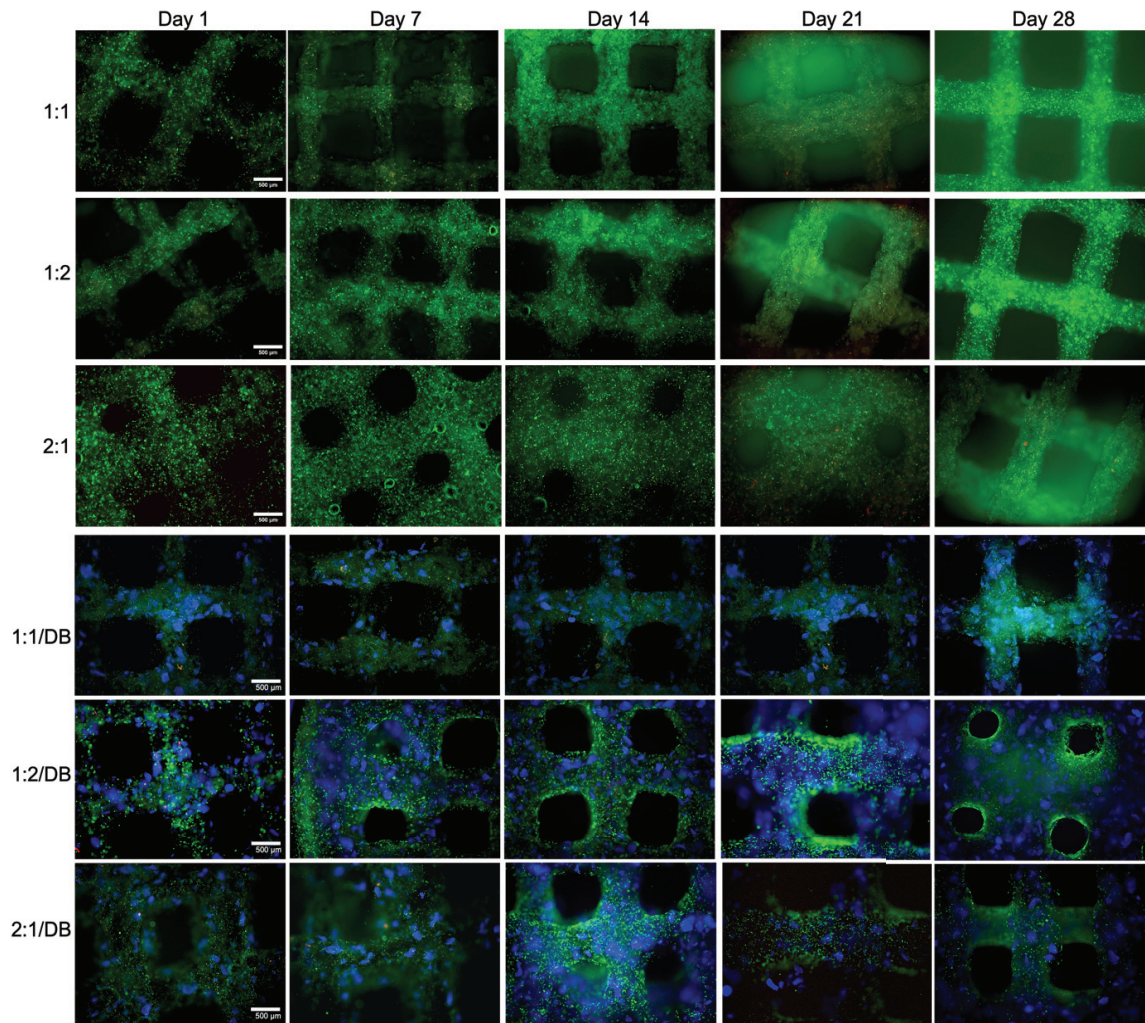
Figure 6.4. Live/Dead staining results of 3D-bioprinted ALG-GEL-MC and ALG-GEL-MC/DB constructs during the 28 days of the culture period. Live cells (Calcein AM, green), dead cells (Ethidium bromide, red), DB particles (blue, autofluorescence) Scale bars: 500 µm.

The potential cytotoxicity of the ALG-GEL-MC/DB scaffolds was assessed by LDH cytotoxicity assay and the results showed that the cytotoxicity level of the cells inside the 3D-bioprinted constructs was mainly stable during the 28 days of the culture period (Figure 6.5 A). At the beginning of the culture period, on day one and day seven, LDH levels were higher compared to the other time points of the culture, especially the highest LDH level detected in the 2:1 group. Following these time points, however, LDH levels decreased, with no statistical differences among groups, which indicates that the ALG-GEL-MC and ALG-GEL-MC/DB bioinks have no cytotoxic effect on hTERT-MSCs.

The proliferation of the cells inside the bioprinted constructs was quantified during 28 days of the culture period. PicoGreen assay based on dsDNA quantification shows that hTERT-MSC cells gradually proliferated inside the bioprinted constructs (Figure 6.5 B). Notably, scaffolds with higher GEL amounts significantly supported cell proliferation in comparison to other groups. Higher cell proliferation was determined on day 28 and statistically significant differences were found compared to other groups (Figure 6.5 B). In addition, higher cell proliferation was reached with the addition of GEL into the ALG-MC structure in comparison to the data demonstrated in *Chapter 5* (Figure 5.6 B).

To assess the differentiation capacity of the cells, 3D-bioprinted ALG-GEL-MC/DB constructs were incubated with an osteogenic induction medium for 28 days, and PicoGreen dsDNA and ALP activity assays were performed. The results show that hTERT-MSC cells proliferated in all groups during the 28 days of the culture period (Figure 6.5 D). Unlike the non-osteogenic groups, cell numbers inside the 1:1, 1:2 and 2:1 groups were higher than in the DB-incorporated groups, with statistical differences. On day 28, cells inside the constructs reached a similar cell number, but statistical differences were found between groups (Figure 6.5 D). In addition, the total cell number inside the 1:2 scaffolds was higher in both the +OS and -OS groups, which indicates that the addition of the GEL into the ALG–MC bioink provides a more favourable environment for hTERT-MSC cells and allows cell growth inside the hydrogels.

The ALP activity of the cells in 3D-bioprinted constructs was evaluated for a 28-day culture period. The ALP activity of the cells in groups without DB particles and -OS induction was stable throughout the 28 days, without statistical significant differences among groups or time periods (Figure 6.5 C). In addition, the ALP activity of cells inside DB-incorporated constructs increased slightly after 14 days, and statistically significant differences were found among the groups without DB particles (Figure 6.5 C). In all +OS induced groups, ALP activity increased during the culture period as expected, especially on days 21 and 28 (Figure 6.5 E). The ALP activity of the cells inside the DB-incorporated ALG-GEL-MC constructs was higher than in the groups without DB particles throughout the 28 days (Figure 6.5 E). In accordance with the proliferation assay, the +OS induced groups showed higher ALP activity. The GEL addition enhanced the proliferation and therefore osteogenic differentiation in the structures compared to the ALG-MC constructs (*Chapter 5, Figure 5.6 E*).
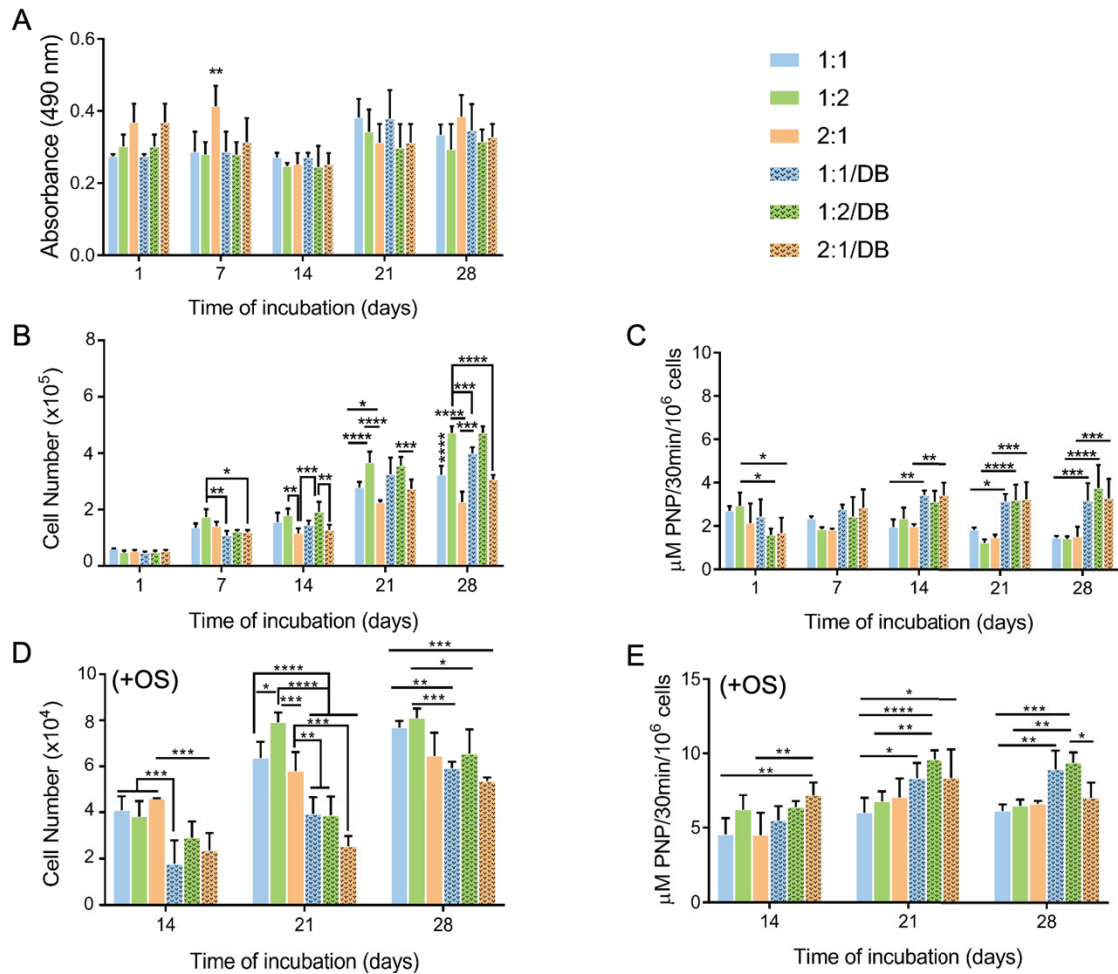
Figure 6.5. Biological activity of hTERT-MSC cells growing inside the bioprinted ALG-GEL-MC/DB constructs. (A) Potential cytotoxicity determined by LDH assay. (B) PicoGreen dsDNA assay results show the total cell number inside the bioprinted constructs. Differentiation capacity of cells assessed by (D) total cell number in osteogenic medium and also by ALP secretion (C) without and (E) with (+OS) osteogenic induction. Data are represented as mean ± SD. *p<0.05, **p<0.01, ***p<0.001 and ****p<0.0001 indicate statistically significant differences of means between groups in each time point by one-way ANOVA tests.

ALP activity results revealed that DB particles significantly support ALP activity and therefore induce osteogenic differentiation as similar in ALG-MC consturcts (*Chapter 5, Figure 5.6 E*). These high levels of ALP were supported by the enhanced cell proliferation with the addition of GEL into the ALG-MC matrix and also may be associated with the inorganic content (hydroxyapatite crystals) of the DB particles, which induces osteogenic differentiation. The synergetic effect of the natural biomineralisation capacity of the DB particles (preserved by our decellularization method) and +OS induction supported osteogenicity. Thus, the differentiation studies confirmed the support of osteogenic differentiation using DB particles, which is the main focus of the project.

6.2.5. Cell Morphology inside 3D-Bioprinted ALG-GEL-MC/DB Constructs

Confocal microscopy imaging was performed to observe the cell attachment and morphology inside the 3D-bioprinted scaffolds. DAPI and F-Actin stainings were used for cell nuclei (blue) and cytoskeleton (green), respectively. In addition, DB particles are visible due to the autofluorescence property of fibrous collagen in the DB particles, which were seen as a red/pink colour. The confocal microscopy images showed the 3D stack images composed of many layers of cell-laden constructs and magnified 3D stack images taken from the inner side of the construct (Figure 6.6). Confocal microscopy images revealed the morphology and spreading of hTERT-MSCs inside the structures. The images indicate that cells grow and proliferate, interacting with DB particles and covering the entire surface of the 3D-bioprinted constructs (Figure 6.6). Attached and elongated hTERT-MSCs were observed both inside and on the surface of structures, showing the cell attachment and migration with decent cell–particle interaction throughout the surface of the 3D constructs.
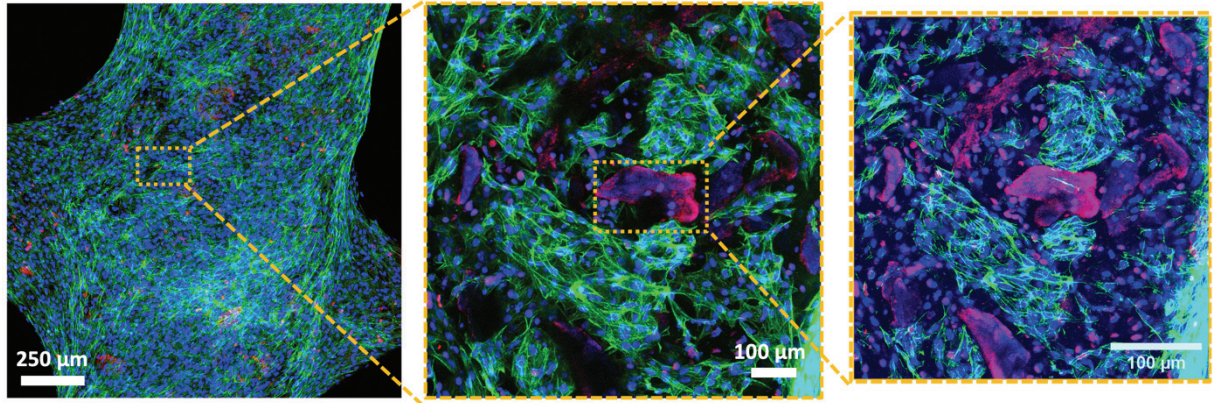
Figure 6.6. Confocal microscopy images of hTERT-MSCs attached and growing inside the 3D-bioprinted ALG-GEL-5MC/DB (1:2) constructs for 14 days of the cell culture period. Magnified images show the inner parts of the cell-laden constructs obtained. Nucleus (blue): DAPI, cytoskeleton (green): Actin 488, DB particles (red/pink): autofluorescence. Scale bars: 250 μm, 100 μm (from left to right).

6.3. Conclusions

In this chapter, ALG–GEL-MC/DB bioinks with hTERT-MSCs were prepared and successfully fabricated by 3D bioprinting. 3D-bioprinted constructs characterized in terms of their cytocompatibility and bioactivity as well as morphologically, mechanically and chemically for potential application in bone-tissue engineering.

Rheological characterization of the hydrogel precursors showed that all prepared biomaterial inks, both with and without DB particles, exhibited a shear-thinning behaviour indicating all inks have printability capacity (Figure 6.1 A). ALG-GEL-MC/DB composite hydrogels were fabricated in a circular shape with ideal, square pore geometry (Figure 6.2 A). The Pr factor, U factor of the 3D-printed hydrogels have similar Pr factor and uniformity (Figures 6.2 B and C). In addition, the pore sizes in all groups are suitable for cell attachment, proliferation and nutrient's diffusion in bone tissue engineering applications.

Beside the noncytotoxicity of the 3D-bioprinted constructs (Figure 6.5 A), higher cell viability was observed in all groups during the 28 days of the culture period (Figure 6.4). In addition, attached hTERT-MSCs formed clusters, especially in 1:2/DB constructs, on day one and then spread inside the 3D-bioprinted constructs (Figure 6.4).

hTERT-MSCs started to elongate in the constructs, especially in the 2:1/5DB scaffolds on day 14 (Figure 6.4). Moreover, confocal images revealed that cells elongated on DB particles inside the structures, exhibiting a well interaction with both material and DB particles (Figure 6.6). The cells exhibited increasing proliferation trend with the addition of the GEL and higher cell proliferation was determined on day 28 (Figure 6.5 B). The ALP activity of the cells inside the DB-incorporated ALG-GEL-MC constructs was higher than in the groups without DB particles throughout the 28 days (Figure 6.5 E). The GEL addition enhanced the proliferation and DB incorporateion into structure induced osteogenic differentiation (Figure 6.5 E).

In conclusion, with the higher printability and shape fidelity of ALG-MC biomaterial ink, the addition of GEL into the ALG-MC matrix improved the biological activity of hTERT-MSCs and incorporation of DB particles induced the osteogenic differentiation. Thus, a composite bioink formulation with higher cell response and suitable shape fidelity was developed by using biocaompatible GEL and bioactive DB particles, which could be a promising candidate for 3D biofabrication applications.

CHAPTER 7

OVERALL CONCLUSIONS

In this thesis study, the main goals are the development of a decellularization method for bone tissue and the preparation of different bioinks containing decellularized bone (DB) particles with the biofabrication of cell-laden constructs by 3D bioprinting method. For this purpose, rabbit, rat and bovine femur bone tissues were decellularized without altering the biochemical and biomechanical properties while removing cellular components from the tissue. DB particles were obtained in 100 μm and 45 μm sizes and used as a natural additive material for preparation of different bioink compositions. This thesis study demonstrated the successful production of DB particles incorporating gelatin (GEL)-, alginate (ALG)- and alginate-gelatin (ALG-GEL)-based bioinks, and fabrication of cell-laden composite constructs produced by the 3D-bioprinting technique. The addition of the DB particles was evaluated with comprehensive studies such as printability capacity of all prepared inks, the physicochemical and mechanical properties of the hydrogels and the biological behaviour of the MSCs inside the 3D-bioprinted structures, as well as the differentiation capacity of the cells for bone-tissue engineering applications.

A combination of physical, chemical and enzymatic methods was used for the decellularization of femur bones obtained from bovine, rat and rabbit. As described in *Chapter 3*, three different SDS concentrations were used for the chemical decellularization method, and 0.1% SDS was chosen as an optimum concentration to remove cellular components from tissue without damaging the ECM proteins, such as collagen and GAG. According to the literature, 0.1% SDS is the minimum concentration for bone-tissue decellularization[18,88,147]. ~95% DNA reduction was achieved with 0.1% SDS treatment, indicating effective decellularization[75]. In addition, it was also showen that the mineralisation site of the tissue remained the same, unlike various studies in the literature[18,147].

Following the verification of the decellularization method, bone particles were used to produce several bioink formulations. *Chapter 4* presented the incorporation of rabbit DB particles into the GEL matrix at 1%, 3% and 5% DB particle (100 μm) concentrations and the successful fabrication of 3D-printed GEL/DB composite

scaffolds with uniform strands and square pore morphology (Figure 4.3). SEM analysis showed good particle–polymer interaction (Figure 4.4 C), and μCT analysis showed homogenous distribution of the DB particles within the GEL matrix (Figure 4.5). While the printability data indicate that the 100 μm size of DB particle concentrations >5% mitigates printability, *in vitro* experiments highlighted that particle concentrations of 5%, with high printability properties, showed no cytotoxic effects but provide a suitable microenvironment for cell proliferation and effective cell–material and cell–particle interaction (Figures 4.9 and 4.10). Obtaining a similar approach to our study, Nyberg et al. demonstrated a comparison of DB ECM (40 μm diameter) with commercially available additives in 3D-printed poly-ε-caprolactone (PCL) scaffolds, and cell-proliferation and osteogenic-marker expressions in the DB-addition groups were higher than in other groups[147]. With the successful fabrication of the GEL/DB scaffolds and promising cell response, it was considered that including a smaller size of bone particles in the GEL matrix could enhance printability and allow for higher DB particle concentrations in the bioink composition. Therefore, smaller sizes (45 μm) of bone particles were used to obtain GEL/DB bioink formulations at 5% and 10% concentrations. The smaller size (45 μm) of bovine-particles-incorporated GEL inks exhibited promising shear thinning, with suitable self-recoverability for potential application for 3D bioprinting and improved printability compared to 100 μm DB particles. In addition, the 10% particle group demonstrated the highest proliferation and osteogenic differentiation, which might result from the natural hydroxyapatite content of the particles. 3D bioprinting of the composite structures allowed for more cell–particle interactions inside the GEL matrix and increased cell proliferation during the culture period. This enhancement of cell behaviour may be caused by the collagen fibers and hydroxyapatite components preserved by the decellularization method, as shown in many studies that have included hydroxyapatite particles[173,180,200,201]. As hypotheses, the remaining natural bone histoarchitecture by our decellularization method promoted cell behaviour within a highly biocompatible GEL matrix, and DB-incorporating biomaterial inks exhibited promising features for 3D-printing applications.

Alginate (ALG)-based bioinks were also developed; *Chapter 5* discussed the incorporation of the DB into hydrogels. ALG, as a biodegradable polymer obtained from brown algae, is commonly used for printing or bioprinting applications. It has high

liquid-absorption capability, providing good thixotropic properties, and is easily cross-linkable with CaCl2, which allows shape fidelity after printing[184]. However, inferior mechanical properties of ALG, must be increased to obtain more stable structures. Methylcellulose (MC) is a polysaccharide-based, non-toxic, biocompatible and highly hydrophilic biopolymer that has been used as a viscosity-enhancing polymer, and as such the addition of MC could enhance viscosity of alginate hydrogels[185]. In addition, the incorporation of the decellularized bovine bone particles could enhance the mechanical properties of the hydrogels and induce osteogenic differentiation. In addition, no study in the literature has described the incorporation of DB particles into the ALG–MC bioink. With this thesis study, DB particles were incorporated into the ALG–MC ink and hTERT-MSCs were used for the bioink composition for the first time. The printability of the ALG–MC bioinks was significantly higher than GEL-based bioinks, and compressive moduli were increased by the addition of the DB particles, but cell viability was decreased after 14 days of the culture period. Similar results also reported by Liu et al., which demonstrated the cell behaviour inside the ALG–MC bioinks and enhanced the biological activity using egg white powder within ALG–MC blends[193]. In this thesis study, the addition of DB particles to the ALG–MC improved cell viability and proliferation. Besides the nontoxicity effect of the bioinks on cells, the addition of DB particles supported cell adhesion, proliferation and osteogenic differentiation. The data are in correlation with previously reported study that described a positive effect of inorganic bioglass additives into ALG–MC blends on hMSC cell proliferation within 3D-bioprinted scaffolds[202].

Since cell viability decreased after 14 days in ALG–MC scaffolds, the addition of the GEL to the ALG–MC bioinks was considered due to the higher cell viability and proliferation capacity of cells inside the GEL structure, as demonstrated in *Chapter 4*. Regarding this approach, different ALG and GEL volumes were used for ALG-GEL-MC ink formulations, and DB particles were included in the structure. It was found that the addition of the GEL to ALG–MC increased the cellular activity in the hydrogel, in accordance with the previously reported studies[203–205]. Cell viability and proliferation inside the structures were enhanced when increasing the GEL content with no cytotoxic effect. In addition, DB-particle incorporation increased cell attachment, proliferation and differentiation. It was found that the cells could migrate inside the ALG-GEL-MC/DB structures with good cell–particle interaction. Moreover, the osteogenic

differentiation capacity of cells was supported by DB-incorporated ALG-GEL-MC hydrogels. In correlation with this approach, the addition of different polymer (MC or GEL) or organic/inorganic particles (DB particles composed of collagen fibers and hydroxyapatite) improved the mechanical properties of the hydrogels and supported the biologic activity of the cells inside the 3D-bioprinted structures.

In conclusion, DB-incorporated GEL-based and ALG-GEL-based bioinks provide bioprinting with MSCs and have promising results for bone-tissue engineering applications. As hypotheses, the approach of using DB particles as a natural source of collagen and hydroxyapatite in 3D-bioprinting techniques using biocompatible polymers provides good interaction with cells, which suggests the potential application of the scaffolds in bone-tissue engineering.

REFERENCES

(1)   Gaharwar, A. K.; Detamore, M. S.; Khademhosseini, A. Emerging Trends in Biomaterials Research. *Ann. Biomed. Eng.* **2016**, *44* (6), 1861–1862. https://doi.org/10.1007/s10439-016-1644-0.

(2)   Amirian, J.; Linh, N. T. B.; Min, Y. K.; Lee, B.-T. Bone Formation of a Porous Gelatin-Pectin-Biphasic Calcium Phosphate Composite in Presence of BMP-2 and VEGF. *Int. J. Biol. Macromol.* **2015**, *76*, 10–24. https://doi.org/10.1016/j.ijbiomac.2015.02.021.

(3)   Gong, T.; Xie, J.; Liao, J.; Zhang, T.; Lin, S.; Lin, Y. Nanomaterials and Bone Regeneration. *Bone Res.* **2015**, *3*, 15029. https://doi.org/10.1038/boneres.2015.29.

(4)   Yang, S. Y.; Hwang, T. H.; Che, L.; Oh, J. S.; Ha, Y.; Ryu, W. Membrane-Reinforced Three-Dimensional Electrospun Silk Fibroin Scaffolds for Bone Tissue Engineering. *Biomed. Mater.* **2015**. https://doi.org/10.1088/1748-6041/10/3/035011.

(5)   Francois, E. L., & Yaszemski, M. J. Preclinical Bone Repair Models in Regenerative Medicine. In *Principles of Regenerative Medicine. Elsevier*; Esevier, 2018; pp 761–767. https://doi.org/10.1016/B978-0-1-809880-6.00043-6.

(6)   Singelyn, J. M.; DeQuach, J. A.; Seif-Naraghi, S. B.; Littlefield, R. B.; Schup-Magoffin, P. J.; Christman, K. L. Naturally Derived Myocardial Matrix as an Injectable Scaffold for Cardiac Tissue Engineering. *Biomaterials* **2009**, *30* (29), 5409–5416. https://doi.org/10.1016/j.biomaterials.2009.06.045.

(7)   Orlando, G.; Booth, C.; Wang, Z.; Totonelli, G.; Ross, C. L.; Moran, E.; Salvatori, M.; Maghsoudlou, P.; Turmaine, M.; Delario, G.; Al-Shraideh, Y.; Farooq, U.; Farney, A. C.; Rogers, J.; Iskandar, S. S.; Burns, A.; Marini, F. C.; De Coppi, P.; Stratta, R. J.; Soker, S. Discarded Human Kidneys as a Source of ECM Scaffold for Kidney Regeneration Technologies. *Biomaterials* **2013**, *34* (24), 5915–5925. https://doi.org/10.1016/j.biomaterials.2013.04.033.

(8)   Gilpin, S. E.; Guyette, J. P.; Gonzalez, G.; Ren, X.; Asara, J. M.; Mathisen, D. J.; Vacanti, J. P.; Ott, H. C. Perfusion Decellularization of Human and Porcine Lungs: Bringing the Matrix to Clinical Scale. *J. Hear. lung Transplant. Off. Publ. Int. Soc. Hear. Transplant.* **2014**, *33* (3), 298–308. https://doi.org/10.1016/j.healun.2013.10.030.

(9)   Sánchez, P. L.; Fernández-Santos, M. E.; Costanza, S.; Climent, A. M.; Moscoso, I.; Gonzalez-Nicolas, M. A.; Sanz-Ruiz, R.; Rodríguez, H.; Kren, S. M.; Garrido, G.; Escalante, J. L.; Bermejo, J.; Elizaga, J.; Menarguez, J.; Yotti, R.; Pérez del Villar, C.; Espinosa, M. A.; Guillem, M. S.; Willerson, J. T.; Bernad, A.; Matesanz, R.; Taylor, D. A.; Fernández-Avilés, F. Acellular Human Heart Matrix: A Critical Step toward Whole Heart Grafts. *Biomaterials* **2015**, *61*, 279–289. https://doi.org/10.1016/j.biomaterials.2015.04.056.

(10) Mazza, G.; Rombouts, K.; Rennie Hall, A.; Urbani, L.; Vinh Luong, T.; Al-Akkad, W.; Longato, L.; Brown, D.; Maghsoudlou, P.; Dhillon, A. P.; Fuller, B.; Davidson, B.; Moore, K.; Dhar, D.; De Coppi, P.; Malago, M.; Pinzani, M. Decellularized Human Liver as a Natural 3D-Scaffold for Liver Bioengineering and Transplantation. *Sci. Rep.* **2015**, *5* (1), 13079. https://doi.org/10.1038/srep13079.

(11) French, K. M.; Boopathy, A. V; DeQuach, J. A.; Chingozha, L.; Lu, H.; Christman, K. L.; Davis, M. E. A Naturally Derived Cardiac Extracellular Matrix Enhances Cardiac Progenitor Cell Behavior in Vitro. *Acta Biomater.* **2012**, *8* (12), 4357–4364. https://doi.org/10.1016/j.actbio.2012.07.033.

(12) Wolf, M. T.; Daly, K. A.; Brennan-Pierce, E. P.; Johnson, S. A.; Carruthers, C. A.; D'Amore, A.; Nagarkar, S. P.; Velankar, S. S.; Badylak, S. F. A Hydrogel Derived from Decellularized Dermal Extracellular Matrix. *Biomaterials* **2012**. https://doi.org/10.1016/j.biomaterials.2012.06.051.

(13) Freytes, D. O.; Martin, J.; Velankar, S. S.; Lee, A. S.; Badylak, S. F. Preparation and Rheological Characterization of a Gel Form of the Porcine Urinary Bladder Matrix. *Biomaterials* **2008**, *29* (11), 1630–1637. https://doi.org/https://doi.org/10.1016/j.biomaterials.2007.12.014.

(14) Lee, J. S.; Shin, J.; Park, H.-M.; Kim, Y.-G.; Kim, B.-G.; Oh, J.-W.; Cho, S.-W. Liver Extracellular Matrix Providing Dual Functions of Two-Dimensional Substrate Coating and Three-Dimensional Injectable Hydrogel Platform for Liver Tissue Engineering. *Biomacromolecules* **2014**, *15* (1), 206–218. https://doi.org/10.1021/bm4015039.

(15) Quint, C.; Kondo, Y.; Manson, R. J.; Lawson, J. H.; Dardik, A.; Niklason, L. E. Decellularized Tissue-Engineered Blood Vessel as an Arterial Conduit. *Proc. Natl. Acad. Sci. U. S. A.* **2011**, *108* (22), 9214–9219. https://doi.org/10.1073/pnas.1019506108.

(16) Nguyen, M.; Do, T.; Tran, H. Fabrication of Injectable Hydrogel from Decellularized Adipose Tissue BT - 8th International Conference on the Development of Biomedical Engineering in Vietnam; Van Toi, V., Nguyen, T.-H., Long, V. B., Huong, H. T. T., Eds.; Springer International Publishing: Cham, 2022; pp 445–453.

(17) Rindone, A. N.; Nyberg, E.; Grayson, W. L. 3D-Printing Composite Polycaprolactone-Decellularized Bone Matrix Scaffolds for Bone Tissue Engineering Applications. In *Methods in Molecular Biology*; 2018. https://doi.org/10.1007/7651_2017_37.

(18) Sawkins, M. J.; Bowen, W.; Dhadda, P.; Markides, H.; Sidney, L. E.; Taylor, A. J.; Rose, F. R. A. J.; Badylak, S. F.; Shakesheff, K. M.; White, L. J. Hydrogels Derived from Demineralized and Decellularized Bone Extracellular Matrix. *Acta Biomater.* **2013**. https://doi.org/10.1016/j.actbio.2013.04.029.

(19)   Khademhosseini, A.; Langer, R. A Decade of Progress in Tissue Engineering. *Nat. Protoc.* **2016**, *11* (10), 1775–1781. https://doi.org/10.1038/nprot.2016.123.

(20)   Langer, R.; Vacanti, J. P. Tissue Engineering. *Science (80-.)*. **1993**, *260* (5110), 920–926. https://doi.org/10.1126/science.8493529.

(21)   Moysidou, C.-M.; Barberio, C.; Owens, R. M. Advances in Engineering Human Tissue Models. *Frontiers in Bioengineering and Biotechnology*. 2021. https://doi.org/10.3389/fbioe.2020.620962

(22)   Hutmacher, D. W.; Tandon, B.; Dalton, P. D. Chapter 11 - Scaffold Design and Fabrication; De Boer, J., Blitterswijk, C. A. V., Uquillas, J. A., Malik, N. B. T.-T. E. (Third E., Eds.; Academic Press, 2023; pp 355–385. https://doi.org/https://doi.org/10.1016/B978-0-12-824459-3.00011-1.

(23)   Lai, G.-J.; Shalumon, K. T.; Chen, J.-P. Response of Human Mesenchymal Stem Cells to Intrafibrillar Nanohydroxyapatite Content and Extrafibrillar Nanohydroxyapatite in Biomimetic Chitosan/Silk Fibroin/Nanohydroxyapatite Nanofibrous Membrane Scaffolds. *Int. J. Nanomedicine* **2015**, *10*, 567–584. https://doi.org/10.2147/IJN.S73780.

(24)   Schofer, M. D.; Boudriot, U.; Wack, C.; Leifeld, I.; Gräbedünkel, C.; Dersch, R.; Rudisile, M.; Wendorff, J. H.; Greiner, A.; Paletta, J. R. J.; Fuchs-Winkelmann, S. Influence of Nanofibers on the Growth and Osteogenic Differentiation of Stem Cells: A Comparison of Biological Collagen Nanofibers and Synthetic PLLA Fibers. *J. Mater. Sci. Mater. Med.* **2009**, *20* (3), 767–774. https://doi.org/10.1007/s10856-008-3634-8.

(25)   Pawlik, J.; Łukowicz, K.; Cholewa-Kowalska, K. New Insights into the PLGA and PCL Blending: Physico-Mechanical Properties and Cell Response. *Mater. Res. Express* **2019**, *6* (8), 85344. https://doi.org/10.1088/2053-1591/ab2823.

(26)   Roohani-Esfahani, S.-I.; Wong, K. Y.; Lu, Z.; Juan Chen, Y.; Li, J. J.; Gronthos, S.; Menicanin, D.; Shi, J.; Dunstan, C.; Zreiqat, H. Fabrication of a Novel Triphasic and Bioactive Ceramic and Evaluation of Its in Vitro and in Vivo Cytocompatibility and Osteogenesis. *J. Mater. Chem. B* **2014**, *2* (13), 1866–1878. https://doi.org/10.1039/C3TB21504K.

(27)   Gonçalves, F.; Bentini, R.; Burrows, M. C.; Carreira, A. C. O.; Kossugue, P. M.; Sogayar, M. C.; Catalani, L. H. Hybrid Membranes of PLLA/Collagen for Bone Tissue Engineering: A Comparative Study of Scaffold Production Techniques for Optimal Mechanical Properties and Osteoinduction Ability. *Mater. (Basel, Switzerland)* **2015**, *8* (2), 408–423. https://doi.org/10.3390/ma8020408.

(28)   Srivastava, D.; DeWitt, N. In Vivo Cellular Reprogramming: The Next Generation. *Cell* **2016**, *166* (6), 1386–1396. https://doi.org/10.1016/j.cell.2016.08.055.

(29) Ladewig, J.; Koch, P.; Brüstle, O. Leveling Waddington: The Emergence of Direct Programming and the Loss of Cell Fate Hierarchies. *Nat. Rev. Mol. Cell Biol.* **2013**, *14* (4), 225–236. https://doi.org/10.1038/nrm3543.

(30) Lutolf, M. P.; Hubbell, J. A. Synthetic Biomaterials as Instructive Extracellular Microenvironments for Morphogenesis in Tissue Engineering. *Nat. Biotechnol.* **2005**, *23* (1), 47–55. https://doi.org/10.1038/nbt1055.

(31) Zhang, Q.; He, Q.-F.; Zhang, T.-H.; Yu, X.-L.; Liu, Q.; Deng, F. Improvement in the Delivery System of Bone Morphogenetic Protein-2: A New Approach to Promote Bone Formation. *Biomed. Mater.* **2012**, *7* (4), 45002. https://doi.org/10.1088/1748-6041/7/4/045002.

(32) Feng, Q.; Li, Q.; Wen, H.; Chen, J.; Liang, M.; Huang, H.; Lan, D.; Dong, H.; Cao, X. Injection and Self-Assembly of Bioinspired Stem Cell-Laden Gelatin/Hyaluronic Acid Hybrid Microgels Promote Cartilage Repair In Vivo. *Adv. Funct. Mater.* **2019**. https://doi.org/10.1002/adfm.201906690.

(33) Caldwell, A. S.; Aguado, B. A.; Anseth, K. S. Designing Microgels for Cell Culture and Controlled Assembly of Tissue Microenvironments. *Advanced Functional Materials*. 2020. https://doi.org/10.1002/adfm.201907670.

(34) Kara, A.; Tamburaci, S.; Tihminlioglu, F.; Havitcioglu, H. Bioactive Fish Scale Incorporated Chitosan Biocomposite Scaffolds for Bone Tissue Engineering. *Int. J. Biol. Macromol.* **2019**, *130*, 266–279. https://doi.org/10.1016/j.ijbiomac.2019.02.067.

(35) Kara, A.; Gunes, O. C.; Albayrak, A. Z.; Bilici, G.; Erbil, G.; Havitcioglu, H. Fish Scale/Poly(3-Hydroxybutyrate-Co-3-Hydroxyvalerate) Nanofibrous Composite Scaffolds for Bone Regeneration. *J. Biomater. Appl.* **2020**, *34* (9), 1201–1215. https://doi.org/10.1177/0885328220901987.

(36) Xue, J.; Wu, T.; Dai, Y.; Xia, Y. Electrospinning and Electrospun Nanofibers: Methods, Materials, and Applications. *Chem. Rev.* **2019**, *119* (8), 5298–5415. https://doi.org/10.1021/acs.chemrev.8b00593.

(37) Bishop, E. S.; Mostafa, S.; Pakvasa, M.; Luu, H. H.; Lee, M. J.; Wolf, J. M.; Ameer, G. A.; He, T. C.; Reid, R. R. 3-D Bioprinting Technologies in Tissue Engineering and Regenerative Medicine: Current and Future Trends. *Genes and Diseases*. 2017. https://doi.org/10.1016/j.gendis.2017.10.002.

(38) Li, J.; Wu, C.; Chu, P. K.; Gelinsky, M. 3D Printing of Hydrogels: Rational Design Strategies and Emerging Biomedical Applications. *Materials Science and Engineering R: Reports*. 2020. https://doi.org/10.1016/j.mser.2020.100543.

(39) Peloso, A.; Dhal, A.; Zambon, J. P.; Li, P.; Orlando, G.; Atala, A.; Soker, S. Current Achievements and Future Perspectives in Whole-Organ Bioengineering. *Stem Cell Res. Ther.* **2015**, *6* (1), 107. https://doi.org/10.1186/s13287-015-089-y.

(40) Uhl, F. E.; Zhang, F.; Pouliot, R. A.; Uriarte, J. J.; Rolandsson Enes, S.; Han, X.; Ouyang, Y.; Xia, K.; Westergren-Thorsson, G.; Malmström, A.; Hallgren, O.; Linhardt, R. J.; Weiss, D. J. Functional Role of Glycosaminoglycans in Decellularized Lung Extracellular Matrix. *Acta Biomater.* **2020**, *102*, 231–246. https://doi.org/10.1016/j.actbio.2019.11.029.

(41) Kara, A.; Koçtürk, S.; Bilici, G.; Havitcioglu, H. Development of Biological Meniscus Scaffold: Decellularization Method and Recellularization with Meniscal Cell Population Derived from Mesenchymal Stem Cells. *J. Biomater. Appl.* **2021**. https://doi.org/10.1177/0885328220981189.

(42) Zhang, X.; Chen, X.; Hong, H.; Hu, R.; Liu, J.; Liu, C. Decellularized Extracellular Matrix Scaffolds: Recent Trends and Emerging Strategies in Tissue Engineering. *Bioact. Mater.* **2022**, *10*, 15–31. https://doi.org/10.1016/j.bioactmat.2021.09.014.

(43) Papadimitropoulos, A.; Scotti, C.; Bourgine, P.; Scherberich, A.; Martin, I. Engineered Decellularized Matrices to Instruct Bone Regeneration Processes. *Bone*. 2015. https://doi.org/10.1016/j.bone.2014.09.007.

(44) Schubert, T.; Lafont, S.; Beaurin, G.; Grisay, G.; Behets, C.; Gianello, P.; Dufrane, D. Critical Size Bone Defect Reconstruction by an Autologous 3D Osteogenic-like Tissue Derived from Differentiated Adipose MSCs. *Biomaterials* **2013**. https://doi.org/10.1016/j.biomaterials.2013.02.053.

(45) Bose, S.; Roy, M.; Bandyopadhyay, A. Recent Advances in Bone Tissue Engineering Scaffolds. *Trends in Biotechnology*. 2012. https://doi.org/10.1016/j.tibtech.2012.07.005.

(46) Amini, A. R.; Laurencin, C. T.; Nukavarapu, S. P. Bone Tissue Engineering: Recent Advances and Challenges. *Crit. Rev. Biomed. Eng.* **2012**, *40* (5), 363–408. https://doi.org/10.1615/CritRevBiomedEng.v40.i5.10.

(47) Zhu, G.; Zhang, T.; Chen, M.; Yao, K.; Huang, X.; Zhang, B.; Li, Y.; Wang, Y.; Zhao, Z. Bone Physiological Microenvironment and Healing Mechanism: Basis for Future Bone-Tissue Engineering Scaffolds. *Bioact. Mater.* **2021**,*6*(11),4110–4140. https://doi.org/https://doi.org/10.1016/j.bioactmat.2021.03.043.

(48) Kattimani, V. S.; Kondaka, S.; Lingamaneni, K. P. Hydroxyapatite–-Past, Present, and Future in Bone Regeneration. *Bone Tissue Regen. Insights* **2016**, *7*, BTRI.S36138. https://doi.org/10.4137/BTRI.S36138.

(49) Rho, J.-Y.; Kuhn-Spearing, L.; Zioupos, P. Mechanical Properties and the Hierarchical Structure of Bone. *Med. Eng. Phys.* **1998**, *20* (2), 92–102. https://doi.org/https://doi.org/10.1016/S1350-4533(98)00007-1.

(50) Kim, T.; See, C. W.; Li, X.; Zhu, D. Orthopedic Implants and Devices for Bone Fractures and Defects: Past, Present and Perspective. *Eng. Regen.* **2020**, *1*, 6–18. https://doi.org/https://doi.org/10.1016/j.engreg.2020.05.003.

(51)   Oryan, A.; Kamali, A.; Moshirib, A.; Eslaminejad, M. B. Role of Mesenchymal Stem Cells in Bone Regenerative Medicine: What Is the Evidence? *Cells Tissues Organs.* 2017. https://doi.org/10.1159/000469704.

(52)   Tonelli, P.; Duvina, M.; Barbato, L.; Biondi, E.; Nuti, N.; Brancato, L.; Rose, G. D. Bone Regeneration in Dentistry. *Clin. cases Miner. bone Metab. Off. J. Ital. Soc. Osteoporosis, Miner. Metab. Skelet. Dis.* **2011**, *8* (3), 24–28.

(53)   Henkel, J.; Woodruff, M. A.; Epari, D. R.; Steck, R.; Glatt, V.; Dickinson, I. C.; Choong, P. F. M.; Schuetz, M. A.; Hutmacher, D. W. Bone Regeneration Based on Tissue Engineering Conceptions — A 21st Century Perspective. *Bone Res.* **2013**, *1* (1), 216–248. https://doi.org/10.4248/BR201303002.

(54)   Karageorgiou, V.; Kaplan, D. Porosity of 3D Biomaterial Scaffolds and Osteogenesis. *Biomaterials* **2005**, *26* (27), 5474–5491. https://doi.org/10.1016/j.biomaterials.2005.02.002.

(55)   Sola, A.; Bertacchini, J.; D'Avella, D.; Anselmi, L.; Maraldi, T.; Marmiroli, S.; Messori, M. Development of Solvent-Casting Particulate Leaching (SCPL) Polymer Scaffolds as Improved Three-Dimensional Supports to Mimic the Bone Marrow Niche. *Mater. Sci. Eng. C* **2019**, *96*, 153–165. https://doi.org/https://doi.org/10.1016/j.msec.2018.10.086.

(56)   Bartis, D.; Pongracz, J. *Three Dimensional Tissue Cultures and Tissue Engineering*; 2011. https://doi.org/10.13140/2.1.2793.5047.

(57)   Mao, D.; Li, Q.; Li, D.; Tan, Y.; Che, Q. 3D Porous Poly(ε-Caprolactone)/58S Bioactive Glass–Sodium Alginate/Gelatin Hybrid Scaffolds Prepared by a Modified Melt Molding Method for Bone Tissue Engineering. *Mater. Des.* **2018**, *160*, 1–8. https://doi.org/https://doi.org/10.1016/j.matdes.2018.08.062.

(58)   Liao, X.; Zhang, H.; He, T. Preparation of Porous Biodegradable Polymer and Its Nanocomposites by Supercritical CO_2 Foaming for Tissue Engineering. *J. Nanomater.* **2012**, *2012*, 836394. https://doi.org/10.1155/2012/836394.

(59)   Martinez Perez, C.; Olivas-Armendariz, I.; Castro-Carmona, J.; Garcia Casillas, P. E. Scaffolds for Tissue Engineering Via Thermally Induced Phase Separation; 2011. https://doi.org/10.5772/1294.

(60)   Cecen, B.; Kozaci, L. D.; YuksEL, M.; Kara, A.; Ersoy, N. Two Layered Scaffolds (Loofah/PLLA/Cellulose/Chitin) for Repair of Osteochondral Defect. *J. Tissue Sci. Eng.* **2018**, *08* (03). https://doi.org/10.4172/2157-7552.1000210.

(61)   Zheng, K.; Sui, B.; Ilyas, K.; Boccaccini, A. R. Porous Bioactive Glass Micro- and Nanospheres with Controlled Morphology: Developments{,} Properties and Emerging Biomedical Applications. *Mater. Horiz.* **2021**, *8* (2), 300–335. https://doi.org/10.1039/D0MH01498B.

(62)   Mohammadi Zerankeshi, M.; Mofakhami, S.; Salahinejad, E. 3D Porous HA/TCP Composite Scaffolds for Bone Tissue Engineering. *Ceram. Int.* **2022**, *48* (16), 22647–22663. https://doi.org/10.1016/j.ceramint.2022.05.103.

(63) Mabrouk, M.; Beherei, H. H.; Das, D. B. Recent Progress in the Fabrication Techniques of 3D Scaffolds for Tissue Engineering. *Mater. Sci. Eng. C. Mater. Biol. Appl.* **2020**, *110*, 110716. https://doi.org/10.1016/j.msec.2020.110716.

(64) Sill, T. J.; von Recum, H. A. Electrospinning: Applications in Drug Delivery and Tissue Engineering. *Biomaterials* **2008**, *29* (13), 1989–2006. https://doi.org/10.1016/j.biomaterials.2008.01.011.

(65) Jin, G.; He, R.; Sha, B.; Li, W.; Qing, H.; Teng, R.; Xu, F. Electrospun Three-Dimensional Aligned Nanofibrous Scaffolds for Tissue Engineering. *Mater. Sci. Eng. C* **2018**, *92*, 995–1005. https://doi.org/https://doi.org/10.1016/j.msec.2018.06.065.

(66) Amiryaghoubi, N.; Fathi, M.; Barar, J.; Omidi, Y. Hydrogel-Based Scaffolds for Bone and Cartilage Tissue Engineering and Regeneration. *React. Funct. Polym.* **2022**, *177*, 105313. https://doi.org/https://doi.org/10.1016/j.reactfunctpolym.2022.105313.

(67) Badylak, S. F.; Freytes, D. O.; Gilbert, T. W. Reprint of: Extracellular Matrix as a Biological Scaffold Material: Structure and Function. *Acta Biomaterialia*. 2015. https://doi.org/10.1016/j.actbio.2015.07.016.

(68) Gupta, K.; Meena, K. Artificial Bone Scaffolds and Bone Joints by Additive Manufacturing: A Review. *Bioprinting* **2023**, *31*, e00268. https://doi.org/https://doi.org/10.1016/j.bprint.2023.e00268.

(69) Gilbert, T. W.; Sellaro, T. L.; Badylak, S. F. Decellularization of Tissues and Organs. *Biomaterials*. 2006. https://doi.org/10.1016/j.biomaterials.2006.02.014.

(70) Badylak, S. F.; Taylor, D.; Uygun, K. Whole-Organ Tissue Engineering : Decellularization and Recellularization of Matrix Scaffolds. *Annu. Rev. Biomed. Eng.* **2011**. https://doi.org/10.1146/annurev-bioeng-071910-124743.

(71) Rabbani, M.; Zakian, N.; Alimoradi, N. Contribution of Physical Methods in Decellularization of Animal Tissues. *J. Med. Signals Sens.* **2021**, *11* (1), 1–11. https://doi.org/10.4103/jmss.JMSS_2_20.

(72) Naal, F. D.; Schauwecker, J.; Steinhauser, E.; Milz, S.; Von Knoch, F.; Mittelmeier, W.; Diehl, P. Biomechanical and Immunohistochemical Properties of Meniscal Cartilage after High Hydrostatic Pressure Treatment. *J. Biomed. Mater. Res. - Part B Appl. Biomater.* **2008**. https://doi.org/10.1002/jbm.b.31059.

(73) Xu, H.; Xu, B.; Yang, Q.; Li, X.; Ma, X.; Xia, Q.; Zhang, Y.; Zhang, C.; Wu, Y.; Zhang, Y. Comparison of Decellularization Protocols for Preparing a Decellularized Porcine Annulus Fibrosus Scaffold. *PLoS One* **2014**. https://doi.org/10.1371/journal.pone.0086723.

(74) Petersen, T. H.; Calle, E. A.; Colehour, M. B.; Niklason, L. E. Matrix Composition and Mechanics of Decellularized Lung Scaffolds. *Cells Tissues Organs* **2012**. https://doi.org/10.1159/000324896.

(75)   Crapo, P. M.; Gilbert, T. W.; Badylak, S. F. An Overview of Tissue and Whole Organ Decellularization Processes. *Biomaterials*. 2011. https://doi.org/10.1016/j.biomaterials.2011.01.057.

(76)   Lee, D. J.; Diachina, S.; Lee, Y. T.; Zhao, L.; Zou, R.; Tang, N.; Han, H.; Chen, X.; Ko, C. C. Decellularized Bone Matrix Grafts for Calvaria Regeneration. *J. Tissue Eng.* **2016**. https://doi.org/10.1177/2041731416680306.

(77)   Reing, J. E.; Brown, B. N.; Daly, K. A.; Freund, J. M.; Gilbert, T. W.; Hsiong, S. X.; Huber, A.; Kullas, K. E.; Tottey, S.; Wolf, M. T.; Badylak, S. F. The Effects of Processing Methods upon Mechanical and Biologic Properties of Porcine Dermal Extracellular Matrix Scaffolds. *Biomaterials* **2010**, *31* (33), 8626–8633. https://doi.org/10.1016/j.biomaterials.2010.07.083.

(78)   Cox, B.; Emili, A. Tissue Subcellular Fractionation and Protein Extraction for Use in Mass-Spectrometry-Based Proteomics. *Nat. Protoc.* **2006**, *1* (4), 1872–1878. https://doi.org/10.1038/nprot.2006.273.

(79)   Yang, M.; Chen, C.-Z.; Wang, X.-N.; Zhu, Y.-B.; Gu, Y. J. Favorable Effects of the Detergent and Enzyme Extraction Method for Preparing Decellularized Bovine Pericardium Scaffold for Tissue Engineered Heart Valves. *J. Biomed. Mater. Res. B. Appl. Biomater.* **2009**, *91* (1), 354–361. https://doi.org/10.1002/jbm.b.31409.

(80)   Stapleton, T. W.; Ingram, J.; Katta, J.; Knight, R.; Korossis, S.; Fisher, J.; Ingham, E. Development and Characterization of an Acellular Porcine Medial Meniscus for Use in Tissue Engineering. *Tissue Eng. - Part A.* **2008**. https://doi.org/10.1089/tea.2007.0233.

(81)   Deeken, C. R.; White, A. K.; Bachman, S. L.; Ramshaw, B. J.; Cleveland, D. S.; Loy, T. S.; Grant, S. A. Method of Preparing a Decellularized Porcine Tendon Using Tributyl Phosphate. *J. Biomed. Mater. Res. - Part B Appl. Biomater.* **2011**. https://doi.org/10.1002/jbm.b.31753.

(82)   Fazelian-Dehkordi, K. H.; Mesbah Ardekani, S. F.; Talaei-Khozani, T. Quality Comparison of Decellularized Omentum Prepared by Different Protocols for Tissue Engineering Applications. *Cell J.* **2022**, *24* (5), 267–276. https://doi.org/10.22074/cellj.2022.7968.

(83)   Badylak, S. F.; Kropp, B.; McPherson, T.; Liang, H.; Snyder, P. W. Small Intestinal Submucosa: A Rapidly Resorbed Bioscaffold for Augmentation Cystoplasty in a Dog Model. *Tissue Eng.* **2007**. https://doi.org/10.1089/ten.1998.4.379.

(84)   Kao, C.-Y.; Nguyen, H.-Q.-D.; Weng, Y.-C. Characterization of Porcine Urinary Bladder Matrix Hydrogels from Sodium Dodecyl Sulfate Decellularization Method. *Polymers (Basel).* **2020**, *12* (12). https://doi.org/10.3390/polym12123007.

(85) Verstegen, M. M. A.; Willemse, J.; Van Den Hoek, S.; Kremers, G. J.; Luider, T. M.; Van Huizen, N. A.; Willemssen, F. E. J. A.; Metselaar, H. J.; Ijzermans, J. N. M.; Van Der Laan, L. J. W.; De Jonge, J. Decellularization of Whole Human Liver Grafts Using Controlled Perfusion for Transplantable Organ Bioscaffolds. *Stem Cells Dev.* **2017**. https://doi.org/10.1089/scd.2017.0095.

(86) Kumar, N.; Kumar, V.; Purohit, S.; Gangwar, A. K.; Shrivastava, S.; Maiti, S. K.; Saxena, S.; Mathews, D. D.; Raghuvanshi, P. D. S.; Singh, A. K.; Singh, K. P. Decellularization of Skin Tissue. *Adv. Exp. Med. Biol.* **2021**, *1345*, 165–191. https://doi.org/10.1007/978-3-030-82735-9_15.

(87) Kara, A. Development of Meniscus Tissue Bio-Compatibility Using Allograft Native Scaffold, Dokuz Eylül Universiy, Master thesis. 2017.

(88) Paduano, F.; Marrelli, M.; Alom, N.; Amer, M.; White, L. J.; Shakesheff, K. M.; Tatullo, M. Decellularized Bone Extracellular Matrix and Human Dental Pulp Stem Cells as a Construct for Bone Regeneration. *J. Biomater. Sci. Polym. Ed.* **2017**. https://doi.org/10.1080/09205063.2017.1301770.

(89) Abedin, E.; Lari, R.; Mahdavi Shahri, N.; Fereidoni, M. Development of a Demineralized and Decellularized Human Epiphyseal Bone Scaffold for Tissue Engineering: A Histological Study. *Tissue Cell* **2018**. https://doi.org/10.1016/j.tice.2018.09.003.

(90) Chen, J.; Burger, C.; Krishnan, C. V; Chu, B.; Hsiao, B. S.; Glimcher, M. J. In Vitro Mineralization of Collagen in Demineralized Fish Bone. *Macromol. Chem. Phys.* **2005**, *206* (1), 43–51. https://doi.org/https://doi.org/10.1002/macp.200400066.

(91) Teixeira, L. S. M.; Bijl, S.; Pully, V. V; Otto, C.; Jin, R.; Feijen, J.; van Blitterswijk, C. A.; Dijkstra, P. J.; Karperien, M. Self-Attaching and Cell-Attracting in-Situ Forming Dextran-Tyramine Conjugates Hydrogels for Arthroscopic Cartilage Repair. *Biomaterials* **2012**, *33* (11), 3164–3174. https://doi.org/10.1016/j.biomaterials.2012.01.001

(92) Øvrebø, Ø.; Perale, G.; Wojciechowski, J. P.; Echalier, C.; Jeffers, J. R. T.; Stevens, M. M.; Haugen, H. J.; Rossi, F. Design and Clinical Application of Injectable Hydrogels for Musculoskeletal Therapy. *Bioeng. Transl. Med.* **2022**, *7* (2), e10295. https://doi.org/10.1002/btm2.10295

(93) Pu, W.; Han, Y.; Yang, M. Human Decellularized Adipose Tissue Hydrogels as a Culture Platform for Human Adipose-Derived Stem Cell Delivery. *J. Appl. Biomater. Funct. Mater.* **2021**, *19*, 2280800020988141. https://doi.org/10.1177/2280800020988141.

(94) M., S. J.; Priya, S.; D., J. T.; J., S.-M. P.; P., H. D.; M., F. D.; Jean, W.; Nabil, D.; L., C. K. Catheter-Deliverable Hydrogel Derived From Decellularized Ventricular Extracellular Matrix Increases Endogenous Cardiomyocytes and Preserves Cardiac Function Post-Myocardial Infarction. *J. Am. Coll. Cardiol.* **2012**, *59* (8), 751–763. https://doi.org/10.1016/j.jacc.2011.10.888.

(95)   Pati, F.; Ha, D.-H.; Jang, J.; Han, H. H.; Rhie, J.-W.; Cho, D.-W. Biomimetic 3D Tissue Printing for Soft Tissue Regeneration. *Biomaterials* **2015**, *62*, 164–175. https://doi.org/10.1016/j.biomaterials.2015.05.043.

(96)   Mandrycky, C.; Wang, Z.; Kim, K.; Kim, D. H. 3D Bioprinting for Engineering Complex Tissues. *Biotechnology Advances*. 2016. https://doi.org/10.1016/j.biotechadv.2015.12.011.

(97)   Groll, J.; Yoo, J. J. Special Issue on Bioinks. *Biofabrication*. 2019. https://doi.org/10.1088/1758-5090/aaeebc.

(98)   Murphy, S. V.; Atala, A. 3D Bioprinting of Tissues and Organs. *Nat. Biotechnol.* **2014**, *32*, 773–785. https://doi.org/10.1038/nbt.2958.

(99)   Groll, J.; Boland, T.; Blunk, T.; Burdick, J. A.; Cho, D. W.; Dalton, P. D.; Derby, B.; Forgacs, G.; Li, Q.; Mironov, V. A.; Moroni, L.; Nakamura, M.; Shu, W.; Takeuchi, S.; Vozzi, G.; Woodfield, T. B. F.; Xu, T.; Yoo, J. J.; Malda, J. Biofabrication: Reappraising the Definition of an Evolving Field. *Biofabrication* **2016**, *8* (1), 013001. https://doi.org/10.1088/1758-5090/8/1/013001.

(100) Park, J. B. The Use of Hydrogels in Bone-Tissue Engineering. *Medicina Oral, Patologia Oral y Cirugia Bucal*. 2011. https://doi.org/10.4317/medoral.16.e115.

(101) Fernandes-Cunha, G. M.; Chen, K. M.; Chen, F.; Le, P.; Han, J. H.; Mahajan, L. A.; Lee, H. J.; Na, K. S.; Myung, D. In Situ-Forming Collagen Hydrogel Crosslinked via Multi-Functional PEG as a Matrix Therapy for Corneal Defects. *Sci. Rep.* **2020**, *10* (1), 16671. https://doi.org/10.1038/s41598-020-72978-5.

(102) Rastin, H.; Ormsby, R. T.; Atkins, G. J.; Losic, D. 3D Bioprinting of Methylcellulose/Gelatin-Methacryloyl (MC/GelMA) Bioink with High Shape Integrity. *ACS Appl. Bio Mater.* **2020**, *3* (3), 1815–1826. https://doi.org/10.1021/acsabm.0c00169.

(103) Kibungu, C.; Kondiah, P. P. D.; Kumar, P.; Choonara, Y. E. Recent Advances in Chitosan and Alginate-Based Hydrogels for Wound Healing Application. *Frontiers in Materials*. 2021. https://doi.org/10.3389/fmats.2021.681960.

(104) Burdick, J. A.; Prestwich, G. D. Hyaluronic Acid Hydrogels for Biomedical Applications. *Adv. Mater.* **2011**, *23* (12), H41–H56. https://doi.org/https://doi.org/10.1002/adma.201003963.

(105) Singh, R.; Sarker, B.; Silva, R.; Detsch, R.; Dietel, B.; Alexiou, C.; Boccaccini, A. R.; Cicha, I. Evaluation of Hydrogel Matrices for Vessel Bioplotting: Vascular Cell Growth and Viability. *J. Biomed. Mater. Res. - Part A* **2016**, *104* (3), 577–585. https://doi.org/10.1002/jbm.a.35590.

(106) Zhang, L.; Yang, G.; Johnson, B. N.; Jia, X. Three-Dimensional (3D) Printed Scaffold and Material Selection for Bone Repair. *Acta Biomater.* **2019**, *84*, 16–33. https://doi.org/https://doi.org/10.1016/j.actbio.2018.11.039.

(107) Levato, R.; Visser, J.; Planell, J. A.; Engel, E.; Malda, J.; Mateos-Timoneda, M. A. Biofabrication of Tissue Constructs by 3D Bioprinting of Cell-Laden Microcarriers. *Biofabrication* **2014**, *6* (3), 35020. https://doi.org/10.1088/1758-5082/6/3/035020.

(108) Malda, J.; Visser, J.; Melchels, F. P.; Jüngst, T.; Hennink, W. E.; Dhert, W. J. A.; Groll, J.; Hutmacher, D. W. 25th Anniversary Article: Engineering Hydrogels for Biofabrication. *Adv. Mater.* **2013**, *25*, 5011–5028. https://doi.org/10.1002/adma.201302042.

(109) Bose, S.; Vahabzadeh, S.; Bandyopadhyay, A. Bone Tissue Engineering Using 3D Printing. *Materials Today*. 2013. https://doi.org/10.1016/j.mattod.2013.11.017.

(110) Ren, T.; van der Merwe, Y.; Steketee, M. B. Developing Extracellular Matrix Technology to Treat Retinal or Optic Nerve Injury(1,2,3). *eNeuro* **2015**, *2* (5). https://doi.org/10.1523/ENEURO.0077-15.2015.

(111) Saldin, L. T.; Cramer, M. C.; Velankar, S. S.; White, L. J.; Badylak, S. F. Extracellular Matrix Hydrogels from Decellularized Tissues: Structure and Function. *Acta Biomater.* **2017**, *49*, 1–15. https://doi.org/https://doi.org/10.1016/j.actbio.2016.11.068.

(112) Badylak, S. F.; Gilbert., T. W. Extra Cellular Matrix as a Biological Scaffold Material Structure and Function. *Acta Biomater.* **2009**. https://doi.org/10.1016/j.actbio.2008.09.013

(113) Faulk, D. M.; Badylak, S. F. Natural Biomaterials for Regenerative Medicine Applications. In *Regenerative Medicine Applications in Organ Transplantation*; 2014. https://doi.org/10.1016/B978-0-12-398523-1.00008-2.

(114) Pati, F.; Jang, J.; Ha, D.-H.; Won Kim, S.; Rhie, J.-W.; Shim, J.-H.; Kim, D.-H.; Cho, D.-W. Printing Three-Dimensional Tissue Analogues with Decellularized Extracellular Matrix Bioink. *Nat. Commun.* **2014**, *5*, 3935. https://doi.org/10.1038/ncomms4935.

(115) Liliang, O.; Rui, Y.; Yu, Z.; Wei, S. Effect of Bioink Properties on Printability and Cell Viability for 3D Bioplotting of Embryonic Stem Cells. *Biofabrication* **2016**, *8*, 035020. https://doi.org/ 10.1088/1758-5090/8/3/035020

(116) Soltan, N.; Ning, L.; Mohabatpour, F.; Papagerakis, P.; Chen, X. Printability and Cell Viability in Bioprinting Alginate Dialdehyde-Gelatin Scaffolds. *ACS Biomater. Sci. Eng.* **2019**, *5* (6), 2976–2987. https://doi.org/10.1021/acsbiomaterials.9b00167.

(117) Chen, G.; Lv, Y. Decellularized Bone Matrix Scaffold for Bone Regeneration BT - Decellularized Scaffolds and Organogenesis: Methods and Protocols; Turksen, K., Ed.; Springer New York: New York, NY, 2018; pp 239–254. https://doi.org/10.1007/7651_2017_50.

(118) Li, M.; Fu, X.; Gao, H.; Ji, Y.; Li, J.; Wang, Y. Regulation of an Osteon-like Concentric Microgrooved Surface on Osteogenesis and Osteoclastogenesis. *Biomaterials* **2019**. https://doi.org/10.1016/j.biomaterials.2019.119269.

(119) Laker, L.; Dohmen, P. M.; Smit, F. E. Synergy in a Detergent Combination Results in Superior Decellularized Bovine Pericardial Extracellular Matrix Scaffolds. *J. Biomed. Mater. Res. - Part B Appl. Biomater.* **2020**. https://doi.org/10.1002/jbm.b.34588.

(120) Smith, C. A.; Richardson, S. M.; Eagle, M. J.; Rooney, P.; Board, T.; Hoyland, J. A. The Use of a Novel Bone Allograft Wash Process to Generate a Biocompatible, Mechanically Stable and Osteoinductive Biological Scaffold for Use in Bone Tissue Engineering. *J. Tissue Eng. Regen. Med.* **2015**. https://doi.org/10.1002/term.1934.

(121) Safdari, M.; Bibak, B.; Soltani, H.; Hashemi, J. Recent Advancements in Decellularized Matrix Technology for Bone Tissue Engineering. *Differentiation*. 2021. https://doi.org/10.1016/j.diff.2021.08.004.

(122) Kim, Y. S.; Majid, M.; Melchiorri, A. J.; Mikos, A. G. Applications of Decellularized Extracellular Matrix in Bone and Cartilage Tissue Engineering. *Bioeng. Transl. Med.* **2019**. https://doi.org/10.1002/btm2.10110.

(123) Mendoza-Novelo, B.; Avila, E. E.; Cauich-Rodríguez, J. V.; Jorge-Herrero, E.; Rojo, F. J.; Guinea, G. V.; Mata-Mata, J. L. Decellularization of Pericardial Tissue and Its Impact on Tensile Viscoelasticity and Glycosaminoglycan Content. *Acta Biomater.* **2011**. https://doi.org/10.1016/j.actbio.2010.11.017.

(124) Hua, R.; Ni, Q.; Eliason, T. D.; Han, Y.; Gu, S.; Nicolella, D. P.; Wang, X.; Jiang, J. X. Biglycan and Chondroitin Sulfate Play Pivotal Roles in Bone Toughness via Retaining Bound Water in Bone Mineral Matrix. *Matrix Biol.* **2020**, *94*, 95–109. https://doi.org/https://doi.org/10.1016/j.matbio.2020.09.002.

(125) Haiwei Xu , Baoshan Xu , Qiang Yang , Xiulan Li, Xinlong Ma, Qun Xia, Yang Zhang, Chunqiu Zhang, Yaohong Wu, Y. Z. Comparison of Decellularization Protocols for Preparing a Decellularized Porcine Annulus Fibrosus Scaffold. *PLoS One* **2014**, *9* (1). https://doi.org/10.1371/journal.pone.0086723.

(126) Groll, J.; Burdick, J. A.; Cho, D.-W.; Derby, B.; Gelinsky, M.; Heilshorn, S. C.; Jüngst, T.; Malda, J.; Mironov, V. A.; Nakayama, K.; Ovsianikov, A.; Sun, W.; Takeuchi, S.; Yoo, J. J.; Woodfield, T. B. F. A Definition of Bioinks and Their Distinction from Biomaterial Inks. *Biofabrication* **2019**, *11* (1), 13001. https://doi.org/10.1088/1758-5090/aaec52.

(127) Giorleo, L.; Tegazzini, F.; Sartore, L. 3D Printing of Gelatin/Chitosan Biodegradable Hybrid Hydrogel: Critical Issues Due to the Crosslinking Reaction, Degradation Phenomena and Process Parameters. *Bioprinting* **2021**. https://doi.org/10.1016/j.bprint.2021.e00170.

(128) Allen, N. B.; Abar, B.; Johnson, L.; Burbano, J.; Danilkowicz, R. M.; Adams, S. B. 3D-Bioprinted GelMA-Gelatin-Hydroxyapatite Osteoblast-Laden Composite Hydrogels for Bone Tissue Engineering. *Bioprinting* **2022**. https://doi.org/10.1016/j.bprint.2022.e00196.

(129) Erzengin, S.; Guler, E.; Eser, E.; Polat, E. B.; Gunduz, O.; Cam, M. E. In Vitro and in Vivo Evaluation of 3D Printed Sodium Alginate/Polyethylene Glycol Scaffolds for Sublingual Delivery of Insulin: Preparation, Characterization, and Pharmacokinetics. *Int. J. Biol. Macromol.* **2022**. https://doi.org/10.1016/j.ijbiomac.2022.02.030.

(130) Sharifi, S.; Islam, M. M.; Sharifi, H.; Islam, R.; Koza, D.; Reyes-Ortega, F.; Alba-Molina, D.; Nilsson, P. H.; Dohlman, C. H.; Mollnes, T. E.; Chodosh, J.; Gonzalez-Andrades, M. Tuning Gelatin-Based Hydrogel towards Bioadhesive Ocular Tissue Engineering Applications. *Bioact. Mater.* **2021**, *6* (11), 3947–3961. https://doi.org/10.1016/j.bioactmat.2021.03.042.

(131) Santoro, M.; Tatara, A. M.; Mikos, A. G. Gelatin Carriers for Drug and Cell Delivery in Tissue Engineering. *Journal of Controlled Release*. 2014. https://doi.org/10.1016/j.jconrel.2014.04.014.

(132) Yin, J.; Yan, M.; Wang, Y.; Fu, J.; Suo, H. 3D Bioprinting of Low-Concentration Cell-Laden Gelatin Methacrylate (GelMA) Bioinks with a Two-Step Cross-Linking Strategy. *ACS Appl. Mater. Interfaces* **2018**. https://doi.org/10.1021/acsami.7b16059.

(133) Negrini, N. C.; Celikkin, N.; Tarsini, P.; Farè, S.; Święszkowski, W. Three-Dimensional Printing of Chemically Crosslinked Gelatin Hydrogels for Adipose Tissue Engineering. *Biofabrication* **2020**. https://doi.org/10.1088/1758-5090/ab56f9.

(134) Ito, R.; Morimoto, N.; Liem, P. H.; Nakamura, Y.; Kawai, K.; Taira, T.; Tsuji, W.; Toi, M.; Suzuki, S. Adipogenesis Using Human Adipose Tissue-Derived Stromal Cells Combined with a Collagen/Gelatin Sponge Sustaining Release of Basic Fibroblast Growth Factor. *J. Tissue Eng. Regen. Med.* **2014**. https://doi.org/10.1002/term.1611.

(135) Nadeem, D.; Kiamehr, M.; Yang, X.; Su, B. Fabrication and in Vitro Evaluation of a Sponge-like Bioactive-Glass/ Gelatin Composite Scaffold for Bone Tissue Engineering. *Mater. Sci. Eng. C* **2013**. https://doi.org/10.1016/j.msec.2013.02.021.

(136) Poursamar, S. A.; Lehner, A. N.; Azami, M.; Ebrahimi-Barough, S.; Samadikuchaksaraei, A.; Antunes, A. P. M. The Effects of Crosslinkers on Physical, Mechanical, and Cytotoxic Properties of Gelatin Sponge Prepared via in-Situ Gas Foaming Method as a Tissue Engineering Scaffold. *Mater. Sci. Eng. C* **2016**. https://doi.org/10.1016/j.msec.2016.02.034.

(137) Chimenti, I.; Rizzitelli, G.; Gaetani, R.; Angelini, F.; Ionta, V.; Forte, E.; Frati, G.; Schussler, O.; Barbetta, A.; Messina, E.; Dentini, M.; Giacomello, A. Human Cardiosphere-Seeded Gelatin and Collagen Scaffolds as Cardiogenic Engineered Bioconstructs. *Biomaterials* **2011**. https://doi.org/10.1016/j.biomaterials.2011.08.049.

(138) Kuwahara, K.; Yang, Z.; Slack, G. C.; Nimni, M. E.; Han, B. Cell Delivery Using an Injectable and Adhesive Transglutaminase-Gelatin Gel. *Tissue Eng. - Part C Methods* **2010**. https://doi.org/10.1089/ten.tec.2009.0406.

(139) Chuang, C. H.; Lin, R. Z.; Tien, H. W.; Chu, Y. C.; Li, Y. C.; Melero-Martin, J. M.; Chen, Y. C. Enzymatic Regulation of Functional Vascular Networks Using Gelatin Hydrogels. *Acta Biomater.* **2015**. https://doi.org/10.1016/j.actbio.2015.02.024.

(140) Yang, G.; Xiao, Z.; Long, H.; Ma, K.; Zhang, J.; Ren, X.; Zhang, J. Assessment of the Characteristics and Biocompatibility of Gelatin Sponge Scaffolds Prepared by Various Crosslinking Methods. *Sci. Rep.* **2018**. https://doi.org/10.1038/s41598-018-20006-y.

(141) Huynh, C. T.; Nguyen, M. K.; Lee, D. S. Injectable Block Copolymer Hydrogels: Achievements and Future Challenges for Biomedical Applications. *Macromolecules*. 2011. https://doi.org/10.1021/ma201261m.

(142) Matricardi, P.; Di Meo, C.; Coviello, T.; Hennink, W. E.; Alhaique, F. Interpenetrating Polymer Networks Polysaccharide Hydrogels for Drug Delivery and Tissue Engineering. *Advanced Drug Delivery Reviews*. 2013. https://doi.org/10.1016/j.addr.2013.04.002.

(143) Goenka, S.; Sant, V.; Sant, S. Graphene-Based Nanomaterials for Drug Delivery and Tissue Engineering. *Journal of Controlled Release*. 2014. https://doi.org/10.1016/j.jconrel.2013.10.017.

(144) Advincula, R. C.; Dizon, J. R. C.; Caldona, E. B.; Viers, R. A.; Siacor, F. D. C.; Maalihan, R. D.; Espera, A. H. On the Progress of 3D-Printed Hydrogels for Tissue Engineering. *MRS Commun.* **2021**. https://doi.org/10.1557/s43579-021-00069-1.

(145) Dutta, S. D.; Hexiu, J.; Patel, D. K.; Ganguly, K.; Lim, K. T. 3D-Printed Bioactive and Biodegradable Hydrogel Scaffolds of Alginate/Gelatin/Cellulose Nanocrystals for Tissue Engineering. *Int. J. Biol. Macromol.* **2021**, *167*, 644–658. https://doi.org/10.1016/j.ijbiomac.2020.12.011.

(146) Eivazzadeh-Keihan, R.; Chenab, K. K.; Taheri-Ledari, R.; Mosafer, J.; Hashemi, S. M.; Mokhtarzadeh, A.; Maleki, A.; Hamblin, M. R. Recent Advances in the Application of Mesoporous Silica-Based Nanomaterials for Bone Tissue Engineering. *Materials Science and Engineering C*. 2020. https://doi.org/10.1016/j.msec.2019.110267.

(147) E, N.; A, R.; A, D.; WL, G. Comparison of 3D-Printed Poly-ε-Caprolactone Scaffolds Functionalized with Tricalcium Phosphate, Hydroxyapatite, Bio-Oss, or Decellularized Bone Matrix. *Tissue Eng. Part A* **2017**. https://doi.org/10.1089/ten.TEA.2016.0418

(148) Markstedt, K.; Mantas, A.; Tournier, I.; Martínez Ávila, H.; Hägg, D.; Gatenholm, P. 3D Bioprinting Human Chondrocytes with Nanocellulose–Alginate Bioink for Cartilage Tissue Engineering Applications. *Biomacromolecules* **2015**, *16* (5), 1489–1496. https://doi.org/10.1021/acs.biomac.5b00188.

(149) Gao, T.; Gillispie, G. J.; Copus, J. S.; PR, A. K.; Seol, Y.-J.; Atala, A.; Yoo, J. J.; Lee, S. J. Optimization of Gelatin–Alginate Composite Bioink Printability Using Rheological Parameters: A Systematic Approach. *Biofabrication* **2018**, *10* (3), 34106. https://doi.org/10.1088/1758-5090/aacdc7.

(150) Kara, A.; Distler, T.; Polley, C.; Schneidereit, D.; Seitz, H.; Friedrich, O.; Tihminlioglu, F.; Boccaccini, A. R. 3D Printed Gelatin/Decellularized Bone Composite Scaffolds for Bone Tissue Engineering: Fabrication, Characterization and Cytocompatibility Study. *Mater. Today Bio* **2022**, *15*, 100309. https://doi.org/https://doi.org/10.1016/j.mtbio.2022.100309.

(151) Kreller, T.; Distler, T.; Heid, S.; Gerth, S.; Detsch, R.; Boccaccini, A. R. Physico-Chemical Modification of Gelatine for the Improvement of 3D Printability of Oxidized Alginate-Gelatine Hydrogels towards Cartilage Tissue Engineering. *Mater. Des.* **2021**, *208*, 109877. https://doi.org/10.1016/j.matdes.2021.109877.

(152) Kolesky, D. B.; Homan, K. A.; Skylar-Scott, M. A.; Lewis, J. A. Three-Dimensional Bioprinting of Thick Vascularized Tissues. *Proc. Natl. Acad. Sci. U. S. A.* **2016**. https://doi.org/10.1073/pnas.1521342113.

(153) Murphy, C. M.; Haugh, M. G.; O'Brien, F. J. The Effect of Mean Pore Size on Cell Attachment, Proliferation and Migration in Collagen-Glycosaminoglycan Scaffolds for Bone Tissue Engineering. *Biomaterials* **2010**. https://doi.org/10.1016/j.biomaterials.2009.09.063.

(154) Woodard, J. R.; Hilldore, A. J.; Lan, S. K.; Park, C. J.; Morgan, A. W.; Eurell, J. A. C.; Clark, S. G.; Wheeler, M. B.; Jamison, R. D.; Wagoner Johnson, A. J. The Mechanical Properties and Osteoconductivity of Hydroxyapatite Bone Scaffolds with Multi-Scale Porosity. *Biomaterials* **2007**. https://doi.org/10.1016/j.biomaterials.2006.08.021.

(155) Rustom, L. E.; Boudou, T.; Lou, S.; Pignot-Paintrand, I.; Nemke, B. W.; Lu, Y.; Markel, M. D.; Picart, C.; Wagoner Johnson, A. J. Micropore-Induced Capillarity Enhances Bone Distribution in Vivo in Biphasic Calcium Phosphate Scaffolds. *Acta Biomater.* **2016**. https://doi.org/10.1016/j.actbio.2016.08.025.

(156) Kim, T. R.; Kim, M. S.; Goh, T. S.; Lee, J. S.; Kim, Y. H.; Yoon, S. Y.; Lee, C. S. Evaluation of Structural and Mechanical Properties of Porous Artificial Bone Scaffolds Fabricated via Advanced TBA-Based Freeze-Gel Casting Technique. *Appl. Sci.* **2019**. https://doi.org/10.3390/app9091965.

(157) Gu, L.; Zhang, Y.; Zhang, L.; Huang, Y.; Zuo, D.; Cai, Q.; Yang, X. Comparative Study of Gelatin Cryogels Reinforced with Hydroxyapatites with Different Morphologies and Interfacial Bonding. *Biomed. Mater.* **2020**. https://doi.org/10.1088/1748-605X/ab7388.

(158) Sartuqui, J.; D'Elía, N. L.; Ercoli, D.; de Alcazar, D. S.; Cortajarena, A. L.; Messina, P. V. Mechanical Performance of Gelatin Fiber Mesh Scaffolds Reinforced with Nano-Hydroxyapatite under Bone Damage Mechanisms. *Mater. Today Commun.* **2019**. https://doi.org/10.1016/j.mtcomm.2019.01.004.

(159) Matthews, F. L.; Rawlings, R. D. Reinforcements and the Reinforcement–Matrix Interface. In *Composite Materials*; 1999. https://doi.org/10.1016/b978-1-85573-473-9.50005-9.

(160) Gerhardt, L. C.; Boccaccini, A. R. Bioactive Glass and Glass-Ceramic Scaffolds for Bone Tissue Engineering. *Materials (Basel).* **2010**. https://doi.org/10.3390/ma3073867.

(161) Mu, C.; Liu, F.; Cheng, Q.; Li, H.; Wu, B.; Zhang, G.; Lin, W. Collagen Cryogel Cross-Linked by Dialdehyde Starch. *Macromol. Mater. Eng.* **2010**. https://doi.org/10.1002/mame.200900292

(162) Savina, I. N.; Gun'Ko, V. M.; Turov, V. V.; Dainiak, M.; Phillips, G. J.; Galaev, I. Y.; Mikhalovsky, S. V. Porous Structure and Water State in Cross-Linked Polymer and Protein Cryo-Hydrogels. *Soft Matter* **2011**. https://doi.org/10.1039/c0sm01304h.

(163) Ghodbane, S. A.; Dunn, M. G. Physical and Mechanical Properties of Cross-Linked Type I Collagen Scaffolds Derived from Bovine, Porcine, and Ovine Tendons. *J. Biomed. Mater. Res. - Part A* **2016**. https://doi.org/10.1002/jbm.a.35813.

(164) Takallu, S.; Mirzaei, E.; Azadi, A.; Karimizade, A.; Tavakol, S. Plate-Shape Carbonated Hydroxyapatite/Collagen Nanocomposite Hydrogel via in Situ Mineralization of Hydroxyapatite Concurrent with Gelation of Collagen at PH = 7.4 and 37°C. *J. Biomed. Mater. Res. - Part B Appl. Biomater.* **2019**. https://doi.org/10.1002/jbm.b.34284.

(165) Distler, T.; McDonald, K.; Heid, S.; Karakaya, E.; Detsch, R.; Boccaccini, A. R. Ionically and Enzymatically Dual Cross-Linked Oxidized Alginate Gelatin Hydrogels with Tunable Stiffness and Degradation Behavior for Tissue Engineering. *ACS Biomater. Sci. Eng.* **2020**, *6* (7), 3899–3914. https://doi.org/10.1021/acsbiomaterials.0c00677.

(166) Martínez Cortizas, A.; López-Costas, O. Linking Structural and Compositional Changes in Archaeological Human Bone Collagen: An FTIR-ATR Approach. *Sci. Rep.* **2020**, *10* (1), 17888. https://doi.org/10.1038/s41598-020-74993-y.

(167) Lewis, P. L.; Green, R. M.; Shah, R. N. 3D-Printed Gelatin Scaffolds of Differing Pore Geometry Modulate Hepatocyte Function and Gene Expression. *Acta Biomater.* **2018**. https://doi.org/10.1016/j.actbio.2017.12.042.

(168) Sattary, M.; Rafienia, M.; Kazemi, M.; Salehi, H.; Mahmoudzadeh, M. Promoting Effect of Nano Hydroxyapatite and Vitamin D3 on the Osteogenic Differentiation of Human Adipose-Derived Stem Cells in Polycaprolactone/Gelatin Scaffold for Bone Tissue Engineering. *Mater. Sci. Eng. C* **2019**. https://doi.org/10.1016/j.msec.2018.12.030.

(169) Popescu-Pelin, G.; Ristoscu, C.; Duta, L.; Stan, G. E.; Pasuk, I.; Tite, T.; Stan, M. S.; Bleotu, C.; Popa, M.; Chifiriuc, M. C.; Oktar, F. N.; Nicarel, A.; Mihailescu, I. N. Antimicrobial and Cytocompatible Bovine Hydroxyapatite-Alumina-Zeolite Composite Coatings Synthesized by Pulsed Laser Deposition from Low-Cost Sustainable Natural Resources. *ACS Sustain. Chem. Eng.* **2020**. https://doi.org/10.1021/acssuschemeng.9b05031.

(170) Yung, C. W.; Wu, L. Q.; Tullman, J. A.; Payne, G. F.; Bentley, W. E.; Barbari, T. A. Transglutaminase Crosslinked Gelatin as a Tissue Engineering Scaffold. *J. Biomed. Mater. Res. - Part A* **2007**. https://doi.org/10.1002/jbm.a.31431.

(171) Kim, H. W.; Kim, H. E.; Salih, V. Stimulation of Osteoblast Responses to Biomimetic Nanocomposites of Gelatin-Hydroxyapatite for Tissue Engineering Scaffolds. *Biomaterials* **2005**. https://doi.org/10.1016/j.biomaterials.2005.01.047.

(172) Landi, E.; Valentini, F.; Tampieri, A. Porous Hydroxyapatite/Gelatine Scaffolds with Ice-Designed Channel-like Porosity for Biomedical Applications. *Acta Biomater.* **2008**. https://doi.org/10.1016/j.actbio.2008.05.023.

(173) Zhu, Y.; Chen, S.; Zhang, C.; Ikoma, T.; Guo, H.; Zhang, X.; Li, X.; Chen, W. Novel Microsphere-Packing Synthesis, Microstructure, Formation Mechanism and in Vitro Biocompatibility of Porous Gelatin/Hydroxyapatite Microsphere Scaffolds. *Ceram. Int.* **2021**. https://doi.org/10.1016/j.ceramint.2021.08.111.

(174) Han, R.; Buchanan, F.; Ford, L.; Julius, M.; Walsh, P. J. A Comparison of the Degradation Behaviour of 3D Printed PDLGA Scaffolds Incorporating Bioglass or Biosilica. *Mater. Sci. Eng. C* **2021**. https://doi.org/10.1016/j.msec.2020.111755.

(175) M'Barki, A.; Bocquet, L.; Stevenson, A. Linking Rheology and Printability for Dense and Strong Ceramics by Direct Ink Writing. *Sci. Rep.* **2017**, *7* (1), 6017. https://doi.org/10.1038/s41598-017-06115-0.

(176) Biscaia, S.; Branquinho, M. V; Alvites, R. D.; Fonseca, R.; Sousa, A. C.; Pedrosa, S. S.; Caseiro, A. R.; Guedes, F.; Patrício, T.; Viana, T.; Mateus, A.; Maurício, A. C.; Alves, N. 3D Printed Poly(ε-Caprolactone)/Hydroxyapatite Scaffolds for Bone Tissue Engineering: A Comparative Study on a Composite Preparation by Melt Blending or Solvent Casting Techniques and the Influence of Bioceramic Content on Scaffold Properties. *Int. J. Mol. Sci.* **2022**, *23* (4). https://doi.org/10.3390/ijms23042318.

(177) Dong, X.; Wu, Z.; Li, X.; Xiao, L.; Yang, M.; Li, Y.; Duan, J.; Sun, Z. The Size-Dependent Cytotoxicity of Amorphous Silica Nanoparticles: A Systematic Review of in Vitro Studies. *Int. J. Nanomedicine* **2020**, *15*, 9089–9113. https://doi.org/10.2147/IJN.S276105.

(178) Wang, X.-F.; Lu, P.-J.; Song, Y.; Sun, Y.-C.; Wang, Y.-G.; Wang, Y. Nano Hydroxyapatite Particles Promote Osteogenesis in a Three-Dimensional Bio-Printing Construct Consisting of Alginate/Gelatin/HASCs. *RSC Adv.* **2016**, *6* (8), 6832–6842. https://doi.org/10.1039/C5RA21527G.

(179) Wenz, A.; Borchers, K.; Tovar, G. E. M.; Kluger, P. J. Bone Matrix Production in Hydroxyapatite-Modified Hydrogels Suitable for Bone Bioprinting. *Biofabrication* **2017**, *9* (4), 44103. https://doi.org/10.1088/1758-5090/aa91ec.

(180) Meesuk, L.; Suwanprateeb, J.; Thammarakcharoen, F.; Tantrawatpan, C.; Kheolamai, P.; Palang, I.; Tantikanlayaporn, D.; Manochantr, S. Osteogenic Differentiation and Proliferation Potentials of Human Bone Marrow and Umbilical Cord-Derived Mesenchymal Stem Cells on the 3D-Printed Hydroxyapatite Scaffolds. *Sci. Rep.* **2022**, *12* (1), 19509. https://doi.org/10.1038/s41598-022-24160-2.

(181) Guillemot, F.; Mironov, V.; Nakamura, M. Bioprinting Is Coming of Age: Report from the International Conference on Bioprinting and Biofabrication in Bordeaux (3B'09). *Biofabrication*. England March 2010, p 10201. https://doi.org/10.1088/1758-5082/2/1/010201.

(182) Kirchmajer, D. M.; Gorkin III, R.; in het Panhuis, M. An Overview of the Suitability of Hydrogel-Forming Polymers for Extrusion-Based 3D-Printing. *J. Mater. Chem. B* **2015**, *3* (20), 4105–4117. https://doi.org/10.1039/C5TB00393H.

(183) Tan, Y. J.; Tan, X.; Yeong, W. Y.; Tor, S. B. Hybrid Microscaffold-Based 3D Bioprinting of Multi-Cellular Constructs with High Compressive Strength: A New Biofabrication Strategy. *Sci. Rep.* **2016**, *6* (1), 39140. https://doi.org/10.1038/srep39140.

(184) Hong, S. H.; Shin, M.; Lee, J.; Ryu, J. H.: Stable Alginate Gel Prepared by Linkage Exchange from Ionic to Covalent Bonds. *Adv. Healthc. Mater.* **2016**, *5* (1), 75–79. https://doi.org/https://doi.org/10.1002/adhm.201400833.

(185) Ahlfeld, T.; Gelinsky, M. Methylcellulose – a Versatile Printing Material That Enables Biofabrication of Tissue Equivalents with High Shape Fidelity. *Biomater. Sci.* **2020**, *8* (8), 2102–2110. https://doi.org/10.1039/D0BM00027B.

(186) Dani, S.; Ahlfeld, T.; Albrecht, F.; Duin, S.; Kluger, P.; Lode, A.; Gelinsky, M. Homogeneous and Reproducible Mixing of Highly Viscous Biomaterial Inks and Cell Suspensions to Create Bioinks. *Gels (Basel, Switzerland)* **2021**, *7* (4). https://doi.org/10.3390/gels7040227.

(187) Schütz, K.; Placht, A.-M.; Paul, B.; Brüggemeier, S.; Gelinsky, M.; Lode, A. Three-Dimensional Plotting of a Cell-Laden Alginate/Methylcellulose Blend: Towards Biofabrication of Tissue Engineering Constructs with Clinically Relevant Dimensions. *J. Tissue Eng. Regen. Med.* **2017**, *11* (5), 1574–1587. https://doi.org/10.1002/term.2058.

(188) Li, H.; Tan, Y. J.; Leong, K. F.; Li, L. 3D Bioprinting of Highly Thixotropic Alginate/Methylcellulose Hydrogel with Strong Interface Bonding. *ACS Appl. Mater. Interfaces* **2017**, *9*. https://doi.org/10.1021/acsami.7b04216.

(189) Karavasili, C.; Tsongas, K.; Andreadis, I. I.; Andriotis, E. G.; Papachristou, E. T.; Papi, R. M.; Tzetzis, D.; Fatouros, D. G. Physico-Mechanical and Finite Element Analysis Evaluation of 3D Printable Alginate-Methylcellulose Inks for Wound Healing Applications. *Carbohydr. Polym.* **2020**, *247*, 116666. https://doi.org/https://doi.org/10.1016/j.carbpol.2020.116666.

(190) Barceló, X.; Eichholz, K. F.; Garcia, O.; Kelly, D. J. Tuning the Degradation Rate of Alginate-Based Bioinks for Bioprinting Functional Cartilage Tissue. *Biomedicines* **2022**, *10* (7). https://doi.org/10.3390/biomedicines10071621.

(191) Rastogi, P.; Kandasubramanian, B. Review of Alginate-Based Hydrogel Bioprinting for Application in Tissue Engineering. *Biofabrication* **2019**, *11* (4), 42001. https://doi.org/10.1088/1758-5090/ab331e.

(192) Ahlfeld, T.; Cubo-Mateo, N.; Cometta, S.; Guduric, V.; Vater, C.; Bernhardt, A.; Akkineni, A. R.; Lode, A.; Gelinsky, M. A Novel Plasma-Based Bioink Stimulates Cell Proliferation and Differentiation in Bioprinted, Mineralized Constructs. *ACS Appl. Mater. Interfaces* **2020**, *12* (11), 12557–12572. https://doi.org/10.1021/acsami.0c00710.

(193) Liu, S.; Kilian, D.; Ahlfeld, T.; Hu, Q.; Gelinsky, M. Egg White Improves the Biological Properties of an Alginate-Methylcellulose Bioink for 3D Bioprinting of Volumetric Bone Constructs. *Biofabrication* **2023**, *15* (2). https://doi.org/10.1088/1758-5090/acb8dc.

(194) Saravanou, S. F.; Ioannidis, K.; Dimopoulos, A.; Kounelaki, F.; Varsami, S. M.; Tsitsilianis, C.; Papantoniou, I.; Pasparakis, G. Dually Crosslinked Injectable Alginate-Based Graft Copolymer Thermoresponsive Hydrogels as 3D Printing Bioinks for Cell Spheroid Growth and Release. *Carbohydr. Polym.* **2023**, *312*, 120790. https://doi.org/https://doi.org/10.1016/j.carbpol.2023.120790.

(195) Ahlfeld, T.; Cidonio, G.; Kilian, D.; Duin, S.; Akkineni, A. R.; Dawson, J. I.; Yang, S.; Lode, A.; Oreffo, R. O. C.; Gelinsky, M. Development of a Clay Based Bioink for 3D Cell Printing for Skeletal Application. *Biofabrication* **2017**, *9* (3), 034103. https://doi.org/10.1088/1758-5090/aa7e96.

(196) Ruther, F.; Distler, T.; Boccaccini, A. R.; Biofabrication of Vessel-like Structures with Alginate Di-Aldehyde—Gelatin (ADA-GEL) Bioink. *J. Mater. Sci. Mater. Med.* **2019**, *30* (1), 8. https://doi.org/10.1007/s10856-018-6205-7.

(197) Gasperini, L.; Mano, J. F.; Reis, R. L. Natural Polymers for the Microencapsulation of Cells. *Journal of the Royal Society Interface*. 2014. https://doi.org/10.1098/rsif.2014.0817.

(198) Jia, J.; Richards, D. J.; Pollard, S.; Tan, Y.; Rodriguez, J.; Visconti, R. P.; Trusk, T. C.; Yost, M. J.; Yao, H.; Markwald, R. R.; Mei, Y. Engineering Alginate as Bioink for Bioprinting. *Acta Biomater.* **2014**, *10* (10), 4323–4331. https://doi.org/https://doi.org/10.1016/j.actbio.2014.06.034.

(199) Lee, K. Y.; Mooney, D. J. Alginate: Properties and Biomedical Applications. *Prog. Polym. Sci.* **2012**, *37* (1), 106–126. https://doi.org/10.1016/j.progpolymsci.2011.06.003.

(200) Heid, S.; Becker, K.; Byun, J.; Biermann, I.; Neščáková, Z.; Zhu, H.; Groll, J.; Boccaccini, A. R. Bioprinting with Bioactive Alginate Dialdehyde-Gelatin (ADA-GEL) Composite Bioinks: Time-Dependent in-Situ Crosslinking via Addition of Calcium-Silicate Particles Tunes in Vitro Stability of 3D Bioprinted Constructs. *Bioprinting* **2022**, *26*, e00200. https://doi.org/10.1016/j.bprint.2022.e00200.

(201) Zhu, H.; Monavari, M.; Zheng, K.; Distler, T.; Ouyang, L.; Heid, S.; Jin, Z.; He, J.; Li, D.; Boccaccini, A. R. 3D Bioprinting of Multifunctional Dynamic Nanocomposite Bioinks Incorporating Cu-Doped Mesoporous Bioactive Glass Nanoparticles for Bone Tissue Engineering. *Small* **2022**, *18*, 2194996. https://doi.org/10.1002/smll.202104996.

(202) Guduric, V.; Belton, N.; Richter, R. F.; Bernhardt, A.; Spangenberg, J.; Wu, C.; Lode, A.; Gelinsky, M. Tailorable Zinc-Substituted Mesoporous Bioactive Glass/Alginate-Methylcellulose Composite Bioinks. *Materials (Basel).* **2021**, *14* (5). https://doi.org/10.3390/ma14051225.

(203) Cheng, L.; Yao, B.; Hu, T.; Cui, X.; Shu, X.; Tang, S.; Wang, R.; Wang, Y.; Liu, Y.; Song, W.; Fu, X.; Li, H.; Huang, S. Properties of an Alginate-Gelatin-Based Bioink and Its Potential Impact on Cell Migration, Proliferation, and Differentiation. *Int. J. Biol. Macromol.* **2019**, *135*, 1107–1113. https://doi.org/10.1016/j.ijbiomac.2019.06.017.

(204) Neufurth, M.; Wang, X.; Müller, W. E. G. Engineering a Morphogenetically Active Hydrogel for Bioprinting of Bioartificial Tissue Derived from Human Osteoblast-like SaOS-2 Cells. *Biomaterials* **2014**, *35* (31), 8810–8819. https://doi.org/https://doi.org/10.1016/j.biomaterials.2014.07.002.

(205) Ashammakhi, N.; Khademhosseini, A. Bioinks and Bioprinting Technologies to Make Heterogeneous and Biomimetic Tissue Constructs. *Mater. Today Bio* **2019**, *1*, 100008. https://doi.org/https://doi.org/10.1016/j.mtbio.2019.100008.

CURRICULUM VITAE

Aylin KARA ÖZENLER

EDUCATION

MSc, Dokuz Eylul University – Biomechanics, 2017

BSc, Ege University - Biology, 2012

FELLOWSHIPS

- The Scientific and Technological Research Council of Turkey – International Research Fellowship Program (TUBITAK-2214A) (2021- 2022)

- The Scientific and Technological Research Council of Turkey – The Scientific and Technological Research Projects Funding Program, TUBITAK-1001 (2017-2020)

- Council of Higher Education 100/2000 PhD Scholarship in Biomaterials and Tissue Engineering (CoHE 100/2000) (2017- 2022)

- IZTECH-Scientific Research Project (2020-İYTE-180) (2020-2021)

PUBLICATIONS

1. Kara, A., Distler, T., Tihminlioglu, F., Boccaccini, A.R. "Fish scale containing alginate dialdehyde-gelatin bioink for bone tissue engineering" Biofabrication (2023).

2. Kara, A., Distler, T., Polley, C., Schneidereit, D., Seitz, H., Friedrich, O., Tihminlioglu, F., Boccaccini, A.R. "3D printed gelatin/decellularized bone composite scaffolds for bone tissue engineering: Fabrication, characterization and cytocompatibility study" Materials Today Bio 15, 100309 (2022).

3. Gunes O.C., Kara A, Baysan G., Husemoglu R.B., Akokay P., Ziylan Albayrak A., Ergur B.U., Havitcioglu H. "Fabrication of 3D Printed poly(lactic acid) strut and wet electrospun cellulose nanofiber reinforced chitosan-collagen hydrogel composite scaffolds for meniscus tissue engineering". J Biomater Appl. Jun 18, (2022).

4. Kara A., Koçtürk S., Bilici G., Havıtçıoğlu H. "Development of biological meniscus scaffold: Decellularization method and recellularization with meniscal cell population derived from mesenchymal stem cells." Journal of Biomaterials Applications 35; 192-1207 (2021).

5. Cecen B., Topates G., Kara A., Onat S., Havıtçıoğlu H., Kozaci D. "Biocompatibility of Silicon Nitride Produced Via Partial Sintering & Tape Casting." Ceramics International 47;3938-3945, (2021).

6. Kara A., Gunes O.C., Albayrak A., Bilici G., Erbil G., Havitcioglu H. "Fish scale/poly(3-hydroxybutyrate-co-3-hydroxyvalerate) nanofibrous composite scaffolds for bone regeneration." Journal of Biomaterials Applications 34; 1201-1215, (2020).

7. Kara A., Tamburacı S, Tıhmınlıoglu F, Havıtçıoğlu H. "Bioactive fish scale incorporated chitosan biocomposite scaffolds for bone tissue engineering" International Journal of Biological Macromolecules, 130;266–279, (2019).

8. Kara, A., Kizmazoglu, C., Husemoglu, B., Bilici, G., Kocturk, S., Havitcioglu, H. "Is It Possible to Develop Allograft Dura Mater Scaffold by Decellularization Method?" The British Editorial Society of Bone & Joint Surgery, Orthopaedic Proceedings, 100 (SUPP_4), 41 41, (2018).

9. Acan E.A., Hapa O., Horoz L., Kara A., Havitcioglu, H. "Effects of a lateral row anchor position on the suture holding strength of a double-row knotless fixation in rotator cuff repair." Joint Diseases and Related Surgery, 29(1):46-51, (2018).

10. Cecen, B., Kozacı, L.D., Yüksel, M., Kara, A., Ersoy, N., Bagrıyanik, A., Havitcioglu, H. "Two Layered Scaffolds (Loofah/PLLA/Cellulose/Chitin) for Repair of Osteochondral Defect." J Tissue Science and Engineering 8: 210, (2017).

11. Kara, A., Kocturk, S., Cecen, B., Erbil, G., Sacık, U., Havıtcıoglu, H. "Meniscus Acellularization Using Allograft Native Scaffold." Biomedical Engineering Meeting (BIYOMUT), 20th National, IEEE Xplore, 1-4, (2016).

PROJECTS

- "Development and in vitro biocompatibility study of novel bioink using decellularized bone extracellular matrix for bone tissue engineering" supported by The Scientific and Technological Research Council of Turkey TUBITAK (2022- 2023), Technical University of Dresden, Centre for Translational Bone, Joint and Soft Tissue Research. Guest PhD Student.
- "Development of novel composite bioinks using natural ECM for bone tissue engineering", Friedrich-Alexander-Universität Erlangen-Nurnberg (2020-2021), Guest PhD Student.
- "Development of Decellularized, Biocompatible Bone Extracellular Matrix for Bone Tissue Regeneration." supported by Izmir Institute of Technology (2020-2021), PhD Student.
- "Comparison of the Healing Rates of Autologous Mesenchymal Stem Cells and Platelet-Rich Plasma in Osteoarthritis Model: In Vitro and In Vivo Study in Wistar Albino Rats.", supported by Dokuz Eylul University (2018- 2020), PhD Student.
- "Development of Cellulose and Hydrogel Based Meniscus Scaffolds Using 3D Printing and Electrospinning Methods.", supported by The Scientific and Technological Research Council of Turkey TUBITAK (2017- 2021), PhD Student.
- "Assessment of the Repair of the Cartilage Tissue Damages as in vitro and in vivo by using Hydrogel-Based Scaffolds.", supported by Dokuz Eylul University (2016-2020), PhD Student.
- "Development of Meniscus Tissue Biocompatibility by Using Allograft Native Scaffold.", supported by Dokuz Eylul University (2015-2017), MSc Student (Thesis Study).
- "Development of Two Layered Scaffolds (Loofah/PLLA/Cellulose/Chitin) for Repair of Osteochondral Defect.", supported by Dokuz Eylul University (2012-2014), MSc Student.